POLITECNICO DI MILANO

School of Industrial and Information Engineering
Master's Degree in Materials Engineering and
Nanotechnology

RELIABILITY OF AN ELECTROMAGNETICALLY ACTUATED MICROMIRROR

Advisor: Prof. Alberto Corigliano
Co-Advisors: Alessandro Balzelli Ludovico,
              Stefano Losa

Thesis by:
Matteo Baiardi, ID 899583

Academic Year 2018-2019

"Imagination is more important than knowledge."

Albert Einstein

Ringraziamenti

Abstract

MEMS are a type of technology based on silicon that is in continuous development. This thesis work was carried out as part of a collaboration between the *Department of Civil and Environmental Engineering* of *Politecnico di Milano* and *STMicroelectronics.* An electromagnetic micro-mirror called "Porcino", belonging to the family of actuators, has been taken into consideration from the reliability point of view. A test matrix (mechanical, powered and unpowered tests) was developed to investigate and study possible failure modes of Porcino. The results confirmed two of them: one linked to the oxidation of a copper coil due to power dissipated generated by the flowing current, and one linked to fatigue life in humid environments. The first one has been solved thanks to the increase in thickness of the coil itself (less dissipated power and therefore also lower oxidation rates), while the second is still a problem. For both failure modes, physical and statistical models have been developed trying to predict the behavior of Porcino in different operating conditions. The models describe well the collected experimental data, but those related to failures in humidity are still to be improved. Regarding the fatigue in humid environment, innovative solutions are being investigated, in particular about the deposition of hydrophobic self-assembled monolayers (SAM) on the surfaces affected by breakage. However, data on results obtained with this treatment are not available yet.

Sommario

I MEMS sono un tipo di tecnologia basata sul silicio in continuo sviluppo. Questo lavoro di tesi è stato svolto nell'ambito di una collaborazione tra il *Dipartimento di Ingegneria Civile ed Ambientale* del *Politecnico di Milano* e *STMicroelectronics*. E' stato preso in considerazione dal punto di vista dell'affidabilità un attuatore, e più in particolare un micro-specchio elettromagnetico chiamato "Porcino". E' stata realizzata una matrice di test (test meccanici, alimentati e non alimentati) per investigare e studiare i possibili meccanismi di rottura del Porcino. I risultati ne hanno confermati due: uno legato all'ossidazione di una bobina di rame a causa della dissipazione generata dalla corrente che scorre al suo interno, ed uno legato alla vita a fatica in ambiente umido. Il primo è stato risolto grazie all'aumento di spessore della bobina stessa (minor potenza dissipata e quindi minor tasso di ossidazione), mentre il secondo risulta tutt'ora un problema. Per entrambi i meccanismi sono stati sviluppati modelli di natura fisica e statistica per cercare di predire il comportamento del Porcino in diverse condizioni operative. I modelli descrivono bene i dati sperimentali raccolti, ma quelli relativi ai fallimenti in umidità sono ancora da migliorare. Per quanto riguarda i fallimenti in umidità si stanno cercando soluzioni innovative, in particolare circa la deposizione di self-assembled monolayer (SAM) idrofobici sulle superfici interessate da rottura. Ad ogni modo non sono ancora disponibili dati relativi ai risultati ottenuti con questo trattamento.

Contents

List of Figures

List of Tables

List of Listings

Introduction

Micro electro mechanical systems, better known as MEMS, are micro devices whose history started with the famous speech *There's Plenty of Room at the Bottom* given by Richard Feynman on December 29th, 1959, about what would later be called nanotechnology. After that lecture, the first MEMS device was invented by Harvey C. Nathanson in 1965, and it was conceived to serve as a tuner for microelectronic radios (a refined version was then patented in 1967 as the Resonant Gate Transistor). In the following years more and more MEMS devices were created and produced, starting from the now very well-established inertial sensors, like accelerometers and gyroscopes, up to the most recent and still partially to be studied devices like actuators (e.g. micro pumps, micro mirrors, etc...). As well described in the book *Mechanics of Microsystems* [1], a good overview of what a MEMS actually is, can be obtained analyzing every part of the acronym:

- *Micro* means that small devices are considered, in which the smallest dimensions can be even at the sub-micrometer scale;

- *Electro* means that inside these small devices there are electric and electronic components, used to transform a physical information in electric signals or, conversely, to activate movements inside the device;

- *Mechanical* means that microsystems have some portion of their architecture that works thanks to mechanical principles, like suspended structures loaded by inertial forces;

- *System* means that these devices are not simple, indeed they must be considered as complex systems combining various components (electronic, mechanical and extra parts, such as optical elements).

This thesis work was carried out as part of a collaboration between the *Department of Civil and Environmental Engineering* of *Politecnico di Milano* and *STMicroelectronics*, which is a leading company in this field of applications. Nowadays it develops and produces many kind of MEMS devices, among which inertial sensors and actuators.

In recent years, an important effort has been made to study and develop innovative devices, in particular to enter the actuator market. Among these are micro-mirrors; they belong to the family of Micro-Opto-Electro-Mechanical-Systems (MOEMS), which in general are MEMS merged with micro-optics, and involve sensing or manipulating optical signals on a very small size scale by using integrated mechanical, optical and electrical systems. Coupling all these technologies is paving the way to several devices such as optical switches, digital micro-mirrors and dynamic displays, bi-stable mirrors, laser micro-scanners, optical shutters, micro-spectrometers, and micro-lenses.

The main character of this thesis is indeed a micro-mirror (called *Porcino* fort its mushroom-like structure), a custom device of which ST deals only with the MEMS, but not with the driving system. Its final application is not yet clear as it is a customer business secret, anyway some hypotheses have been made about it, for example about facial and gesture recognition.

1.1 Thesis Objective

The purpose of this thesis is to show the procedure that has been used to prove the reliability of an electromagnetically actuated micro-mirror (called Porcino), a fundamental step for qualification of the product and its subsequent industrial production. It must be clear that this work started while the qualification was already in progress, and therefore it will cover only the latest versions of the device. Several difficulties have been encountered due to the fact that this type of product is highly innovative, and therefore no standard and automated procedures are available yet for testing the devices. In this regard, a test matrix has been prepared to investigate the possible failure mechanisms of Porcino, in particular to discover and study both those related to the device itself and to its application and those related to the materials which compose its structure.

Porcino has been subjected to different kind of tests: mechanical tests, powered tests, unpowered tests. The activity has been carried out in collaboration, as well as with Reliability team, with Characterization and Design teams, with the support, when necessary, of Failure Analysis and Technology teams.

From the reliability activity, two failure modes have been discovered for Porcino: one related to copper oxidation, and one to fatigue of Si/SiO_2 in humid environment.

Predictive models (both of physical and statistical nature) about these phenomena have been also developed, which are useful to transpose the results obtained during the accelerated tests to other operating conditions (for example different temperature, humidity and stress) and give an idea of how many devices could fail during application in real life.

1.2 Work Organization

Chapter 2 provides an overview of resonant micro-mirrors. In particular in the first part are explained the possible actuation principles and operation modes, with also a digression on micro-mirrors requirements that can help in the general understanding of this devices. A brief report on material selection and possible applications is also present. At the end of the chapter, the state of the art with some examples of already studied micro-mirrors is presented.

Chapter 3 gives an overview of *Porcino* project, with a description of the device, its functioning and its process flow.

Chapter 4 provides an overview on what reliability is and an in-depth description of the test matrix applied to Porcino device.

Chapter 5 includes the description of analytical models, both of physical and statistical nature, regarding the most interesting failure modes found out during reliability test matrix.

Chapter 6 summarize the work done for this thesis project, drawing conclusions on results obtained and providing intentions for future activities.

CHAPTER 2

Micro-mirrors Overview

In the first part of this chapter, some of the main principles that are needed to understand a micro-mirror functioning are explained. These concepts are of general validity, and don't depend on the particular actuation mechanism used for the device.

The second part summarizes the state of the art of micro-mirrors, considering studies found in literature. Particular attention was given to the specific type of actuation mechanism used for each of them.

2.1 Basics of Micro-mirrors

Micro-mirrors are MEMS merged with micro-optics (MOEMS), and among their applications, the principal ones are sensing and manipulation of optical signals at a very small scale, exploiting integrated mechanical, optical and electrical systems.

2.1.1 Actuation Mechanisms for Micro-mirrors

A MEMS micro-mirror (see Fig. 2.1) consist, in general, of a central, reflective surface (the mirror itself) supported by a cantilever beam at one side or by torsional
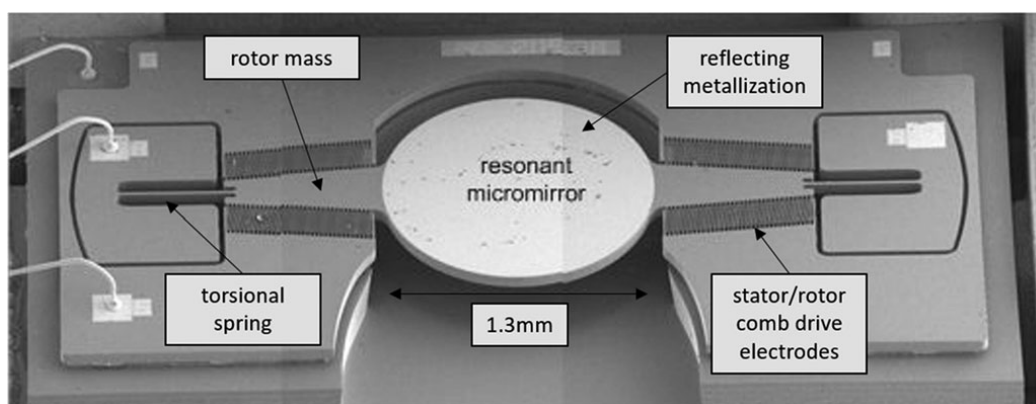
Figure 2.1: SEM image of an electrostatic micro-mirror developed in *ST*. In figure are also indicated some components typical of this kind of device. Adapted from [2]

.
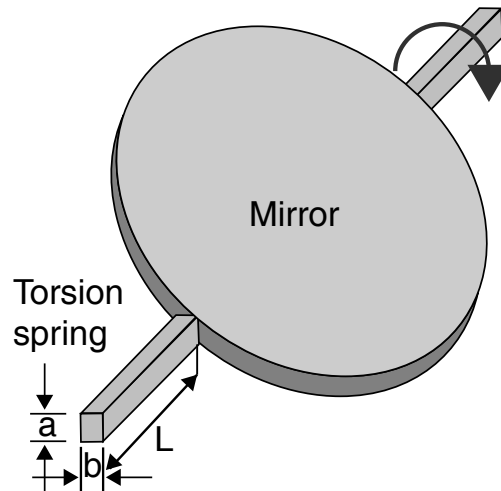
Figure 2.2: Representation of a MEMS scanning mirror during actuation, supported by torsional springs. Adapted from [3]

.

springs at both sides (most common configuration). The first things to know when designing a micro-mirror are the scanning speed and the scanning angle, that unluckily have conflicting influence on design selection. In the following, some important quantities related to torsional springs are analyzed, considering a rectangular cross-section as the most common one. Taking into account the structure represented in Fig. 2.2, for this kind of beam, the torsional constant k_θ of the spring is given by[3]:

$$k_\theta = \frac{T}{\theta} \frac{\beta G a b^3}{L} \tag{2.1}$$

where:
T = Applied torque;
θ = Mechanical rotation angle;
G = Shear modulus of the beam material;
a = Wider dimension of the rectangular cross-section;
b = Narrower dimension of the rectangular cross-section;
β = Tabulated constant depending on b/a;
L = Beam length.

The natural frequency ω_0 of the mirror based on symmetric torsional springs is given by[3]:

$$\omega_0 = \sqrt{\frac{2k_\theta}{J}} \tag{2.2}$$

where J is the mass moment of inertia, and depends mostly on the manufacturing process used to obtain the desired mirror configuration. A low J is preferred in order to keep the scanning speed high, but requirements for mirror surfaces usually brings to relatively high thickness, resulting in higher J.

The maximum displacement achievable by the mirror can be limited by either the applied torque generated to drive the mirror, or by the maximum shear stress

that may arise in the springs τ_{max} [3]:

$$\tau_{max} = \frac{T}{\alpha ab^2} \tag{2.3}$$

where α is another constant depending on a and b.

Many technologies are available to get various kind of micro-mirrors and, in particular, with different type of actuation systems, depending on the application requirements (see Fig. 2.3). The main mechanisms available nowadays are reported in the following:

- **Electrostatic** devices are those that have been studied the most over the years, and therefore they are the most known and understood at present. They allows to reach high speed, but provide limited mechanical scanning ranges at non-resonance (typically 2°) and up to 20° at resonance. Moreover this actuation mode often requires an actuator of big dimensions and relatively high voltages, above 40 V. An advantage of electrostatic actuators is that, to reduce the number of failure modes of the scanners related to this actuation principle, it is possible to apply some robust surface micromachining processes.

- **Electrothermal** micro-mirrors have also been extensively investigated. Both unidirectional and bidirectional scanning at angles up to ±30° with low driving voltages have been achieved. Some disadvantages of this kind of actuation system are the necessity of high driving currents, the requirement for thermal isolation of the actuator and a rather slow dynamic response.

- **Electromagnetic** scanners have been studied more recently. They exploit the Lorentz principle to generate an oscillating force starting from a current presumably flowing in a coil and the presence of a strong magnetic field. Their big advantage is that they use a relatively low voltage to generate quite large forces, allowing the scanning mirror to reach rather large deflection angles. The main drawbacks of this actuation mechanism are its high power consumption and the complex structures to obtain a bi-axial actuation. This is the principle used for the actuation of Porcino, the device that will be analyzed in this work.

- **Piezoelectric** devices represent the new frontier for MEMS and MOEMS, so nowadays this actuation system is among the most investigated. For what concerns micro-mirrors it presents several advantages, first of all large deflection angles by using low voltages and minimum power consumption. A drawback could be that, in case of a device designed with a large mirror surface, also the area covered by the piezoelectric material should be wide to guarantee a proper actuation, and this would bring to rather high occupation volumes.

In this thesis more attention will be given to the electromagnetic actuation principle, as it is the one exploited for the actuation of the studied device, Porcino.
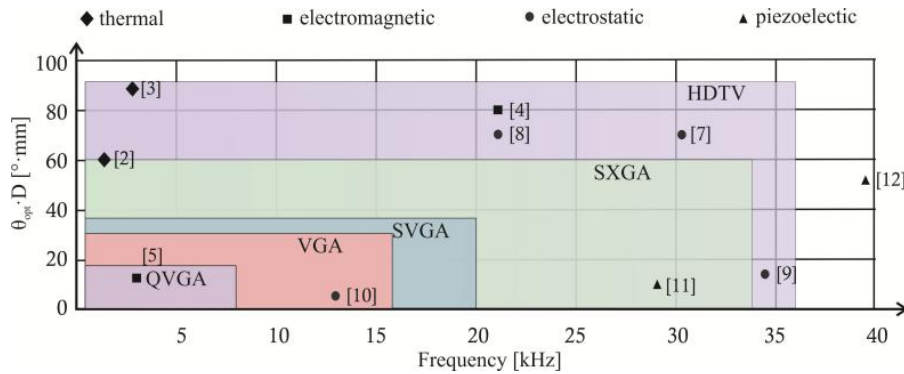
Figure 2.3: In figure is reported a comparison of performances of micro-mirrors actuated by different principles. On the axes are reported the θD-product and the frequency. Adapted from [4]

.

2.1.2 Operating Modes and Parametric Resonance

Micro-mirrors embedded in a MOEMS can oscillate with respect to a single axis or both, depending on the desired application. Obviously a mirror that twists on a single axis is easier to design, fabricate and drive than a bi-axial one, but the main drawback is that, if a full raster pattern is needed, at least a couple of mirror is necessary, as shown in Fig. 2.4. Evidently this brings to a higher volume occupation, that is not always compatible with the final device. On the contrary, a bi-axial micro-mirror can be embedded more easily in the final system, but it's much more difficult to drive, due to the fact that both axes must be opened at proper angles at the same time, using a single driving system, and from this also more difficulties come in designing and fabricating.

A micro-mirror can work in various conditions, and more precisely with different operating modes:

- **Quasi-static mode**, in which both axis are controlled without resonance, and so the mirror can either hold a static position or move at a steady velocity for raster scanning and vector graphics. This mode is good because it is simple to synchronize the laser source to the mirror movement, and to ensure that each point is exposed by an equal amount of light, which makes it simpler to achieve a uniform picture. However, it is very challenging to produce a single mirror with both large deflection and high-frequency scanning in two directions.

- **Resonant mode**, in which both axes exploit the resonance of the mechanical structure to obtain a large optical deflection amplitude. The problem here is that the frequency range for functioning is very narrow and sinusoidal trajectories shouldn't have a delay in phase with respect to the ap-
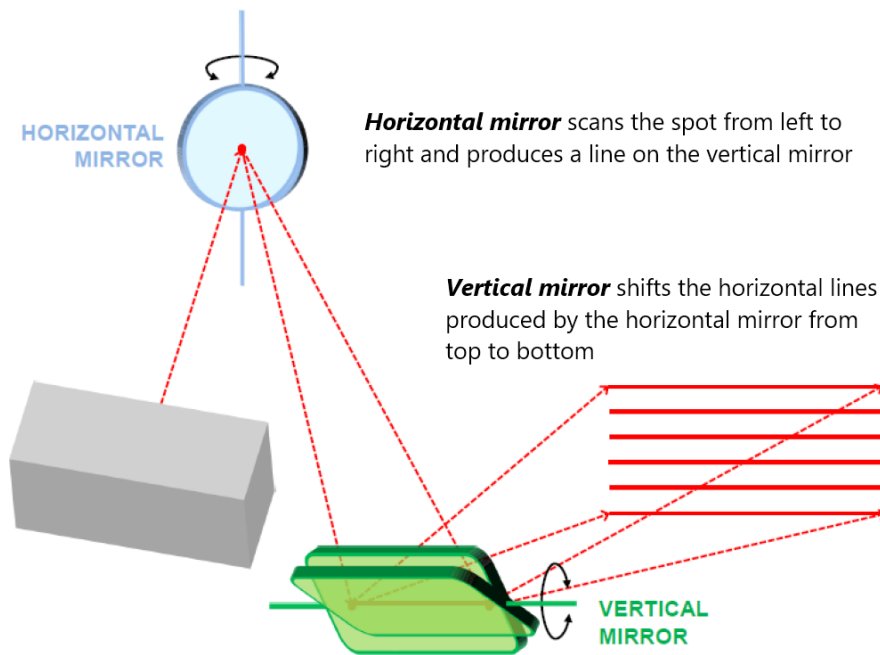
Figure 2.4: Projection principle with single-axis micro-mirrors. On the left a point light source, colored in gray; at the top a horizontal micro-mirror; at the bottom a vertical micro-mirror; on the right the full-raster projection, result of the two different projections.

plied voltage. Resulting 2D motions are therefore often limited to special shapes like circles or ellipses.

- **Combined mode**, which is a combination of the previous two; here one axis is driven in resonance at high frequency (some kHz) to create a line in one direction (for example a vertical line), while the second axis is driven quasi-statically to create a full-raster pattern that covers a rectangular area in a controlled way.

The operating modes described above are valid both for bi-axial micro-mirrors and uni-axial ones, again, with the foresight to remember that the last ones need more than one mirror to operate. So, for example, if two uni-axial mirrors are used, in order to have a device working in combined mode, one of them should work in resonant mode, while the other in quasi-static mode. As generally the combined mode is the preferred mode of operation of a micro-scanner for image projection applications, it will be analyzed more in detail in the following.

The resonant scanner will typically run at frequencies exceeding 10 kHz, and should provide a large scan angle. Being in resonant condition, the fast scanner can meet these rates and resolution requirements with the added advantage of low power consumption. Additionally, the resonant scanner can provide a master pixel clock rate[1] for the system. In general, for good image quality, the fast scan (e.g. horizontal) position and frequency should derive from the slow ones (e.g. vertical), therefore the slow axis is preferably non-resonant and driven with

---

[1]Pixel clock rate is the speed at which pixels are transmitted in order for a full frame of pixels to fit within a single refresh cycle
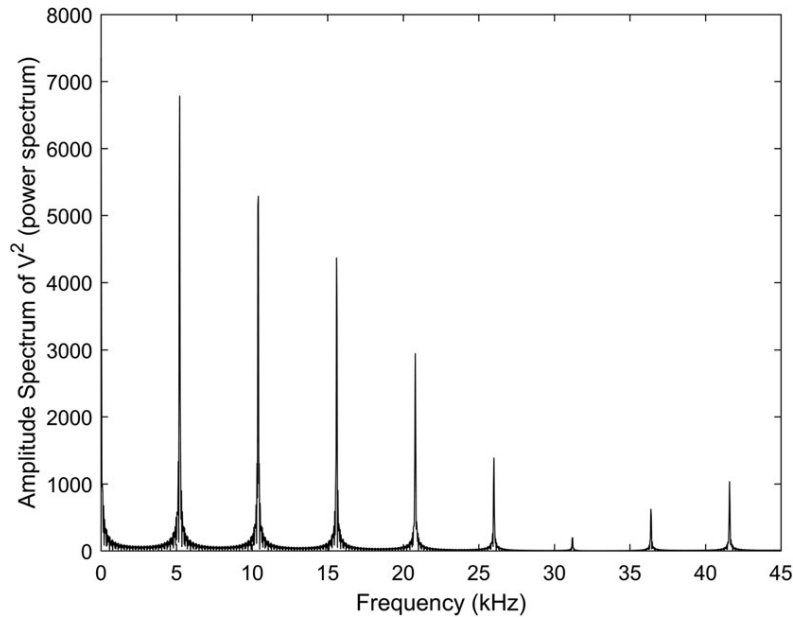
Figure 2.5: Representation of the power spectrum for a 150 V square wave used to drive an electrostatic micro-mirror with $f_0 \sim 5300$ Hz, adapted from [2]. Please note that as n gets higher (from left to right), the amplitude of the forcing parameter (V^2 in this case) becomes smaller; moreover the square wave is a waveform that usually contains all of the multiples $n\omega_{SW}$ of the fundamental frequency, and so it can easily excite undesired mechanical modes

a waveform that provides equal spacing between raster lines (e.g. a sinusoidal one), at a frequency that equals the refresh rate of the display[5].

An important phenomenon regarding resonating MEMS is the so called *parametric resonance*. As reported above, micro-mirrors are driven with waves at frequencies close to their natural frequency, so that high scanning angles and low power consumption are achieved. However it is possible to exploit parametric resonance to excite the desired resonant mode (e.g.torsional mode oscillation of the sprigs supporting the mirror) even at frequencies different from the natural one of the system. As reported in literature[6], various sources can activate parametric excitation in resonant micro-systems, as piezoelectric elements, Lorentz forces and thermal interactions.

Parametric resonance is effective when the cycle of modulation repeats twice during one period of natural oscillations in the system, that is when a parametric modulation's frequency is equal to twice the system's natural frequency. Mathematically it's possible when [7]:

$$n\omega_M = 2\omega_0 \tag{2.4}$$

where n is a positive integer, ω_M is the frequency of the modulation and ω_0 is the natural frequency of the mechanical system. Usually the higher is the order n of parametric resonance, the less is the amount of energy transferred to the oscillating system at each period, as can be seen in the example of Fig. 2.5, where the power spectrum of a square wave is represented. A good way to exploit this phenomenon is to use it when the standard driving condition would excite un-

desired mechanical modes[2] (*spurious modes*), and so there is need to move away from these problematic regions. Nevertheless, this phenomenon can either be a problem when driving wave contains frequencies that can excite the already mentioned spurious modes.

A big difference to keep in mind when comparing forced oscillations and parametric excitation is that for the first, the increment of energy during one period is proportional to the amplitude of oscillations ($\propto \sqrt{E}$), while for the last, energy increment is proportional to the energy stored in the system.

2.1.3 Materials Selection

For what concerns the structural part of the MOEMS devices, silicon (Si), both in its poly-crystalline and mono-crystalline form, remains the best choice. Indeed, Si results good both for its mechanical and electrical properties[8] as widely investigated in [9], and for the knowledge that is now consolidated from the manufacturing point of view with this material, given also the fact that it is the second most abundant element on the Earth (this implies lower production costs). To maintain the flatness of large mirrors, such devices are typically fabricated in single crystal silicon (SCS).

Obviously, to guarantee a high level of reflectance, the materials used to cover the mirror surface must be metals. The metallic coatings are different depending on which range of the electromagnetic spectrum is needed for the application. In general, and also in *ST*, for the visible-UV range aluminum (Al-5N[3]) is used, with a maximum reflectance of 90% in the visible, while for the infrared spectrum gold (Au-4N) is the chosen material, with a reflectance of 97% in the IR range (Fig. 2.6). Finally, depending on the application and, above all, on the actuation mechanism, other materials can also be used in addition. Among these some examples are copper (Cu), used when high conductivity is necessary, and titanium (Ti) and nickel (Ni), useful to protect some materials particularly subject to oxidation.

2.1.4 Main Fields of Application

In the following, taking into account the information given until this point, a brief overview is reported about different solutions studied by *ST* (but of general validity), to cover a wide range of application:

- **Augmented Reality (AR)**: in this kind of application a set of micro-mirrors is embedded in a system able to give the user an interactive experience of a real world environment where the objects that reside in the real world are enhanced by computer-generated perceptual information (not to confuse with *Virtual Reality*). Of course a projection in the visible range of the

---

[2]in particular, for what concerns micro-mirrors, all those modes different from the torsional one

[3]This notation indicates the "number of 9" in the purity level. In a few words, a level of purity 5N means that the material is pure at 99.999% while 4N means at 99.99%, and so on.
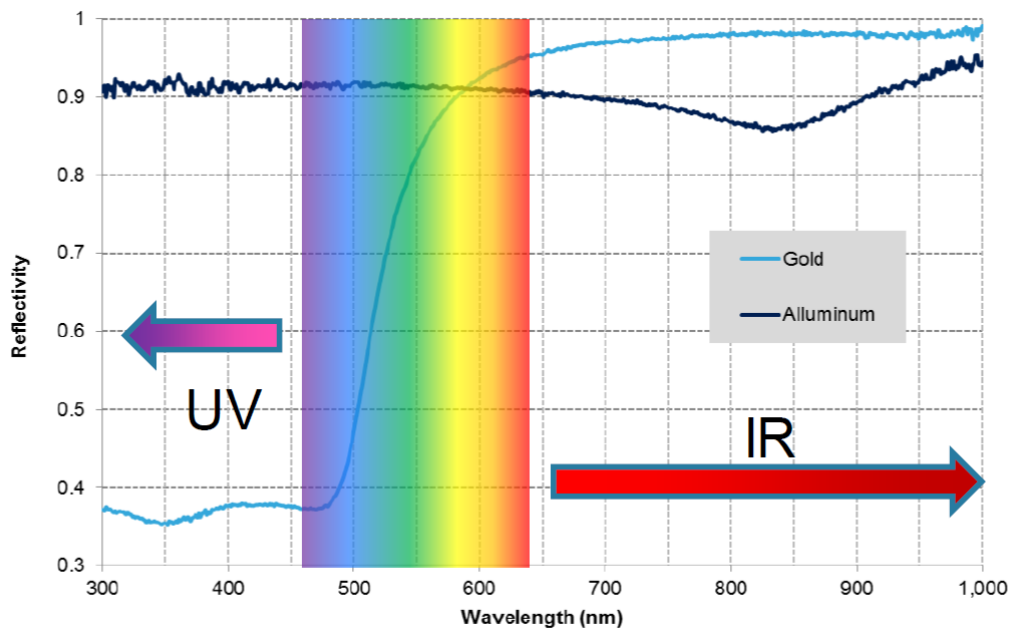
Figure 2.6: The graph shows how the reflectivity of aluminum (Al) and gold (Au) vary in different regions of the electromagnetic spectrum; this is the reason why depending on the application one material is chosen rather than the other. Adapted from ST internal reports

spectrum is needed (Al deposited on the mirror), as well as a small occupation volume and a low power consumption, because the final application includes a wearable device.

- **Projection**: in this case the application is more canonical, and the micromirrors are simply embedded in a projector as optical elements. Obviously, a projection in the visible is necessary (Al coating is preferred), and particular attention must be given to the quality of the mirror surface in terms of flatness, roughness and reflectivity, in order to guarantee high brightness and high resolution of the projected image.

- **Gesture & Face Recognition**: a facial recognition system is a technology capable of identifying or verifying a person from a digital image or a video frame from a video source, while for gesture recognition users can use simple gestures to control or interact with devices without physically touching them (many approaches have been made using cameras and computer vision algorithms to interpret sign language). Here the projection must be in the infrared range of the spectrum, as the use of IR also ensures that the feature works consistently regardless of the lighting conditions, so gold (Au) is the material used to cover the mirror. Moreover, a small occupation volume and a large angle of scanning are needed as these mirrors should be embedded in a portable or wearable device.

12

2.1.5 Micro-scanner Requirements

In this section the main requirements for a scanning micro-mirror have been reported.

For scanners, the highest resolvable spatial frequency is determined by the scan angle required to move the tip of the scan mirror by approximately $\lambda/2$. The motion of the scanner tip is proportional to the product of the scan angle and the mirror size. Thus, the total number of resolvable spots for the scanner is proportional to the product between scan angle and mirror size (θD-product), and inversely proportional to the light wavelength. Likewise, in scanning displays, display resolution requirement directly translates into a θD one, and the display refresh rate prerequisite translates into vertical and horizontal scanner frequencies (f_v and f_h). Both the θD-product and f_h (fast-axis in this case) are very important figures of merit for scanner performance comparison.

In calculating the required θD-product for a given display format, one has to take into account these factors:

- Beam profile across the scanner (e.g., clipping ratio of Gaussian beams[4]) and operation wavelength;

- Usable portion of the scan line (limitations due to sinusoidal motion of resonant scanners);

- Clear aperture size of the scanner;

- Modulation Transfer Function (MTF[5]) and contrast requirements of the display;

- Static and dynamic flatness of the scan mirror surface.

Other important requirements are related to scan repeatability and to the accuracy of information about scanner pose coming from position sensors. All of these parameters have a direct impact on display image quality and are discussed in the following sections. During this description the horizontal axis will be considered as the resonant one, and the vertical axis as the quasi-static one.

2.1.5.1 Resolution and Number of Pixels

As discussed above, the resolution is proportional to the θD product of the scanner. Besides the number of pixels, many other factors impact the θD requirements for the scanner. For instance, one important advantage of laser scanning systems is that one scanner can be used to redirect multiple beams simultaneously, thereby improving the horizontal or vertical resolution of the display. Multiline writing increases the line rate of the system by the number of beams.

---

[4]Gaussian beams are light beams where the electric field profile in a plane perpendicular to the beam axis can be described with a Gaussian function, possibly with an added parabolic phase profile[10]

[5]The MTF of a lens is a measurement of its ability to transfer contrast at a particular resolution from the object to the image. In other words, MTF is a way to incorporate resolution and contrast into a single specification[11]

When a multi-beam approach is considered, the general scan equation for horizontal and vertical resolution of a scanning display system can be written as:

$$N_h = \frac{4\theta_{MMSA}DK_spK_{os\_h}\cos(\alpha)}{K_Ta\lambda} \tag{2.5}$$

$$N_v = \frac{4\theta'_{MMSA}D'K_spK_{os\_v}\cos(\alpha)n_v}{K_Ta\lambda} \tag{2.6}$$

$$f_s = \frac{F_rN_v}{K_{ub}K_{os\_v}n_v} \tag{2.7}$$

Where:

N_h = horizontal resolution of display
N_v = vertical resolution of display
f_s = horizontal scanner frequency [Hz]
D = scan mirror size along horizontal axis
D' = scan mirror size along vertical axis
θ_{MMSA} = maximum mechanical scan angle amplitude (0-peak)
θ'_{MMSA} = maximum mechanical scam angle amplitude in vertical axis (0-peak)
θ_{TVSA} = total video scan angle ($\theta_{TVSA} = 4\theta_{MMSA}K_{os}$)
K_{sp} = spot size to pixel size ratio (typically $0.5 < K_{sp} < 2$)
K_{os} = overscan constants for horizontal and vertical axis ($K_{os} <= 1$)
K_{ub} = 1 for unidirectional and 2 for bidirectional scanning
α = feed beam angle (can be different for horizontal and vertical axis)
n_v = number of vertical feed beams
K_T = beam clipping constant
a = mirror shape factor ($a = 1$ for square/rectangular mirrors, $a = 1.22$ for circular ones)
F_r = frame rate or refresh rate for the display (typically $60Hz$)
f_v = vertical scanner frequency ($f_v = F_r$)

A K_{sp} of 1 corresponds to Full-Width Half Maximum (FWHM) overlap of adjacent pixels and is considered the optimal trade-off between raster modulation and Modulation Transfer Function (MTF). Larger K_{sp} values correspond to more overlap, which will lower contrast and MTF [12].
From equations 2.5, 2.6 and 2.7 it is possible to understand most of the dependencies regarding resolution of scanners. For a better understanding of all the variables and parameters reported above, it is suggested to consult [5].

2.1.5.2 Frequency and Pixel Timing Requirements

The resonant horizontal scanner moves faster at the center of the scan and comes to a stop at the extremities of the scan. K_os, already encountered in Section 2.1.5.1, defines the usable portion of the scan line. Within the disposable area, pixel time

Table 2.1: Some examples of parameters obtained for different display formats; this is extracted from [5]. The parameters are the following: F_r = Frame rate, equal to the vertical scanner frequency f_v (Hz); f_h = Horizontal scanner frequency (Hz); n_h = Horizontal Scan Pixel Number; n_v = Number of parallel scan lines; t_{ret} = Maximum retrace time allowed for vertical scanner (msec); t_{center} = Pixel-time at the center of horizontal scan line (nsec); t_{edge} = Pixel-time at the edge of the written area (nsec); f_{clock} = Maximum pixel clock frequency (MHz).

Display Format	F_r (Hz)	n_h	n_v	f_h (Hz)	t_{ret} (ms)	t_{center} (ns)	t_{edge} (ns)	f_{clock} (MHz)
VGA	60	640	480	15750	1.4	28.4	65.2	35.2
SVGA	60	800	600	19200	1.0	18.7	42.8	53.6
XGA	60	1024	768	24500	1.0	11.4	26.2	87.6
SXGA	60	1280	1024	16400	1.1	13.6	31.3	73.3
HDTV	60	1920	1080	17200	1.0	8.7	73.3	115.3

should be varied electronically to produce display pixels with equal width. The pixel time at the centre (t_c) and the edges (t_e) of the display can be expressed as:

$$t_c = \frac{K_{os\_h}}{\pi f_h N_h} \tag{2.8}$$

$$t_e = \frac{K_{os\_h}\sqrt{1 - K_{os\_h}^2}}{\pi f_h N_h} \tag{2.9}$$

The maximum allowable vertical retrace time t_{vret} can be expressed as:

$$t_{vret} = \frac{1}{f_v}\left(1 - \frac{N_v f_v}{2 f_h}\right) \tag{2.10}$$

Reducing the retrace time allows for smaller horizontal frequency and longer pixel times.

2.1.5.3 Raster Quality

Fig. 2.7 illustrates considerations of unidirectional and bidirectional scanning and certain advantages and disadvantages of each. Bidirectional scanning increases the light source utilization and reduces the required horizontal scanner frequency, both by a factor of 2. However, it requires buffering one line of data and displaying it in reverse order during backward sweep of horizontal scanner, as well as precise control of the phase between forward scan and backward scan lines, and finally can produce non-uniform line-to-line spacing across the scan line. The strong correlation between the simulation and actual systems can be seen by comparing the simulated results to those of the actual video display system. The text in the simulation is a 10pt font placed at the center and at the edge of the display. The non-uniform line spacing results in brightness variations and somewhat reduces the contrast modulation for points away from the center of the screen. The amount of usable screen width (TVSA) for the bidirectional scanning should be determined based on the display image quality requirements.

Unidirectional Scanning   Bi-directional Scanning
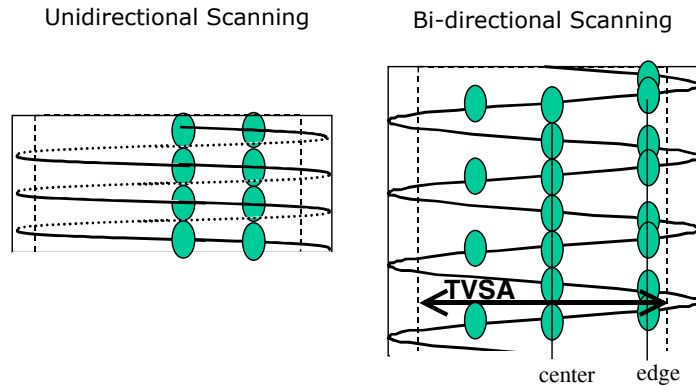
Figure 2.7: In figure is reported a comparison between unidirectional and bidirectional scanning. Adapted from [5]

2.1.5.4 Quality Factor

An important parameter to take into account during the design process is the quality factor, better known as *Q factor*. It is a dimensionless parameter that describe the efficiency of the studied device. More precisely it is a quantification of how underdamped an oscillator is, and characterize also a resonator's bandwidth relative to its central frequency. An high *Q factor* means a low rate of energy loss during oscillations, and so, for example, a resonator oscillating in air will have a lower *Q* with respect to one put in vacuum. *Q factor* is inversely proportional to the damping ratio (ζ), which describes the level of damping in a system, and more precisely $Q = 1/2\zeta$. Looking at Fig. 2.8, generally a system can be considered:

- *Overdamped* if $Q < 1/2$: in this case, due to the low quality factor (haigh damping ratio, $\zeta > 1$), the system doesn't oscillate at all and instead it slowly decay towards equilibrium (steady state amplitude of zero).

- *Critically damped* if $Q = 1/2$: it corresponds to an intermediate quality factor and, at this level of damping ($\zeta = 1$), the system approaches most rapidly the steady state amplitude of zero. Larger amounts of damping ($\zeta > 1$) cause the solution to approach zero more slowly, whereas smaller amounts of damping ($\zeta < 1$) cause the solution to oscillate more rapidly around zero.

- *Underdamped* if $Q > 1/2$: for systems with high quality factor the frequency of oscillation is very close to the undamped natural frequency $\omega_0 = \sqrt{\frac{k}{m}}$. Of course if Q is just a little bit higher than $1/2$ the system may oscillate just a couple of times before reaching the equilibrium and stopping the oscillation.

16
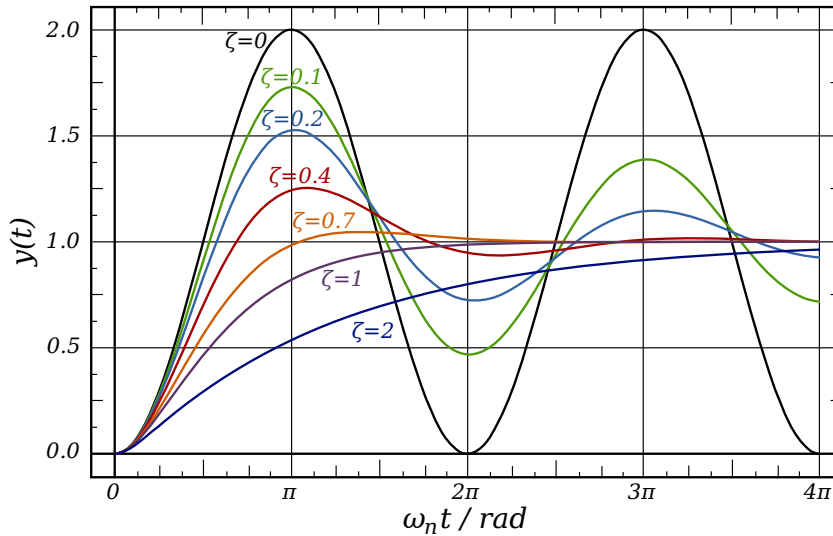
Figure 2.8: In figure are reported curves showing different oscillating behavior depending on the damping ratio ζ of the system. Adapted from [13]

2.1.5.5 Other Requirements

Several other factors can affect the image quality. For instance, the non-linearity of the vertical scan should be less than 0.1% across the vertical scan line. The horizontal scanner position and the frequency need to be determined very accurately and has to be monitored continuously. Line-to-line jitter[6] and frame-to-frame jitter depend on how accurately the scan position and the frequency can be synchronized with the data clock and the vertical scanner. The total jitter in the system should be at sub-pixel levels. If we assume a maximum of 1/8 pixel off-axis motion for the horizontal scanner, the jitter in the system including electronics, position sensor, and mechanical scanner should not exceed 3-4 nsec at 1σ.

Optical and mechanical design of the scanner housing imposes additional constraints in scanner design. Manufacturing and alignment tolerances become very tight for small scan mirrors. Small mirrors require large scan angles, and large scan angles result in focus errors and a non-flat image plane (i.e. field curvature). Field curvature can be corrected optically, but for low cost and low weight head-mounted display applications, there is no room for field correction lenses. All of this imposes a lower bound on the scanning mirror size.

2.1.5.6 Static and Dynamic Mirror Flatness

Both static and dynamic flatness of the scan mirror are important parameters for image quality. As illustrated in Fig. 2.9, high acceleration forces during mechanical deflection of the mirror result in bending of the mirror. Even very small amount of deviation from linearity due to mechanical deformation can result in optical distortion of the pixel and the image. Maximum deformation occurs at the

---

[6]Jitter is the variation in periodicity of a signal or periodic event from its target or true frequency
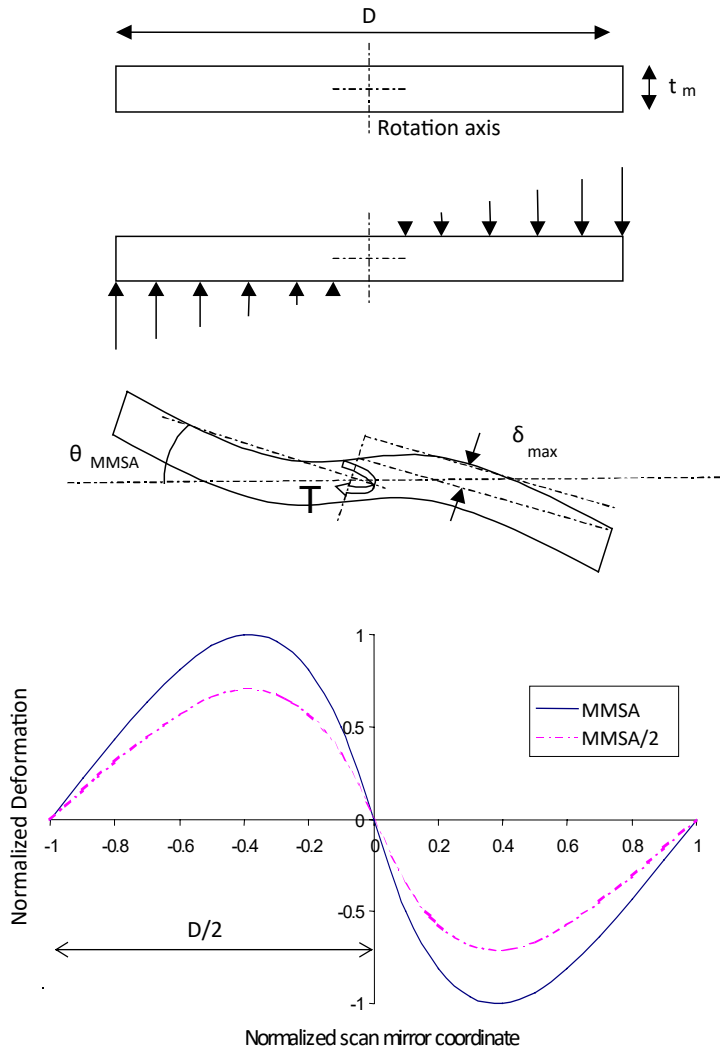
Figure 2.9: At the top a graphical representation of the dynamic mirror deformation is present; at the bottom the surface profile resulting from the deformation. Adapted from [5]

extremities of the scan. For rectangular block mirrors, the following equations can be used to compute mirror deformation, which is defined as the deviation from linearity:

$$\delta(u) = \frac{\delta_{max}(u^5 - 10u^3 + 20u^2 - 11u)}{1.83} \tag{2.11}$$

$$\delta_{max} = 0.217 \frac{\rho f^2 D^5 \theta_{MMSA}}{E t_m^2} \tag{2.12}$$

Where:

u = Normalized mirror surface coordinate perpendicular to rotation axis;
ρ = Material density;
E = Young modulus of the material;
f = Scanner frequency.

Fig. 2.9 shows also the shape that the mirror surface takes as a function of u ($u = \pm1$ corresponds to the edges of the mirror). As seen from the figure, the

18

deformation is symmetrical with respect to the center of the mirror. For the kind of aberration the mirror introduces, the maximum mechanical mirror deformation (δ_{max}) should not exceed $\lambda/10$ ($\lambda/5$ optical path difference) of the shortest system wavelength. This will permit the spot to remain diffraction limited across the scan line. Note that δ_{max} is proportional to $D^5\theta$. Due to high sensitivity to changes in D, if the system performance is deformation limited, significant gains can be attained by slightly reducing the mirror size.

2.2 State of the Art

In the following sections the state of the art of micro-mirrors is reported, according to the overview presented in [14] and other sources found in literature.

2.2.1 Electrostatic Micro-mirrors

Torsional electrostatic micro-mirrors are the most diffused among kind of devices, as they were the first to be studied and produced. Their functioning consists in the application of a voltage between movable (rotors) and fixed (stators) electrodes, so that the mirror rotates around the torsional axis until the electrostatic and restoring torque reach the same value:

$$T_e(\theta) = \frac{V^2}{2}\frac{\delta C}{\delta \theta} \tag{2.13}$$

$$T_e(\theta) = k\theta \tag{2.14}$$

where V is the applied voltage, $C = (\epsilon_0 A)/g$ is the capacitance of the actuator (ϵ_0 is the permittivity in free space, A is the overlap area of the electrode and g the gap between moving and fixed electrodes), θ is the rotation angle and k is the spring stiffness.

The principal configurations for this kind of scanning micro-mirrors are *parallel plates* and *interdigitated combdrive*, which are both shown in Fig. 2.10.

2.2.1.1 Electrostatic Parallel-Plate Scanner

A work proposed several years ago about bi-axial electrostatic micro-mirrors have been proposed by *Fan et al.*[15]. The micro-mirror, realized by the MESA[7] technology, is attached to a pair of suspended frames through two sets of orthogonal torsional beams and can be rotated around two axes by applying an electrostatic force between the mirror and the quadrant electrodes on the substrate. The outer frame is connected to four side-support plates by micro-hinges that, if pushed inwards simultaneously, can raise the center plate above the substrate. By applying bias to electrode 1 and 2, the mirror is rotated around the Y-axis, while

---

[7]Micro-Elevator by Self-Assembly; it's a technology that allows to rise the surface micro-machined plates to several hundreds of μm above the wafer surface
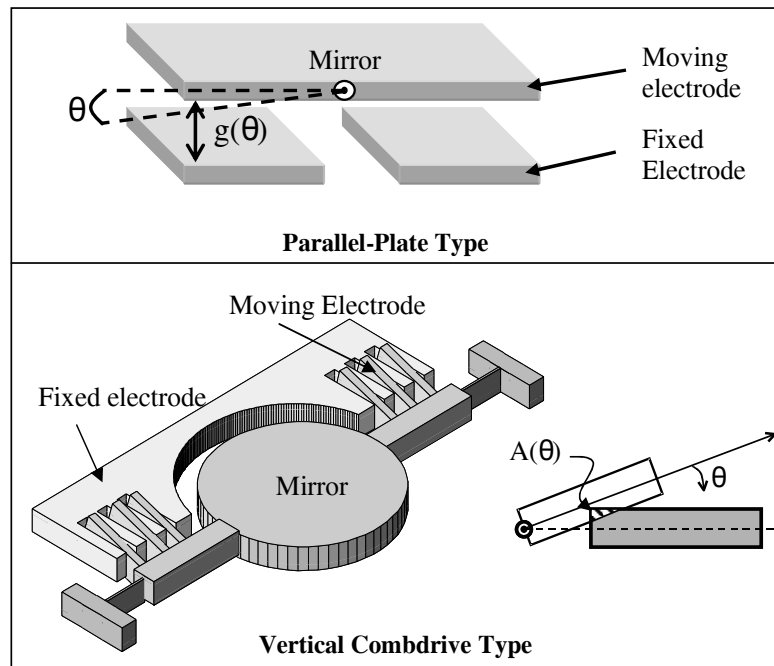
Figure 2.10: In figure is reported a representation of the two main configurations for electrostatic micro-mirrors: parallel plate type (Top) and vertical combdrive type (Bottom). Adapted from [14]

switching the bias is to electrode 2 and 3, the mirror is rotated around the X-axis. The maximum deflection angle reached is about ±14° with a pull-in voltage of 70 V, that could be lowered by means of thinner torsional beams. The resonant frequency of the scanner is about 1.5 kHz.

2.2.1.2 Electrostatic Comb-Drive Scanner

An example of this kind of micro-mirror is shown in Fig. 2.1, and it was studied in some works in collaboration with *STMicroelectronics*[16]. The device has been fabricated with a dedicated SOI[8] technology. The reflecting mirror is supported by two coaxial torsional beams. Four sets of 33 fingers each are anchored to the trapezoidal regions directly attached to the mirror, and they are interdigitated with their stator counterparts, forming a comb drive structure that provide the electrostatic actuation mechanism. The torsional natural frequency of the micro-mirror is f_0 =5370 Hz. In standard working conditions the device is excited near the resonance peak with a driving square wave at 130 V, reaching a deflection angle of almost 30°. However, this micro-mirror is actuated by means of *parametric resonance*, whose principle has been shown in 2.1.2; in this way, driving at 10 kHz with 110 V, more than 30° are achieved.

---

[8]Silicon-On-Insulator

2.2.2 Electromagnetic Micro-mirrors

Jeong et al[17] presented a slow-scanning electromagnetic micro-mirror for mobile application. The device is characterized by small size and low power consumption, and it is designed to be actuated through Lorentz force, by means of a current flowing in a coil, in presence of a strong magnetic field generated by two static magnets (Fig. 2.11). The scan angle reaches 8° with 45 mA input. In order to minimize device size, the mirror surface is placed on the opposite side of the coil actuator so that the coil and mirror shares the moving structure. Due to the size reduction, the rotating inertia is drastically reduced and the magnetic field density between magnets can be increased. As result, driving power is minimized granting a power consumption of about 55 mWrms.
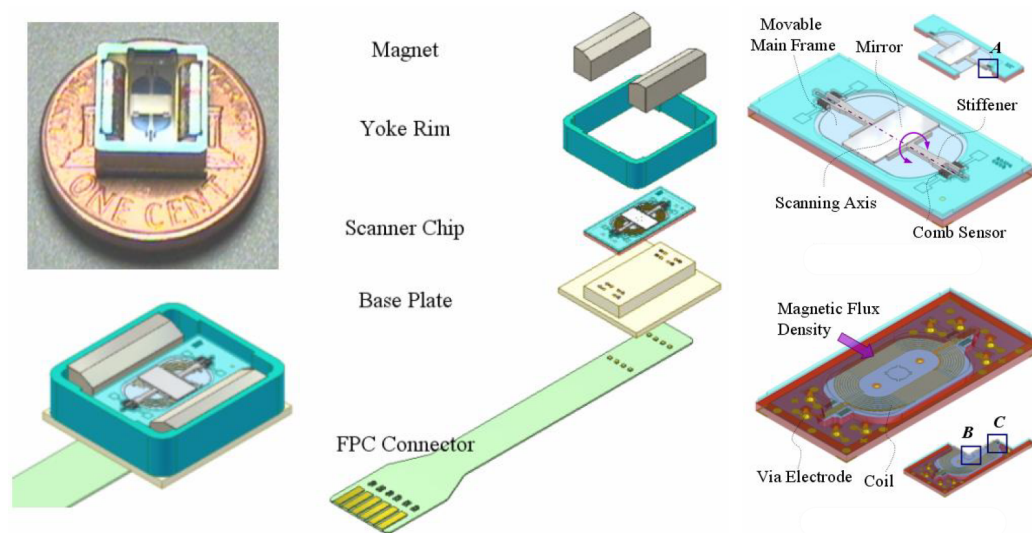
Figure 2.11: In figure is reported a picture and a representation of an electromagnetic micromirror; it is possible to notice the presence of a coil through which a current can flow, and two magnets which guarantees a proper magnetic field, in order to activate a Lorentz force. Adapted from [17]

2.2.3 Piezoelectric Micro-mirrors

More recently piezoelectric materials have been studied more and more, with a consequent improvement in their process technology and applications. *Gu-Stoppel et al.*[4] presented an uni-axial piezoelectric resonant micro-mirror, whose actuation is achieved using PZT[9]. Compared to other driving principles, this one is less affected by air damping and thermal or magnetic interference. The micro-mirror is driven by two bimorph actuators which are connected via top and bottom electrodes: the bending of thee actuators allows the mirror to rotate around its axis. The device showed a total optical scan angle of up to 42.5° at a frequency of 32 kHz when driven by one actuator with a unipolar rectangular pulse signal of 7 V, while with a driving signal of 2.5 V, the maximum scan angle was about

---

[9]PZT is a piezoelectric material, and stands for lead-zirconate-titnate

18° at a frequency of 31.4 kHz. To resume, the device features large deflection, high resonant frequency and Q-factor, and also requires low driving voltage to function.
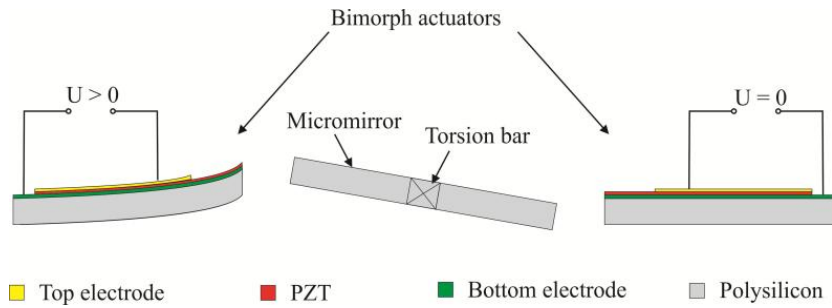
Figure 2.12: In figure is reported a cross-section of a piezoelectric micro-mirror driven by two PZT bimorph actuators. Adapted from [4]

CHAPTER 3

Electromagnetic Micro-mirror

This chapter gives a brief overview of the project carried on by *STMicroelectronics* and its contractor in the last few years. Its goal is the design, qualification and finally industrialization of an electromagnetically actuated micro-mirror working in the near-infrared spectrum, which is simply called *Porcino* for its mushroom-like structure. Different versions of Porcino have been developed, aimed at solving problems of various kinds (mechanical, electrical, optical, etc . . .) encountered during the project (as reported in section 3.6). It is worth noticing that *ST* dealt only with the MEMS micro-mirror, as package and driving system were property of the customer. This led inevitably to additional difficulties in the project and qualification phase.

3.1   Device Description

Porcino is an electromagnetically actuated micro-mirror that works in the near-infrared spectrum. Some images are reported in Fig. 3.1, Fig. 3.2a and Fig. 3.2b, in which it's possible to recognize all the components of this device.

As Porcino is a bi-axial micro-mirror, its structure and driving system are rather complex. The two main axis are distinguished as follows: the one aligned with micro-mirror oscillation is called *fast-axis* (because it involves oscillations at high frequencies, in resonance), while the other one is called "*slow-axis*" (perpendicular to fast-axis, with low-frequency oscillations, in quasi-static mode).

 Looking to the pictures, it is possible to notice the frame, which occupies most
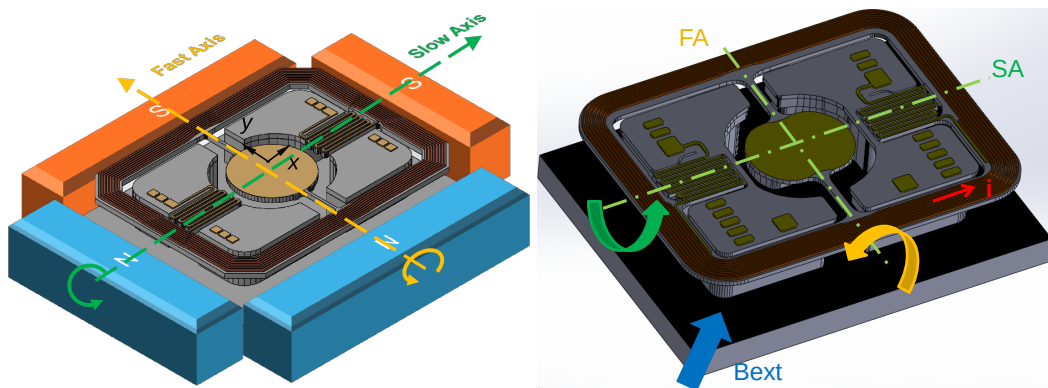
Figure 3.1: In figure two 3D representations of Porcino micro-mirror is reported.
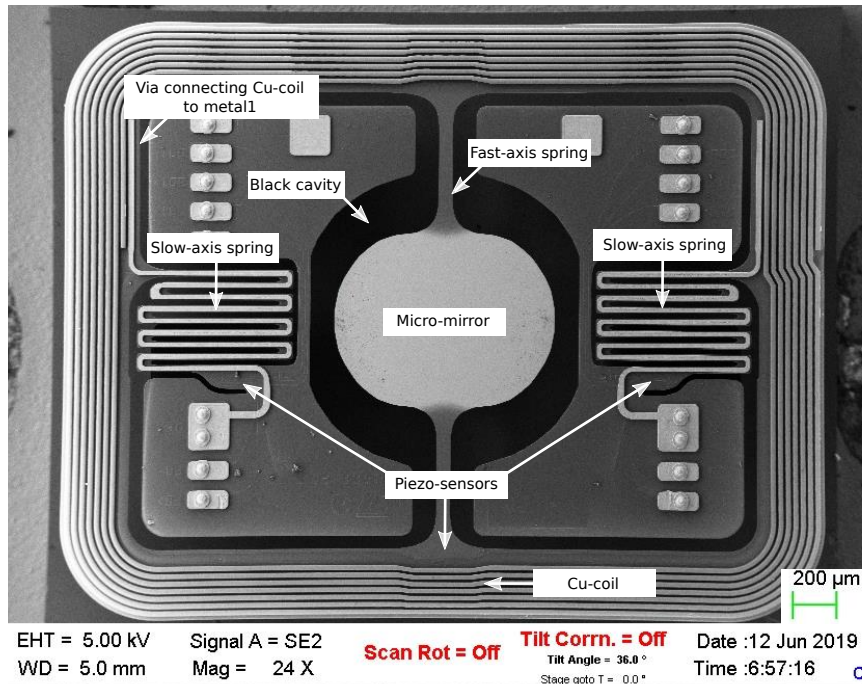
(a)
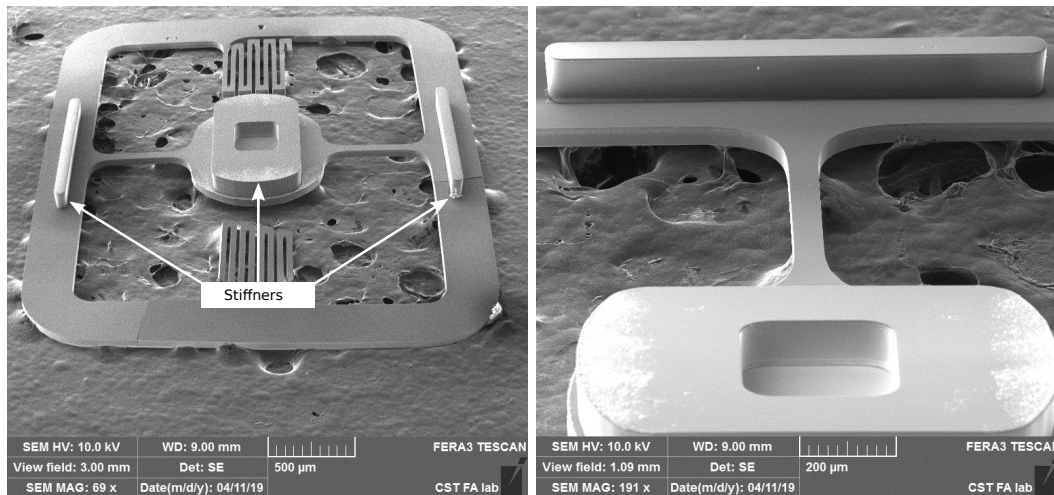
(b)

Figure 3.2: In Fig. 3.2a a top view of Porcino micro-mirror is showed. Picture have been taken with a SEM. In Fig. 3.2b are reported two pictures of Porcino's backside. "Stiffners" behind mirror and fast-axis anchorage points on the frame are visible.

of the object's surface. Around the structure there is a set of four magnets (see Fig. 3.1), which generate the magnetic field necessary for Porcino's electromagnetic actuation (the resultant of the magnetic field is diagonal).

Running along the outer part of the frame, a coil made of copper (Cu) can be found, through which a current can flow between two driving pads. The main purpose of the coil (by coupling with the external magnetic field) is to generate the driving force necessary to actuate the MEMS.

In the central portion there is the micro-mirror itself, which is covered with gold

24

to guarantee high reflectivity in the near-infrared spectrum (in which the device works). The mirror is anchored to the frame by means of a stiff torsional spring, which allows a high frequency oscillation of the mirror around fast-axis (it must be rigid, so that resonance frequency of its torsional mode is quite high, $f_0 \simeq 21\text{kHz}$). Instead, along the slow-axis two folded springs are placed, which favor the quasi-static oscillation of the frame (they are not very rigid, $f_0 \simeq 600\text{Hz}$). Under the mirror it is possible to see a dark cavity, which is called "*black cavity*". It is important that surfaces of this one are the least reflective possible, so that no extra reflection points are created during operation (projection through reflection of an incident laser beam). To avoid this, it presents a certain level of roughness. A set of three piezoresistive sensors (consisting in Wheatstone bridges), one placed on the fast axis, and two on the slow axis, allows to drive and monitor the MEMS. These have an important role, as they determine the device sensitivity, which is the ratio of the unbalanced bridges outputs to the mechanical angle reached on that axis. The reason why there are two of them on the slow-axis is that in this way it is possible to exclude spurious asymmetric movements from the calculation (such as *pitch*, see section 3.2), since the output resulting from the sum of the two sensors becomes zero.

Some silicon-oxide supports are present under the mirror and under the fast-axis spring, at its anchor points with the frame. They are called "*stiffners*" and their task is to improve the stiffness of these parts and to balance the MEMS mass.

Finally some pads are visible on the frame surface. Two of them are used to receive the driving signal, while the others allow to send the input signal to the sensors and to receive the output one, so that the system can be monitored.

After dicing, the final sizes of the die alone are $3.53\,\text{mm} \times 2.80\,\text{mm} \times 0.89\,\text{mm}$.

3.2 Actuation Mechanism

In this section the actuation mechanism of Porcino will be explained.

Porcino is a micro-mirror electromagnetically actuated exploiting the *Lorentz force*, generating when a current flows in presence of a magnetic field, as already reported. This is achieved by means of the copper coil inside which current flows, and four large static magnets, one on each side of the frame.

Lorentz force acts on moving electrical charges, and thus, as they are usually bounded to a wire (inside which current is flowing), the magnetic forces are transferred to the wire itself. This force is at a maximum when current and field are perpendicular to each other. Lorentz force is given by:

$$d\mathbf{F} = id\mathbf{l} \times \mathbf{B} \tag{3.1}$$

where $\mathbf{F}$ is the generated force, i is the magnitude of the flowing current, $\mathbf{l}$ is a vector which describes the length of the wire in which current is passing and its flowing direction, and $\mathbf{B}$ is the magnetic field.
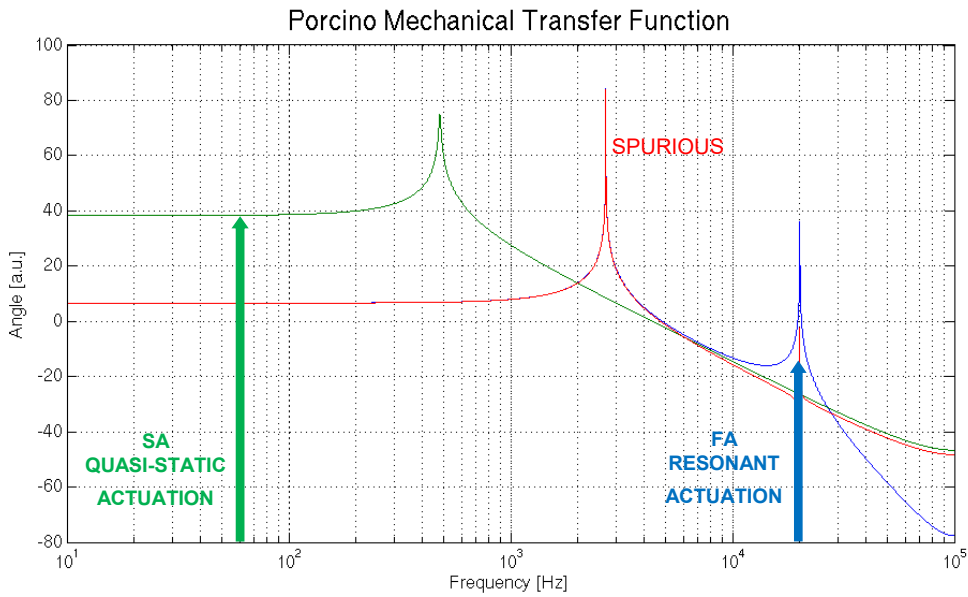
(a)
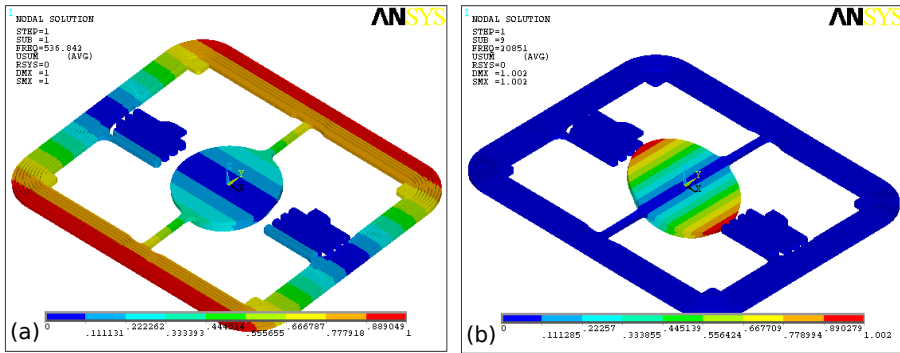
(b)

Figure 3.3: Porcino's mechanical transfer function is reported in Fig. 3.3a. It is possible to note the frequencies of the two driving signals, one at ~60 Hz for the slow axis, which is driven in quasi-static mode, and one at ~21 kHz for the fast axis, driven in resonant mode. Finally a peak at ~2500 Hz is noticeable, which represent a spurious, undesired mode for the system.
Simulations of Porcino's oscillation modes are reported in Fig. 3.3b. On the left, the slow-axis oscillation at ~60 Hz, (quasi-static mode) is shown; on the right, the fast-axis oscillation at ~21 kHz (resonant mode) is present. This image is courtesy of the Design Team of *STMicroelectronics* and should be looked at by consulting Fig. 3.3a.

The configuration of the pairs of magnets around the frame is such that the generated magnetic field has a diagonal resultant. Furthermore the size of the magnets is not the same on the two axes. Indeed, those placed on the slow axis are larger than those on the fast axis, so the two components of the diagonal magnetic field are not the same (that aligned to the fast axis is stronger than the one along the slow- axis).

From a mechanical point of view, Porcino can be described as a DC motor, with its corresponded motor torque.
Finite elements (FE) magnetic simulations of the magnetic assembly have been

done by Design Team of *STMicroelectronics*, that have taken into account the motor torque constant ($K_T(\theta)$ = torque produced divided by armature current) as a significant quantity to describe the magnetic torque. Practically, $K_T(\theta)$ synthesizes the coupling between the magnetic field and the geometric structure subject to force, that is the Cu coil. It is a θ-function because the integral of the Lorentz forces along the coil has significantly different values by rotating the coil itself in space.

From results it can be assessed that the slow-axis oscillation is more "efficient" with respect to the fast-axis one, being K_T always higher in the first case, with a maximum of 2.5×10^{-5} Vs with respect to 1.5×10^{-5} V s. This means that less current is needed to reach the same opening angle in the oscillation around the slow-axis with respect to the fast-axis. More properly, at equal flowing current the opening angle is higher on the slow-axis side.

From the dynamics point of view, Porcino can be modeled as a damped harmonic oscillator, and dynamics of its three main movements is well described by the coupled motion equations:

$$J\frac{d^2\theta}{dt^2} + b\frac{d\theta}{dt} + k\theta = T(\theta) \tag{3.2}$$

where J is the moment of inertia, b the damping coefficient, k the stiffness, and T the torque.

Looking to eq. (3.2), damping for Porcino comes from the air drag, acting on the mirror surface during its rotation. Considering the relation between Q-factor and damping coefficient ($b = 1/2Q$), an analytical model has been made and validated by the Design Team of *STMicroelectronics*. It shows that the higher is the mirror opening angle, the lower is the resulting *Q factor* (see Fig. 3.4). What turned out was $Q \simeq 1400$ for angles $\simeq 6°$, and $Q \simeq 600$ for angles $\simeq 15°$, thus, Porcino falls well within the category of underdamped systems.

Considering again eq. (3.2), as stiffness is related to resonance frequency ($f \propto \sqrt{k/m}$, where m is the mass of the system), depending on the frequency of the driving signals, different oscillation modes can be activated on Porcino.
For example, the two frequencies indicated in Fig. 3.3a are related to a precise movement reported in Fig. 3.3b, which correspond to the desired oscillations of the MEMS. In particular, Porcino is driven with an alternate current composed by two different signals: one is a sinusoidal wave at 60 Hz (most common refresh rate for displays), which drive the slow-axis in quasi-static mode, and one is a square wave at 21 kHz that drive the fast-axis in resonant mode.
As noticeable, the current at 60 Hz also excites a spurious oscillation mode (red curve in Fig. 3.3b), so, even if the amplitude is quite low, this movement will be present in the global actuation of the MEMS.
 More in details, as Porcino is designed, three different movements are generated:

- a wide oscillation around the slow axis, generated by the current signal at

Q-factor vs Angle
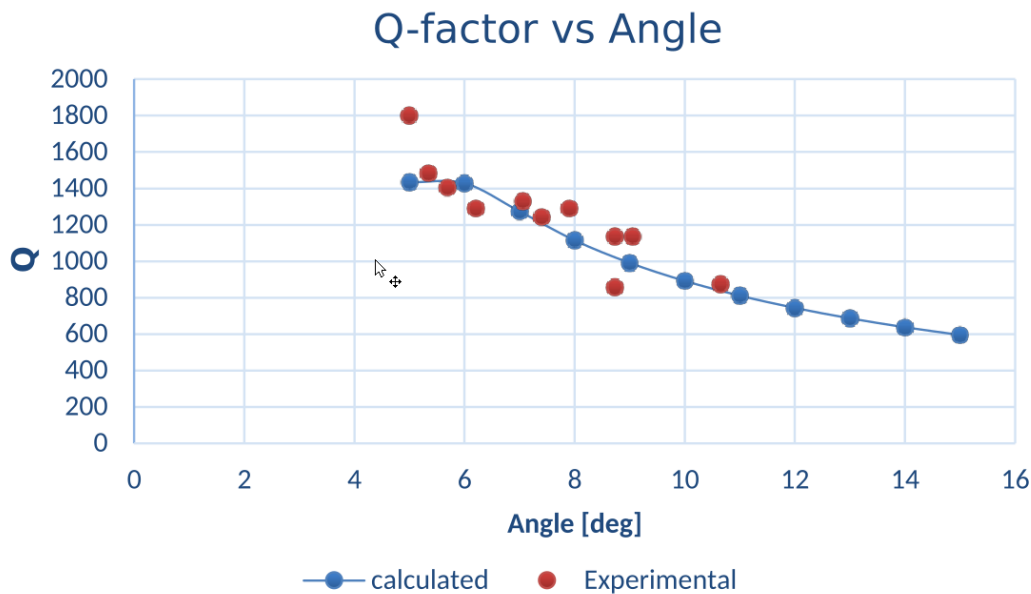
Figure 3.4: In figure is reported the Q-factor of Porcino at different operating conditions (in terms of opening angles).

60 Hz in presence of the resulting magnetic field, favored by the presence of the two folded, less rigid springs (see Fig. 3.3ba);

- a slight, but still present, oscillation of the frame around the fast axis (called *pitch mode*, whose peak is at about 2500Hz, visible as the third mode in Fig. 3.5) generated by the fact that the current at 60 Hz also activate this spurious mode. For this reason, when slow-axis is projected on a plane appears not perfectly straight, but slightly inclined;

- a very fast oscillation of the whole frame, generated by the magnetic field and the current signal at 21 kHz. This movement is consequently transmitted to the fast-axis spring, whose torsional oscillation mode has its own resonance frequency around 21 kHz, and therefore the central mirror can be actuated with a minimum energy consumption (see Fig. 3.3bb).

Anyway, depending on the frequency of the driving signal, much more modes could be excited, as visible in Fig. 3.5. Thus it is important to choose driving signals with frequencies quite distant from those of undesired modes, in such a way that these are not activated, or at least in a non relevant way.
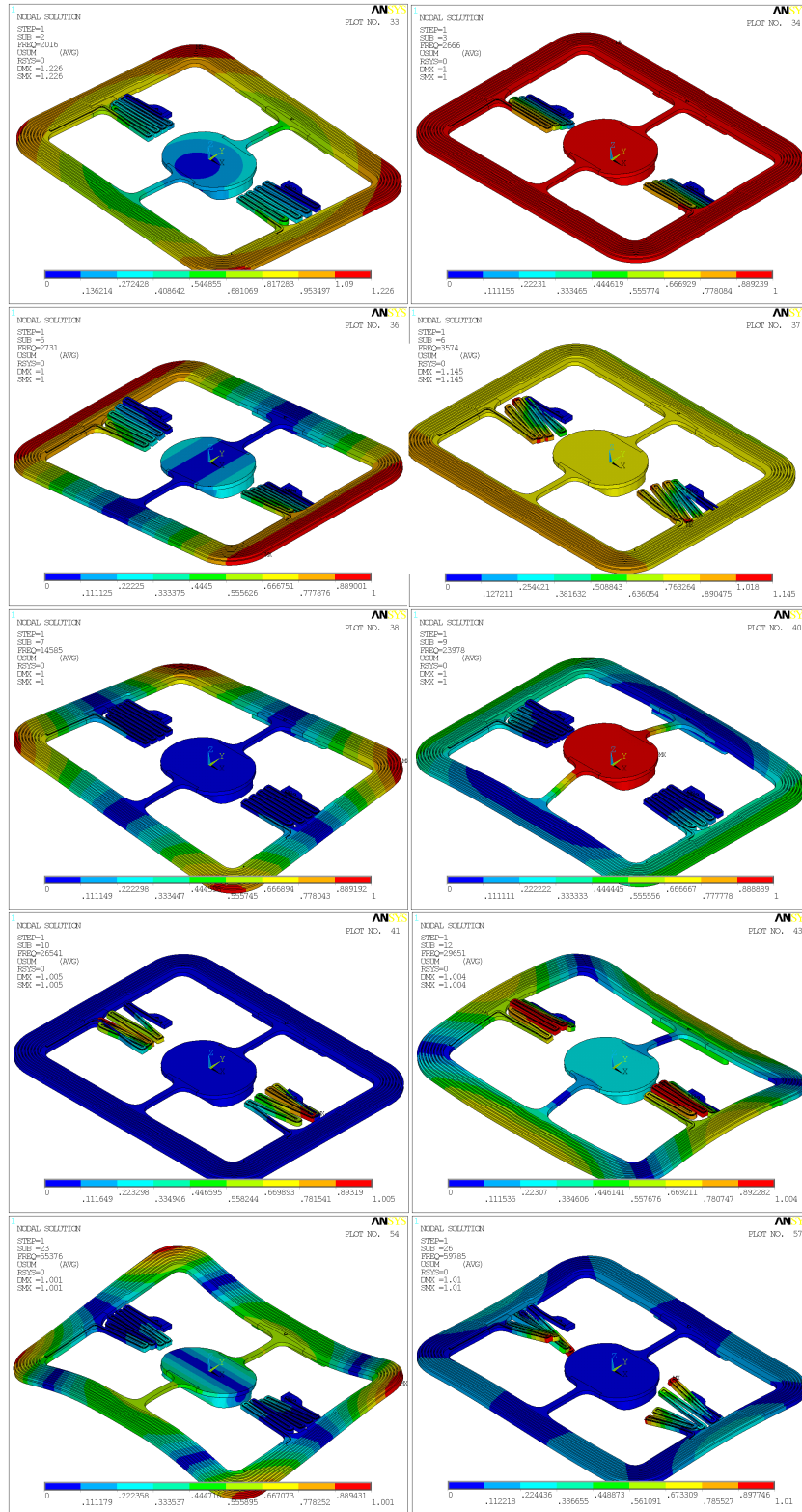
Figure 3.5: Simulations of Porcino's oscillation modes are reported in figure. From the top and from left to right, the oscillation modes related to driving signals at the following frequencies: 2016Hz, 2666Hz, 2731Hz, 3574Hz, 14585Hz, 23978Hz, 26541Hz, 29551Hz, 55376Hz, 59785Hz.

3.3 Sensing System

Porcino's functioning is monitored by means of three piezoresistive sensors (PZR), using a standard Wheatstone bridge configuration. Two sensors are placed on the slow-axis, near the folded springs, in order to decouple slow-axis and pitch movements, while the third one is located at the anchoring point of fast-axis spring. PZR sensors exploit the piezoresistive effect of silicon to monitor the mechanical angle opening of the micro-mirror. Indeed, in presence of stress, silicon resistivity changes, and from this variation it is possible to go back to the torsional stress close to the springs anchoring points. In this way, it is possible to indirectly evaluate the mechanical opening angles on both axes. In order to have the highest possible response to the mechanical torsion of the springs, PZR sensors are realized in correspondence of these positions, as visible in Fig. 3.6.
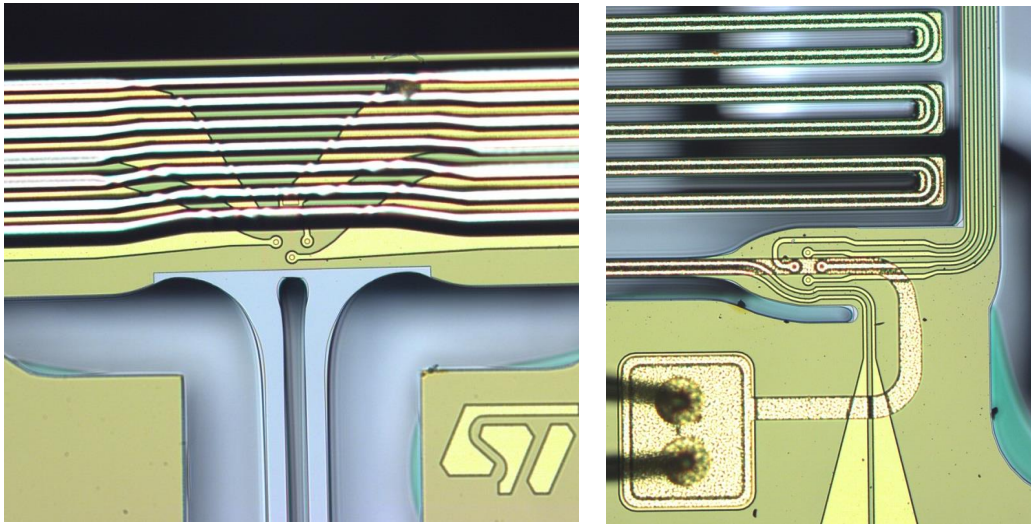
Figure 3.6: In the pictures are reported the piezoresistive sensors in Wheatstone bridge configuration of Porcino. On the left the one on the fast-axis spring anchoring, while on the right the one on the slow-axis spring anchoring point.

As the desired slow-axis oscillation (*roll*) generate an in-phase springs rotation, the bridge output will be not null. Instead, for the unwanted pitch movement the rotation of the spring is in anti-phase, and so the bridge output will be equal to zero, thus not interfering with the device monitoring on the two main axes.

As already said, to sense the piezoresistive effect due to shear effect, a standard Wheatstone bridge configuration is used (Fig. 3.7). The output voltage from the bridge is given by:

$$V_{out} = \frac{\Delta R}{R} V_{bias} = \alpha_{sensor} \theta_{MA} V_{bias} \tag{3.3}$$

Where α_{sensor} is the sensor sensitivity ($\alpha_{FA} = 20\,\text{mV/deg V}$; $\alpha_{SA} = 1.9\,\text{mV/deg V}$) and θ_{MA} the mechanical opening angle.
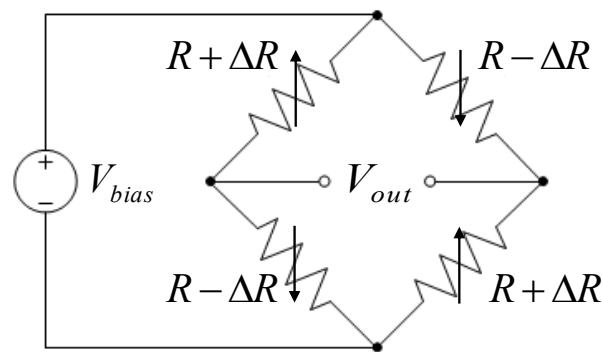
Figure 3.7: In the pictures is reported a general schematic of a Wheatstone bridge.

3.4 Driving System for Qualification

It must be pointed out that the driving system used by *STMicroelectronics* and that used by the customer are different, for example not only in the way they manage the output signals of the MEMS (PZR sensors output), but also in the driving signals themselves. Indeed the customer drives by current signals, while *ST* uses driving voltage signals. Obviously the operating conditions reached are the same in both cases, as the two quantities are linked by Ohm law ($i = V/R$) and that the intrinsic resistance of the device is equal in both cases.

Then, also waveforms used by the customer are different, indeed, for the resonant fast-axis they use a sinusoidal signal, while for the quasi-statics slow-axis a sawtooth one.

It is worth mentioning that if a system is driven in a static or quasi-static way, its mechanical response will have the same waveform as the incoming signal. If instead it is driven in resonance, its response will always have a sinusoidal waveform, no matter what the driving signal is.

Furthermore, ST system works in open-loop[1] on mechanical angles and slow-axis spring frequency, while in closed-loop[2] on the fast-axis spring frequency. Instead, the customer guides in closed-loop both on the angles and on the fast and slow-axis frequency, so as to keep the functional parameters of the device always constant.

As the two driving systems are different, let's analyze the one used by *STMicroelectronics*.

As reported above, *STMicroelectronics* only deals with the MEMS. Indeed, wafers with micro-mirrors are produced internally and then are delivered to the cus-

---

[1]Open-loop means that the driving system gives an input to the device, without reading any received output.

[2]Closed-loop means that the driving system gives an input to the device, reads the output received and modifies the following input in order to maintain a certain working condition.
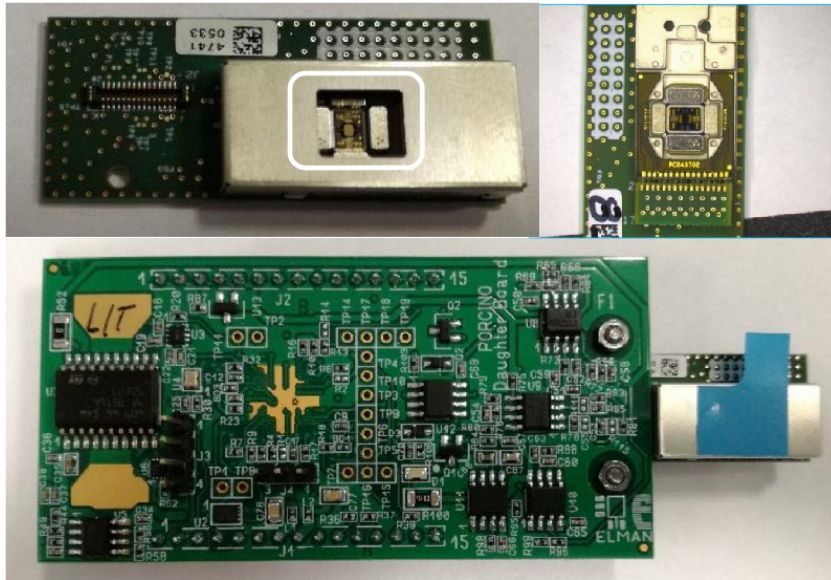
Figure 3.8: In figure, Porcino's test vehicle (top pictures) and daughter-board (bottom picture) are shown.

tomer, who assembles each device on a test vehicle (TV). This is then mounted on a driving board (called *daughterboard*) designed for Porcino in *STMicroelectronics*, which allows to electrically drive it and to perform all the measurements necessary for the qualification. These elements are reported in Fig. 3.8.

On the daughterboard is installed a microprocessor called GARNET. This system has been designed to be multi-purpose, satisfying all the possible conditions to which Porcino could be subjected (opening angles, uni-axial, bi-axial), giving different commands to the device, depending on the test to be performed (DC Test, Life Test, Power On-Off, see chapter 4).

Indeed it can be programmed in order to allow the various pads of the device to get the right driving signal, and to receive data collected by the sensors.

Another fundamental task of GARNET is to lock the resonance frequency of fast-axis spring torsional mode. As already mentioned, to do this it works in closed-loop on this parameter. Practically, if the MEMS undergoes a drift in resonance frequency (due for example to fatigue cycles), GARNET modifies the frequency of driving signal (voltage) to match it with the resonance frequency of the mechanical structure.

For sure, this type of system has disadvantages, such as the fact that it risks to introduce failure modes not typical of the final device. At the same time, another risk could be not to discover failures that would be typical only of the final system. However, *ST*'s driving system has been agreed with the customer, who confirmed its validity and its equivalence with their one (in terms of reliability). Taking these considerations, the eventuality of such problems should have been minimized, if not completely avoided.

3.5 Process Flow

In this section the process flow by which Porcino is fabricated is reported. In this way the reader can have a general idea of how this object is produced and why certain problems arise, which will be better analyzed in chapter 4.

Generally, Porcino can be divided into two main parts:

- a *sensor wafer*, which contains the active parts of the device (such as PZR sensors, mirror, metal vias, etc...);

- a *cap wafer*, that works as an handler for the sensor wafer, and creates the spaces necessary for the motion of its mechanical parts.

Fig. 3.9 tries to summarize the main process flow steps with a block diagram.
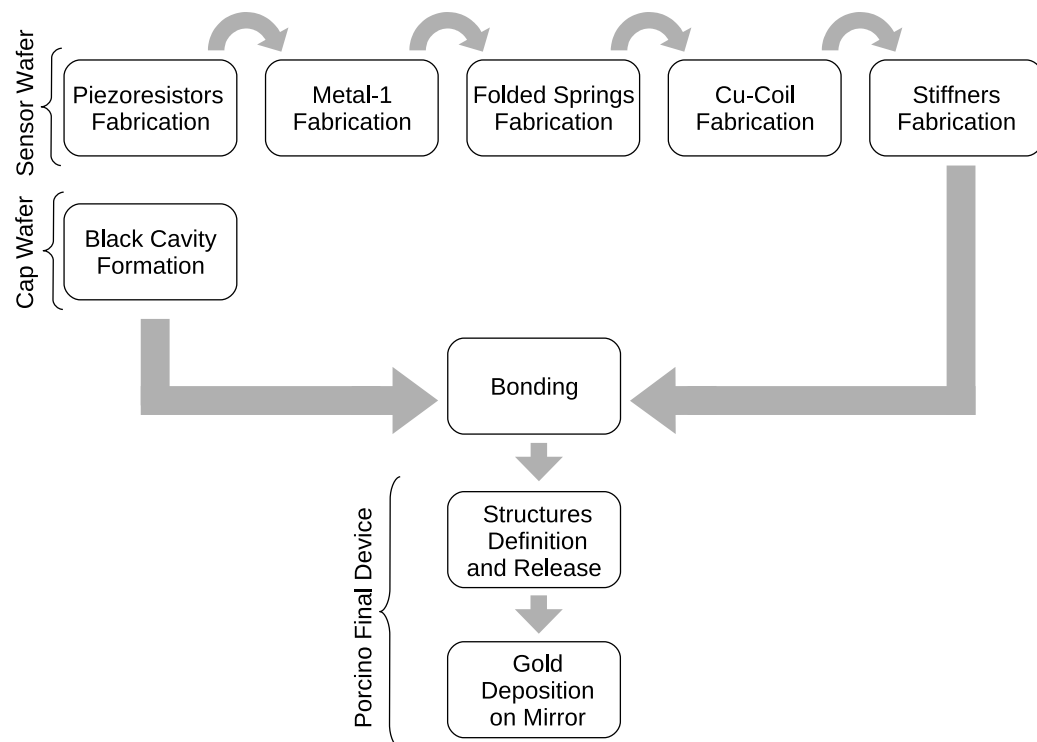
Figure 3.9: In figure is reported a scheme presenting the most important steps for Porcino fabrication.

3.5.1 Sensor Wafer Processing

The sensor wafer starts with an SOI (*silicon on insulator*) composed by 650μm of handle Si, 1μm of buried oxide (SiO$_2$) and 45μm of Si p-type substrate. On this substrate, an oxide layer of 200Å is grown, and it is the starting point on which the principal parts are built. In the following sections the fabrication of the main components of Porcino's sensor wafer will be explained. They includes: piezoresistive sensors, metal-1, folded springs, Cu-coil and stiffners.

3.5.1.1   Piezoresistors Fabrication

The manufacture of piezoresistive sensors consists in the implantation of dopant species that allow to create an imbalance in terms of potential difference, thus generating the structure of a Wheatstone bridge (see Fig. 3.10).

Through dedicated masks three different implants are carried out, directly through the oxide layer: n^-, n^+ and p^+.
The n^- implant is done using P_{31} with the following process conditions for implant energy and dose: $E_{impl} = 120\text{keV}$, $N_d = 1.2 \times 10^{13}$.
Regarding n^+ implant, also here P_{31} is used, but with energy about 40keV and higher dose ($N_d = 5 \times 10^{15}$).
Finally, for p^+ implant, B_{11} has been used, with $E_{impl} = 50\text{keV}$ and $N_d = 5 \times 10^{15}$.

After these steps, a 6000Å layer of TEOS (tetraethyl orthosilicate) is deposited through LPCVD[3], and an annealing is done in order to activate the implants.

Finally, contacts are defined by means of a mask and a dry etch step.
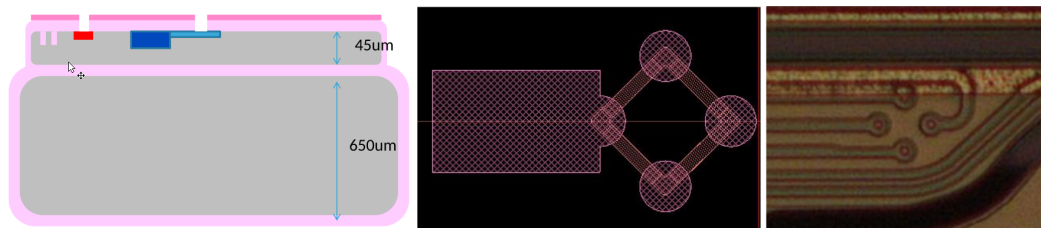
Figure 3.10: In figure are reported three images related to piezoresistor implantation on Porcino. From left to right: the Porcino's schematic cross-section, the mask related to this step, and a picture of the interested section

3.5.1.2   Metal-1 Fabrication

After the realization of the implants, metal-1 is deposited throughout the top surface. It serves to create all the vias necessary to make the input and output signals flow through the MEMS. It consists of multiple layers that are deposited over the entire surface of the device, and in particular /Ti 200Å/ TiW 1000Å/ Au 2500Å/ TiW 300Å. Through a series of masks, some etching steps (both of wet and dry type) are carried out so as to define the routes of the vias, as shown in Fig. 3.11.

---

[3]Low-pressure chemical vapor deposition
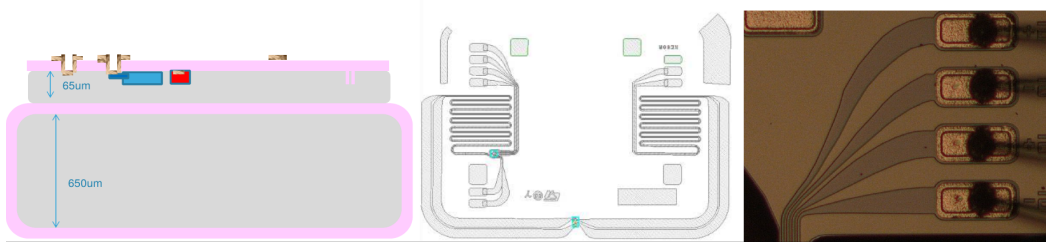
Figure 3.11: In figure are reported three images related to metal-1 fabrication on Porcino. From left to right: the Porcino's schematic cross-section, the mask related to this step, and a picture of the interested section.

3.5.1.3 Seed Deposition and Folded Springs Fabrication

After the definition of metal-1 a layer of 6700Å of SiN is deposited on the surface in order to isolate and protect the vias. Then, the opening of the vias on metal-1 occurs through dry etch.

After this step, a metal layer is deposited by sputtering and defined by etching masks. It is done by a metal stack made of Ti 200Å / Cu 2000Å / Ti 200Å. This layer act as a seed to grow the flexure springs and the coil.

Folded springs are grown as a three-layer metal stack made of Au 4µm / Ni 3µm / Au 7µm. This is done after removing the surface layer of Ti from the interested areas of the seed layer through an etching mask (see Fig. 3.12).
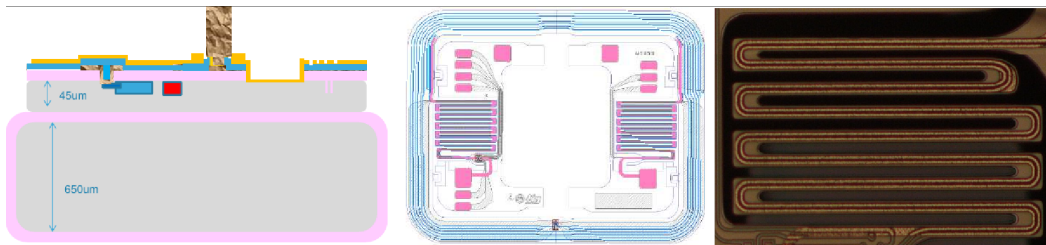
Figure 3.12: In figure are reported three images related to seed deposition and folded springs fabrication on Porcino. From left to right: the Porcino's schematic cross-section, the mask related to this step, and a picture of the interested section.

3.5.1.4 Coil Fabrication

After completing the folded springs fabrication, next step is the growth of the metal coil through which driving current will flow.
First of all, the seed layer is treated so that no oxides are present on top of it, and the Ti layer is removed in order to expose the Cu. After these processes, a coil mask is applied (30µm thick), and the coil growth must be done within 48h, so that no further oxide creates on the seed surface.
This condition is very important, because coil is grown by electrochemical deposition (ECD), and so the substrate surface must be conductive. Furthermore,
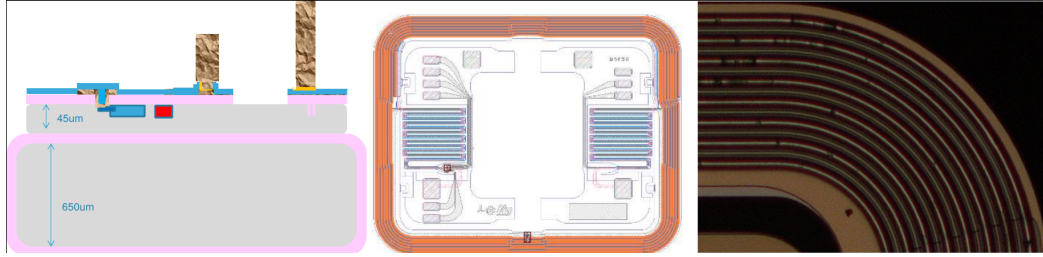
Figure 3.13: In figure are reported three images related to coil fabrication on Porcino. From left to right: the Porcino's schematic cross-section, the mask related to this step, and a picture of the interested section.

Ti layer is removed from the seed in order to have a good ECD growth in terms process of stability and repeatability.

The coil structure has been modified throughout Porcino development: until version 3.2 it was composed by Cu 21µm/ Ni 1µm, while starting from version 3.4 it turned into Cu 26µm/ Ni 1µm. This has been done in order to augment the maximum value of current the device can sustain without failing. Anyway, it is not possible to grow the coil more than that, because it becomes too high, and problems occur regarding the polymeric mask. The Ni layer on top of coil is added to enhance the corrosion resistance of the coil itself.

3.5.1.5 Stiffners Fabrication

Once the upper part of the sensor wafer is completed, it is covered by a polymeric layer which allows the bonding with a handler wafer. This is done because the following processing steps imply to work on the backside of sensor wafer, and thus, by using a handler, damages on its front side can be prevented.
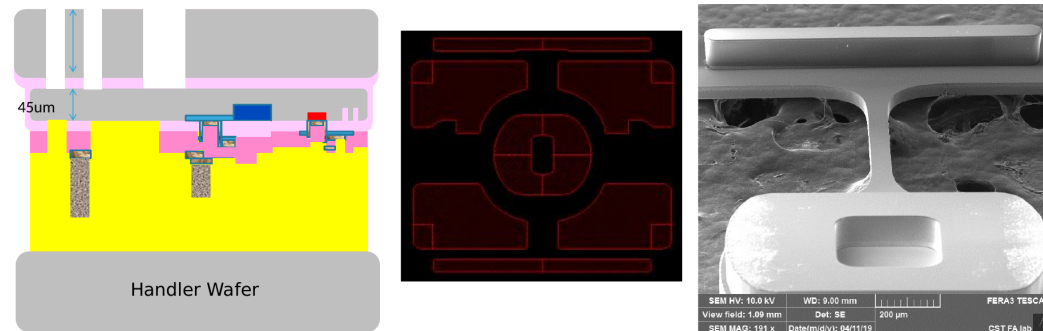
Figure 3.14: In figure are reported three images related to stiffners on Porcino. From left to right: the Porcino's schematic cross-section, the mask related to this step, and a picture of the interested section.

After the bonding with the handler wafer, the system is turned backside and lapped up to a thickness of 120µm.

Then, a mask on the backside is done. By dry etching, the silicon and oxide are removed, generating the so-called stiffners. As mentioned before, this structures help to increase the rigidity of the structure and to adjust its weight (see Fig. 3.14).

It is important to perform this process accurately, because otherwise the fabricated structures may be subjected to delamination problems during their fatigue life, leading to a loss in stiffness and so to a drift in the resonance frequency of the structure over time.

3.5.2 Cap Wafer Processing

At this point, another wafer is processed. It will constitute the cap wafer with which the structure of Porcino will be assembled.

3.5.2.1 Black Cavity Formation

As noticeable from Fig. 3.15, cap wafer has a cavity in correspondence of the coil and mirror areas, necessary to let it oscillate without hitting the bottom. It is formed through a dry silicon etching, using a proper mask and resist.

It is very important that this cavity, called black cavity, is the least reflective possible, in order to avoid possible problems during the application related to the creation of extra spots during laser projection. To do this, the bottom surface is treated through a dry silicon etching, so as to create a roughness that strongly reduces its reflectivity.

At the end of this process, surfaces of the cap wafer are covered with TEOS on the anchor points with the sensor wafer a glue is placed and cured.
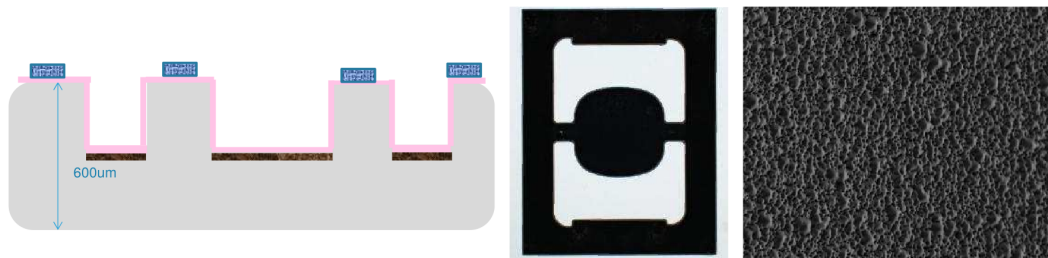
Figure 3.15: In figure are reported three images related to black cavity formation on Porcino. From left to right: the Porcino's schematic cross-section, the mask related to this step, and a picture of the interested section.

3.5.3 Bonding and Final Processing

When everything is ready, sensor wafer is permanently bonded to cap wafer, taking it by the handler and using the glue placed before on the cap wafer.

After that, handler wafer is removed and the surface of the sensor wafer is cleaned from the brewer, freeing all the contacts and elements of the MEMS.

At this point, mechanical structures such as mirror, springs and frame are opened, and they become free to move. This is done by using a proper mask (rotor mask) and a silicon etching procedure (see Fig. 3.16).

Finally, a multi layer of TiW and Au is deposited on the mirror surface by sputtering using a shadow mask, in such a way that none of it can reach the black

Figure 3.16: In figure are reported three images related to bonding, mechanical structure opening and gold deposition on Porcino. From left to right: the Porcino's schematic cross-section, the mask related to this step, and a picture of the interested section.

cavity. Gold is used in order to make the MEMS active in the near-infrared range of the EM spectrum.

A clear schematic image of the completed Porcino is reported in Fig. 3.17, where all the main components cited above are presents.
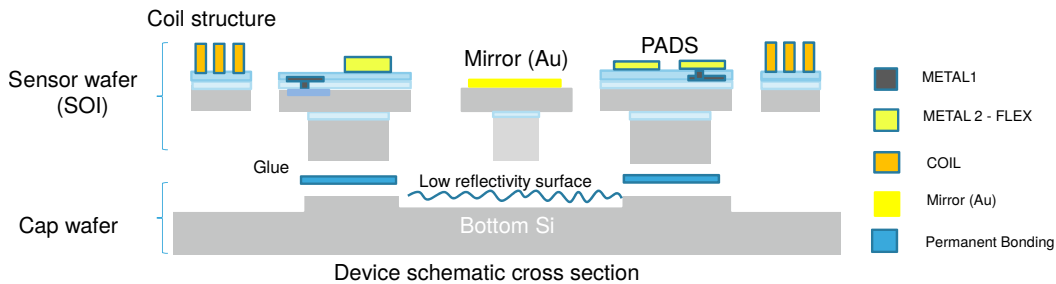
Figure 3.17: In figure is reported a schematic of the finite Porcino, with all the main components discussed in this chapter.

3.6 Micro-mirror Variants

It should be noted that different versions of Porcino have been designed and studied, in order to solve problems related to the design of older versions. In particular, for this thesis work, the considered versions are listed below, with a brief description for each of them:

Porcino 3.1 is the first official version of Porcino, and it is almost identical to its final design. This version is the one chosen, after preliminary studies, to be taken as the basis for carrying out qualification tests and for subsequent developments. In particular, with version 3.1 important parameters were set, for example frame size and metal materials (transition from Al to Au for metal-1), and it was verified that the device could withstand more or less all the tests (in particular life tests, mechanical tests and DC tests). Furthermore, a redesign was made so that fewer spurious modes were excited. Later versions do not introduce substantial changes to the MEMS, but rather try to improve it to solve various problems encountered during qualification.

Porcino 3.2 is the successor of Porcino 3.1. Mechanical and fatigue resistance were good, but the problem was that copper coil tended to oxidize too quickly with the typical driving current of the device (180-220mA for reliability tests), resulting incompatible with the customer driving system. It was the first version subjected to the actually used tests matrix and experimental set-up.

Porcino 3.4 has the thickness of the copper coil increased by 5 micrometers compared to version 3.2 (from 22 to 27 micrometers). Thus, current densities are lower, and coil tends to oxidize more slowly, resulting in an increase of driving currents that the device can withstand.

Porcino 3.5 has practically the same design as the previous version, with only some changes in the handle-wafer; from the functional point of view, there are no variations with respect to Porcino 3.4.

Porcino 3.6 has the same design as Porcino 3.5, but has been subjected to a change in the shadow-mask for depositing gold on the mirror, to prevent the underlying cavity from being contaminated, and therefore having a non-negligible reflection component that can cause problems during application. Once again, from the functional point of view there are no differences with respect to Porcino 3.4 and 3.5, but only a reduction of the mirror's reflective surface.

3.7 Requirements

The specs requested by the customer for Porcino micro-mirror are reported in this section.
The validation and verification of these requirements is not a task strictly related to Reliability and Design Team, but rather to Characterization one. However, there was a strong collaboration among these sides, which was fundamental to complete the objectives and adjust some critical parameters.

Obviously, the specs reported in Tab. 3.1 aren't the conditions that device should reach during operation, but rather the limit values that must be able to withstand during life without breaking or deteriorating. This is why, for reliability tests, for example the opening angles of the micro-mirror aren't set to $15° \times 20°$ with an RMS driving current of $200\,\text{mA}$, but rather to $14° \times 18°$ with a RMS current $\sim 150\text{-}160\,\text{mA}$, which are conditions much more representative of the real operating conditions of the device.
In any case, these topics will be better discussed in chapter 4, where the reliability test matrix will be presented.

Table 3.1: In the table are present all the spec requirements for Porcino micro-mirror, according to customer's requests.

Parameter	Minimum	Typical	Maximum	Unit
Laser wavelength	830	860	980	nm
Operating Temperature	0	40	60	°C
Power at full FOV (RMS)		250	300	mW
SA-FA axes coupling			0.025	deg
Mirror impedance (T_{room})		4.5	5.5	Ω
Mirror impedance ($T_{operative}$)		6	6.6	Ω
Coil temperature			200	°C
Coil inductance			0.5	μH
Optical power average (mirror)			0.3	W
Max current rating ($\geq$ 20ms) (RMS)			200	mA
Current at startup ($\leq$ 20ms) (RMS)			400	mA
Max absolute current ($\leq$ 25μs)			500	mA
Storage temperature	-40		85	°C
Solw-axis frequency	1	60	120	Hz
Fast-axis frequency	19500	21000	22500	Hz
Neighbouring modes frequency	-1000	f_{FA}	+1000	Hz
Mirror diameter along SA		1		mm
Mirror diameter along FA		0.76		mm
Mirror reflectance (Au cover)	90			%
MEMS die specular reflectance		10	15	%
Mirror scan angle stability			±1	deg
Mirror SA scan angle setting range			20	deg
Mirror FA scan angle setting range			15	deg
Mirror acoustic noise level			42	dB
Mirror flatness			$\frac{1}{4}\lambda$	
Mirror curvature	800			mm
Mirror surface roughness (RMS)			20	nm
FA Sensor bridge resistance	2		6	kΩ
SA Sensor bridge resistance	2		5	kΩ
FA Sensor sensitivity	4		12	mV/deg V
SA Sensor sensitivity	0.75		3	mV/deg V
Pitch Sensor sensitivity	8		18	mV/deg V

Reliability of the Electromagnetic Micro-mirror

"Innovation is something new or different that delivers value to the world, with the key criteria that I'm not innovating if I'm not bettering people's lives. Put simply, it is the future delivered" [18].

Television, personal computer and information technology, mobile phone, smartphone, wearable technologies (with all the sensors behind it) and so on, are all innovations that radically changed human life.

Innovation can be done in two different ways, both equally important, and sometimes interconnected in a synergistic way:

1. through basic scientific research, carried out mainly by universities or scientific laboratories;

2. through research and development for application purposes, carried out by industries, with the aim of setting up a production line.

Considering the industrial field, in which this thesis work was carried out, innovation includes a complex process flow that involves a high level of collaboration between different company teams (Design, Technology, Manufacturing, Characterization, Quality and Reliability, etc . . .), with the aim of bringing a device to a level of maturity such that it can be produced and commercially distributed.

Reliability is a fundamental part of this process, and its importance will be extensively explained inside this chapter.

4.1 Introduction to Reliability

Generally it is very important that a device is not only defect-free just after the production phase, but it should be also capable to perform its function without early failures for a declared period of time. This is true also in MEMS field, where emerging technologies require marketplace acceptance in order to be designed into high volume and for critical applications.

Reliability plays a fundamental role in this regard, as its purpose is to reproduce, in a much shorter period of time, the stress conditions to which a product would be subjected during its lifetime.

Furthermore, reliability does not guarantee a minimum level of defects to the customer, but it rather serves to direct the final design, so that in the end the device complies with specifications and a minimum lifetime period can be guaranteed. More in detail, reliability searches for possible intrinsic failure modes of a MEMS, that can be related to its design, process, packaging or application (e.g. fracture, creep, fatigue, stiction, short and open circuits, arcing, corrosion, dielectric charging, etc...). To do this, specific tests are carried out, each one aimed at stressing the device in well defined conditions, in order to put in evidence a specific failure mechanism, by applying highly stressing factors to the product, both of electrical and physical nature, separately or in conjunction (e.g. see scheme in Fig. 4.1). These considerations imply that test matrix may be different depending on the device under analysis and its application.
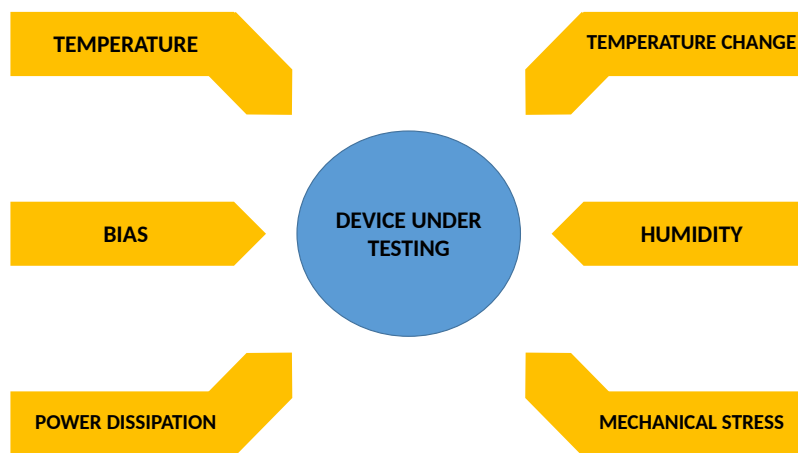
Figure 4.1: In figure is reported a simple scheme with some stress factors applicable to a device for reliability testing purposes.

4.1.1   Basic Concepts

Generally, there is no simple answer when asked if an object will work up to the limit imposed for its lifetime, and so if it is reliable; the only way to do this is to use concepts of probability and statistics. Indeed, the reliability of an item can be interpreted as follows:

"If n statistically identical items are put into operation at time t = 0 to perform a given mission and ñ ≤ n of them accomplish it successfully, then the ratio ñ/n is a random variable which converges for increasing n to the true value of the reliability"[19]

So, reliability is a characteristic of an item, generally designated by R, and it is expressed by the probability that the item will perform its required function under given conditions for a stated time interval. In a qualitative way, reliability can be considered as the ability of an item to remain functional for a given pe-

riod of time. Then, it is very important that a statement of reliability is always accompanied by the definition of the following concepts:

- *required function*, that specifies the item's task. For example, for given inputs, the item outputs have to be constrained within specified tolerance bands. The definition of the required function is the starting point for any reliability analysis, as it defines failures;

- *operating conditions*, which have an important influence upon reliability, and must be carefully specified;

- *mission duration T*, often taken as the parameter t, is defined as the time target up to which the object is supposed to work. Then the *reliability function* is defined by $R(t)$, and it is the probability that no failure will occur at item level in the time interval $[0, t]$, generally with the assumption that $R(0) = 1$.

The required function and the operating conditions can also be time dependent. In these cases a mission profile has to be defined and all reliability statements will be related to it. A representative mission profile and the corresponding reliability targets should be given in the item specifications.

Now let's define the concept of *failure* in a more thoroughly way. A failure occurs when an item stops performing its required function, and the failure-free operating time is generally a random variable; usually it is reasonably long, but sometimes very short, as failures may be caused by transient events at turn-on. Generally, when investigating the reliability of a device, it is assumed that at $t = 0$ it is free of defects and systematic failures (even if this is not always true). Failures are classified, besides their relative frequency, also according to:

- *Mode*: it is the symptom by which a failure is observed, for example drifts, open and short circuits for electronic components, and rupture, creep, cracking or fatigue for mechanical ones.

- *Cause*: it can be *intrinsic* or *extrinsic*. The first one is due to weaknesses or wearout within the item, while the second one is due to misuse or mishandling during the design, production, or operation phase. Extrinsic causes often lead to systematic failures, which are deterministic and should be therefore considered like defects, always present at $t = 0$.

- *Effect*: it includes the consequences due to the failure of an item, and it can be different if considered on the item itself or at a higher level. A usual classification is: non-relevant, partial, complete and critical failure. They can also be distinguished between *primary* and *secondary*, as one failure can cause further damages in the item, generating more failures.

- *Mechanism*: it is the process resulting in a failure (physical, chemical, mechanical, etc...).

A further distinction can be done between *sudden* and *gradual* failures, with the firsts termed *"catastrophic failures"*, and the seconds *"degradation failures"*.
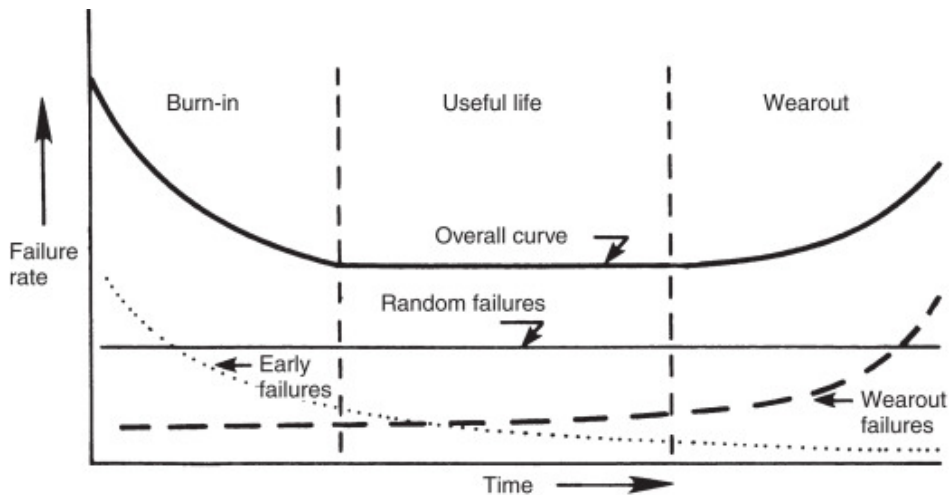
Figure 4.2: In picture is reported the so called Bathtub curve. The overall curve (continuous thick line) is presented with also the individual contributes of each different life phase, in particular early failures (dotted line), wearout failures (dashed lines) and random failures (continuous narrow line). Adapted from [19]

For a product life, an important role is played by *failure rate*, also known as *hazard rate*, $h(t)$. Generally the failure rate of a large population of statistically identical, independent items exhibits the following three phases, often showing the form of a bathtub curve, as reported in Fig. 4.2:

1. *Early failures* or *infant mortality*: failure rate decreases rapidly with time. In this first phase, failures are generally attributable to randomly distributed weaknesses in materials, components, or production processes, and so they are considered as intrinsic failures.

2. *Failures with constant failure rate* or *useful life*: failure rate is approximately constant and equal to h; failures in this phase follow a Poisson distribution, and usually are sudden and complete, so they are extrinsic (due to external accidents).

3. *Wearout failures*: failure rate increases with time, and failures are generally related to aging, wearout, fatigue, and so on, thus they are considered as intrinsic failures too.

An ideal situation is to eliminate the failures caused by defects in the infant mortality portion of the curve through burn-in or environmental stress screening (ESS), and to limit the operation period of the item so that it doesn't falls into the wearout phase. Indeed, the operational life of a product is usually kept within the typically constant failure rate section of the curve.

4.1.2 Mathematical Approach

In the following, the general basic mathematical statistics used in reliability will be analyzed as reported also in chapter A, according to [19–21].

Let's assume that n statistically identical, independent items are put into operation a time $t = 0$ under the same conditions, and that at time t a subset $\overline{n}(t)$ of these items have not yet failed. $\overline{n}(t)$ are independent realizations of a random variable, designated as the item's failure-free operating time, τ.

First of all some *empirical* quantities, i.e. statistical estimates of the real ones, can be defined. These are important because in practice there are never unlimited samples to test, and so n never tends to ∞, which is the condition for which the estimates converge to the real value. Thus, even if the outcome won't be the real one, this is the only way to achieve some results and do some calculations.

The *empirical mean of τ*, or the *empirical mean time to failure (MTTF)* is obtained through the following expression, and converge to the real value $\bar{t}$ for $n \rightarrow \infty$:

$$\hat{\bar{t}} = \frac{t_1 + \cdots + t_n}{n} \tag{4.1}$$

The *empirical reliability function* is given by the following relation, and it converges to the real value $R(t)$ for $n \rightarrow \infty$:

$$\hat{R}(t) = \frac{\overline{n}(t)}{n} \tag{4.2}$$

The *empirical failure rate* is defined as:

$$\hat{h}(t) = \frac{\overline{n}(t) - \overline{n}(t + dt)}{\overline{n}(t)dt} \tag{4.3}$$

where $\hat{h}(t)dt$ is the ratio of the items failed within the interval $(t, t + dt]$ to the number of items still functional at the time t. This estimate converges to the real value for $n \rightarrow \infty$ and $dt \rightarrow 0$, in such a way that $ndt \rightarrow 0$.

Let's now pass to the definition of the real quantities, and to how they are related to each other.

Reliability is the probability of an item to perform properly under typical operating conditions for the expected lifetime, and it can be defined mathematically as:

$$R(t) = 1 - F(t) \tag{4.4}$$

where $R(t)$ is the reliability function, defined as the probability of operating without failure until time t, and $F(t)$ is the *cumulative failure distribution function* (CDF), that is the probability that a randomly chosen part will fail by time t. A lifetime distribution model is $f(t)$, the *probability density function* (PDF) over the time range $(0, \infty)$. The relationships between CDF and PDF are the following:

$$F(t) = \int_0^t f(t')dt' \tag{4.5}$$

$$f(t) = \frac{d}{dt}F(t) \tag{4.6}$$

The hazard or failure rate $h(t)$ is the probability that, as device reached time t without breaking, failure will occur in the next time interval divided by the reliability $R(t)$:

$$h(t) = \frac{f(t)}{1 - F(t)} = \frac{f(t)}{R(t)} \tag{4.7}$$

Considering eqs. (4.4) and (4.6), this can also be rewritten as:

$$h(t) = -\frac{1}{R(t)}\frac{dR(t)}{dt} = -\frac{d}{dt}(\ln R(t)) \tag{4.8}$$

The integral of the hazard rate is the cumulative hazard or failure rate:

$$H(t) = \int_0^t h(t')dt = -\ln R(t) \tag{4.9}$$

The dimension of $h(t)$ is (time^{-1}). Since $R(0) = 1$, the reliability rate over a time period t is the exponential of the cumulative hazard rate in the same period t:

$$R(t) = \exp\left(-\int_0^t h(t')dt\right) \tag{4.10}$$

In many practical applications, the failure rate can be assumed to be nearly constant for all $t \geq 0$ ($h(t) = h$). Thus, from eq. (4.8) follows:

$$R(t) = \exp\left(-ht\right) \tag{4.11}$$

An important quantitative reliability concept is how long the population will survive without a failure. This is also termed *mean time to failure* (MTTF), more specifically, the mean time to the first failure. The mean of a continuous random variable (t) with density $f(t)$ (PDF), provided the integral converges absolutely, is given by:

$$\bar{t} \equiv \int_{-\infty}^{\infty} tf(t)dt \tag{4.12}$$

For positive continuous random variables, eq. (4.12) reduces to:

$$\bar{t} \equiv \int_0^{\infty} tf(t)dt \tag{4.13}$$

For $\bar{t} \leq \infty$, eq. (4.13) can be expressed as:

$$\bar{t} \equiv \int_0^{\infty} (1 - F(t))dt = \int_0^{\infty} R(t)dt \tag{4.14}$$

The eq. (4.14) is demonstrated in section A.1.1.
In many practical applications, the failure rate can be assumed to be nearly constant for all $t \geq 0$ ($h(t) = h$). In this cases it is common to define the *mean time between failures* (MTBF), which, putting eq. (4.11) inside eq. (4.14) becomes:

$$MTBF = \frac{1}{h} \tag{4.15}$$

4.1.3 Standards for Reliability (JEDEC)

To verify the reliability of a product, tests are chosen in order to prove its resistance to stressful conditions. Obviously these stress factors depend on the device and its application, as for example it is clearly useless to subject a sensor to temperatures of 300°C, when it will have to work around 60°C.
It is therefore important to understand that each device needs a test matrix that is meaningful for it. Furthermore, the same identical device designed for two completely different applications will have to be subjected to different types of tests to verify its reliability. Indeed, the same MEMS could be useful both for high temperature applications, or for others at high mechanical stresses. Thus, it is necessary to verify the thermal resistance in one case, and the mechanical robustness in the other (or both if the application is both at high temperatures and high accelerations).
In any case, for each qualification campaign, the test matrix is designed starting from past experiences on similar devices, but above all by referring to international standards recognized all over the world.

In the field of microelectronics, the most widely used standards come from JEDEC [22]. The JEDEC Solid State Technology Association is an independent semiconductor engineering trade organization and standardization body. Its origins date back to 1944, when the Radio Manufacturers Association and the National Electronic Manufacturers Association established the Joint Electron Tube Engineering Council (JETEC). Over the years it evolved, and in 1958 it was renamed JEDEC (Joint Electron Device Engineering Council). Over the next 50 years, JEDEC's work expanded into developing test methods and product standards that became vital to the development of the semiconductor industry.

Reliability testing at accelerated conditions is critical in generating lifetime data in a much shorter period of time. Stresses (e.g. high temperature, temperature cycling, applied voltage, relative humidity, etc …) experienced in the environment of use are enhanced (by means of accelerating factors) to a level that allows an acceleration of time-to-failure (TTF) of a device by means of an individual failure mechanism. The aim is to recreate the same failure modes occurring during the real application of the device.

The starting point used by *STMicroelectronics* for qualifying all of its products are standards, among which JEDEC itself, where general reliability test matrix are included. In Tab. 4.1 are reported the failure mechanisms generally investigated through each individual reliability test and an example is shown in Tab. 4.2. Before some of these tests, a preconditioning[1] (PC) is applied, in order to simulate the assembly process done by the customer. PC also checks that the mounting stress does not affect the subsequent reliability performances.

---

[1]Following JEDEC J-STD-020 MSL=3, preconditioning includes 24h bake at 125°C, 192h of moisture at 30°C and 60%*RH* and 3 IR reflow according to a dedicated profile.

Table 4.1: In table are reported the failure mechanisms investigated through each individual reliability test. Adapted from [22]

Test name	Description	Potential Failure Modes
HAST	Unbiased highly accelerated stress test (P, T, humidity)	electrochemical corrosion
HTOL	High temperature operating life	Electro and thermo-migration in the interconnections, wires bonding degradation, vias and oxides degradation
HTS	High temperature storage	Oxidation, structural changes, softening, drying out, viscosity reduction, expansion, parameters drift, noise, insulating resistance, open and short circuits
PC (JL3)	Preconditioning	Thermal and mechanical failure during manufacturing simulation
THB	Temperature humidity bias	Corrosion, electrolysis, resistance value increase, wire breaks
TC	Thermal cycles	Metal displacement, dielectric cracking, molding compound delamination, wire bonding failure, die attach layer degradation
MS	Mechanical shock	Structural changes, fracture of fixings and housings, lost of connections, fatigue, contact problems
ESD	Electrostatic discharge	Dielectric breakdown, thermal fatigue
LU	Latch-up	Catastrophic electrical failure

Table 4.2: Example of a reliability test matrix. It includes test coming from standarda,as JEDEC and MIL-STD. Adapted from [22]

Test name	Description	PC before	Conditions - Method	Duration
HAST	Unbiased highly accelerated stress test	✓	$T = 130°C$, $RH = 85\%$, JESD22-A118	96h
HTOL	High temperature operating life	✓	$T = 125°C$, $V_{dd} = 3.6V$, with self-test actuation, JESD22-A108	1000h
HTS	High temperature storage		$T = 150°C$ JESD22-A103	1000h
PC (JL3)	Preconditioning		JEDEC J-STD-020 MSL = 3	
THB	Temperature humidity bias	✓	$T = 85°C$, $RH = 85\%$, $V_{dd}3.0V$	1000h
TC	Thermal cycles	✓	$T_{low} = -40°C$, $T_{high} = +125°C$, JESD22-A104	1000cy
MS-1	Mechanical shock		$a = 3000g$, 0.3ms, MIL-SDT-883	
MS-2	Mechanical shock		$a = 10000$, 0.2ms, MIL-SDT-883	
ESD HBM	Electrostatic discharge		HBM model, JEDEC/JESD22-A114E	
ESD MM	Electrostatic discharge		MM model, JEDEC/JESD22-A114E	
ESD CDM	Electrostatic discharge		CDM model, ANSI/ESD-STM-5.3.1.ESDA	
LU	Latch-up		$T = 85°C$, $i = 100mA$ EIA/JESD78	

4.2 Test Matrix and Instruments

In this section the test matrix used for Porcino reliability will be presented, along with the instrumentation and the techniques employed for each test and measurement.

As reported in section 4.1.3, it is important to adapt standards to the product and application under consideration. For this reason, tests reported below have been customized or added, in agreement with the client, in order to be significant for studying Porcino and its possible failure modes (see section 4.3). Test matrix, with expected failure mechanisms and testing conditions, is reported in Tab. 4.4 andTab. 4.5.

Tests are divided into these categories:

1. **Mechanical tests**: shocks and random or sweep vibration. These are also followed by a powered life test.

2. **Powered tests**: life test in dry and humid environment, DC test and power On-Off test.

3. **Unpowered tests**: low-temperature storage (LTS), temperature-humidity storage (THS), thermal cycles (TC), electrostatic discharge (ESD).

Each test includes multiple phases. First of all, samples to be tested are subjected to a calibration procedure that allows the device to be programmed to work under certain conditions (see also section 4.2.1). Furthermore, before starting any test, a visual inspection (VI) with an optical microscope and a measurement of the key parameters (reported in section 4.3) are carried out, in order to have reference quantities and images to compare with the following measurements. In this way it's possible to establish the state of progressive degradation of the device.

At this point the test can be started, whose total duration is different depending on the test itself. During their execution, tests are periodically stopped to allow the remeasure (*readouts, $t_1, \ldots, t_n$*) of the key parameters, and thus verify the state of the MEMS. A block diagram of this procedure is visible in Fig. 4.3.

Finally, two different kinds of TVs have been used:

- with magnets, for tests involving studies on fatigue phenomena. Indeed, in this way Lorentz force is generated and device is actuated;

- without magnets, for tests not involving micro-mirror oscillation (DC current and power On-Off). In this way current flows anyway in MEMS, creating dissipation phenomena that can be studied and correlated with some failure modes, avoiding cyclic fatigue contributions. Indeed, Lorentz force is not generated due to the lack of magnetic field, and MEMS doesn't cycle.

Some important key parameters that can be correlated with the failure mechanisms reported above have been found and monitored. These parameters are both mechanically and electrically related. They have been measured by means of two different automated stations: one for calibration and general measurements of

50
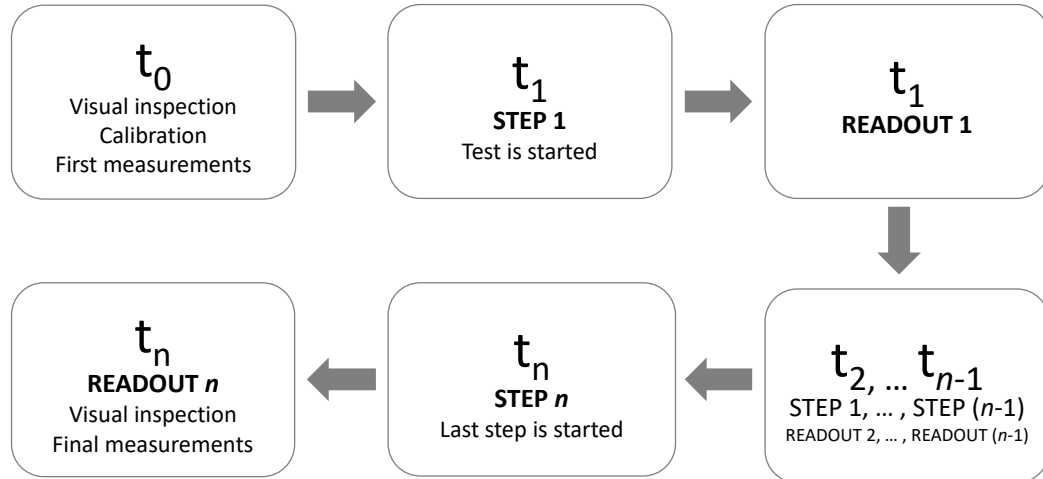
Figure 4.3: Block diagram of the flow used during Porcino reliability testing.

mechanical parameters, and one for electrical measures (resistances). They will be both described in section 4.2.

From calibration station the most important extracted parameters were the following:

- *Slow-axis angle* (deg)
- *Fast-axis angle* (deg)
- *Fast-axis sensor's sensitivity* $\left(\frac{mV}{V\,deg}\right)$
- *Slow-axis sensors sensitivity* $\left(\frac{mV}{V\,deg}\right)$

- *Fast-axis frequency* (Hz)
- *Slow-axis current RMS* (mA)
- *Fast-axis current RMS* (mA)
- *Full raster current RMS* (mA)

These parameters can be useful to identify some mechanical failures. One example is a loss in stiffness on the fast-axis due to oxide (stiffners) delamination, which correlates with a variation in fast-axis frequency.

Instead, from resistances station these measurements have been done:

- *Coil driving resistance*
- *SB1 resistance*
- *SO1 resistance*
- *SB2 resistance*

- *SO2 resistance*
- *FB resistance*
- *FO resistance*
- *Room temperature*

where *SB* stands for slow-axis sensor bias, *SO* for slow-axis sensor output, *FB* for fast-axis sensor bias and *FO* for fast-axis sensor output (outputs are referred to Wheatstone bridges of the sensors).

Also these parameters are very useful, as for example coil driving resistance can be used to better understand Cu oxidation and/or MEMS thermal behavior. It is also possible to find out if there are current leakages or open circuits when there are unusual values coming from the various channels.

For the most important quantities mentioned above, some limits on the drift they can show after testing have been imposed, and they are shown in Tab. 4.3. In this

Table 4.3: In table are reported the drift limits imposed, in agreement with the customer, after completion of each test.

Quantity	Drift (Δ)	Unit
Full-Raster Current	±5	%
Drive Resistance	+10	%
Fast-Axis Angle	±0.6	deg
Slow-Axis Angle	±0.6	deg
Fast-Axis Sensitivity	±4	%
Slow-Axis Sensitivity	±4	%
Fast-Axis Frequency	−100	Hz
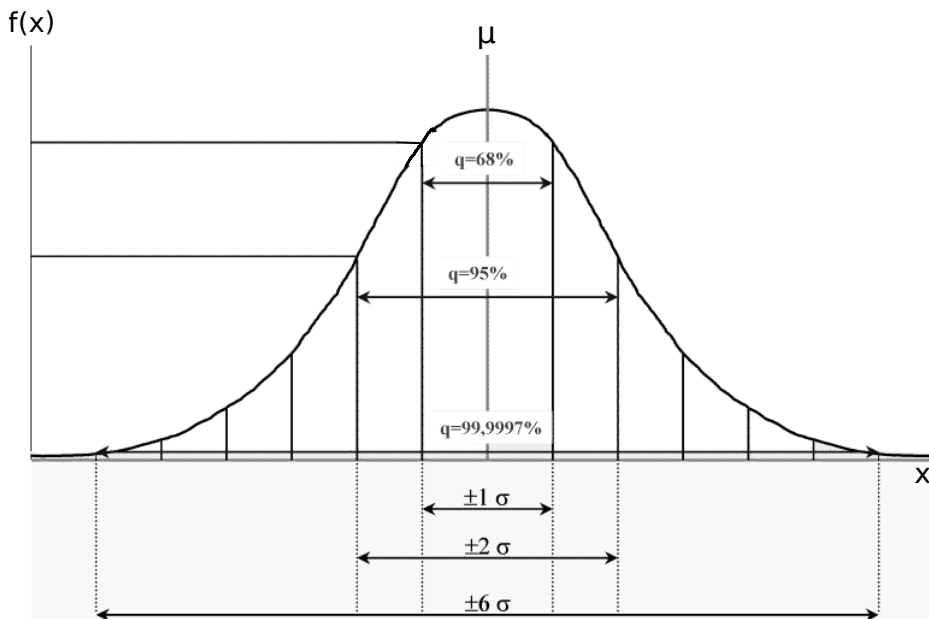
Figure 4.4: The graph shows how the limits for parameters drift have been chosen using the six-sigma approach. Adapted from [23]

way some criteria have been decided to establish whether tests have been passed or not, in agreement with the customer.

In particular, the thresholds of these parameters were evaluated taking into account the six-sigma value of their distributions. When the number of elements that compose a population is high enough, the statistics of this population can be approximated as a Gaussian (according to standards this condition is reached when at least 77 samples are available per lot). Using six-sigma means taking 99.99966% of the population into consideration, or, from another point of view, discarding 3.4ppm from it (see Fig. 4.4). Taking as an example the resonance frequency, its average value is approximately 21kHz and, tracing the limits according to the six-sigma approach (and thus excluding the 0.00034% of the population), it results that the acceptable threshold beyond which a device is considered anomalous is ±100Hz.

Table 4.4: In table is reported the reliability test matrix of Porcino. The expected failure modes searched for each test are presented in the last column.

Test name	Description	Expected Failure Modes
MS	Mechanical shock	Structural changes, fracture of fixings and housings, lost of connections, fatigue cracks, contact problems
VIB	Vibration test	Structural changes, fracture of fixings and housings, lost of connections, fatigue cracks, open and short circuits, contact problems
LT	Dynamic life test in dry environment	Fatigue cracks, oxides delamination, parameters drift
LT-RH	Dynamic life test in humid environment	Fatigue cracks, oxides delamination, parameters drift, insulation failure, short-circuiting
DC	Static DC current	Metals oxidation due to high power dissipation, vias degradation, electromigration, resistances drift
COR	Static power On-Off in humid environment	Sensor burns and vias degradation due to possible current peaks at powering on
LTS	Low temperature storage	Strength deterioration due to low-temperature fragility
THS	Temperature humidity storage	Electrochemical corrosion at package level
TC	Thermal cycles	Strength deterioration, thermal fatigue cracks
ESD-HBM	Electrostatic discharge - Human Body Model	Dielectric breakdown, thermal fatigue

Table 4.5: In table is reported the reliability test matrix of Porcino. The operating conditions of each test are shown, as well as its duration and readouts scheduled.

Test name	Description	Conditions	Duration	Readouts
MS-1	Mechanical shock	$a = 1500g$, 0.5ms		After test
MS-2	Mechanical shock	$a = 1000g$, 0.7ms	1000h	After test
Ran-Vib	Vibration Random	$a = 3.13g(RMS)$; f from 5Hz@$0.01g^2$/Hz to 20Hz@$0.02g^2$/Hz (slope up) and from 20Hz to 500Hz@$0.01g^2$/Hz (flat)	10 min/$axis$ on X, Y, Z	After test
Sweep-Vib	Vibration sweep frequencies	$a = 20g$; f from 20Hz to 2000Hz to 20Hz	$4cy/axis$, 4 min/cy	After test
LT-AM	Life test after mechanical tests	$T = 85°C$, $12.5° \times 15.7°$, $14° \times 18°$	168h	168h
LT85	Dynamic life test in dry environment	$T = 85°C$, $12.5° \times 15.7°$, $14° \times 18°$	1000h	168, 500, 1000h
DC	Static DC current	$T = 85°C$, $i = 180, 200, 210, 220$mA	1000h	72, 168, 336, 500, 1000h
COR	Static power On-Off in humid environment	$T = 85°C$, $RH = 85\%$, $i = 180$mA, $ON/OFF = 30$ min/30 min	1000h	168, 1000h
LT-RH	Dynamic life test in humid environment	$T = 85°C$, $RH = 85\%$, $12.5° \times 15.7°$, $14° \times 18°$, $12.5°, 14°, 15°(only fast - axis)$	1000h	168, 336, 500, 1000h
LTS	Low temperature storage	$T = -40°C$	1000h	168, 1000h
THS	Temperature humidity storage	$T = 85°C$, $RH = 85\%$	500h	500h
TC	Thermal cycles	$T_{min} = -40°C$, $T_{max} = 85°C$	$1000cy$	$250, 1000cy$
ESD-HBM	Electrostatic discharge - Human Body Model	0.5, 1, 2kV		After test

4.2.1 Calibration and Readout Setup

Before subjecting TVs to various tests, a calibration procedure and the first measurements must be carried out.

Given the innovativeness of Porcino project, measurements and calibrations of devices could not be made on consolidated and automated machinery as nowadays in the case of more mature technologies, such as inertial sensors. Indeed the setups used have been designed specifically for the qualification of this product, and therefore result highly customized and less efficient in terms of automation and time to measure a sample with respect to other systems.
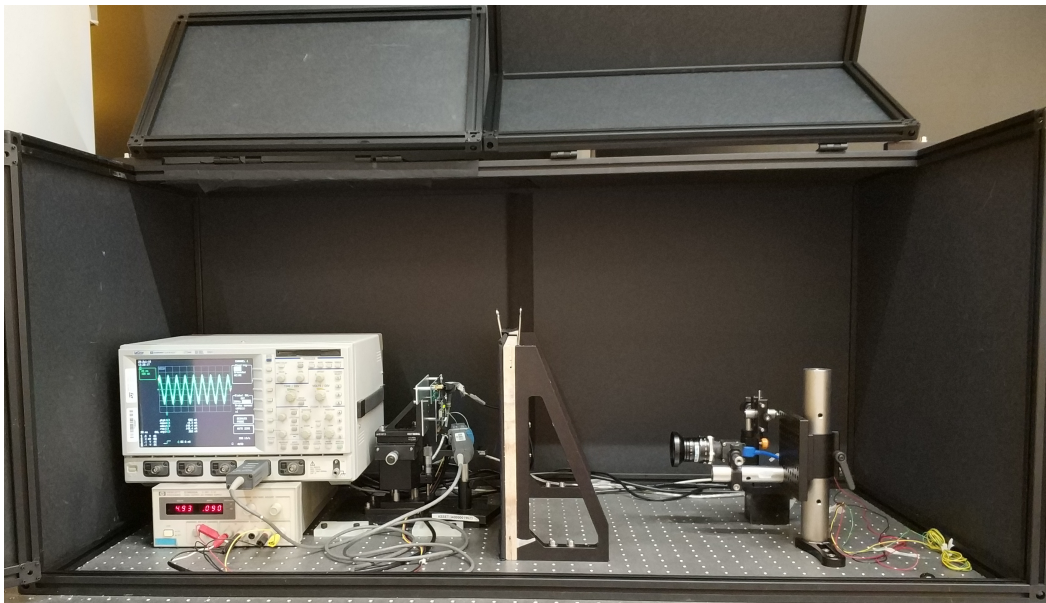
Figure 4.5: In figure is reported the setup used for calibrating Porcino devices and measuring their key parameters

Calibration has been done using a semi-automatic calibration station (shown in Fig. 4.5), whose set up and operation were provided by Characterization Team of *STMicroelectronics*. The setup consists of a generator (*HP E3620A*) necessary to send the driving signal to the daughterboard and then to the device, and an oscilloscope (*LeCroy WAVERUNNER LT344*) with a current probe to collect driving current signals, and eventually to analyze sensor signals. The half mechanical opening angles are measured using a red laser (*Laser diode, class II, λ = 650nm*) with normal incidence on the mirror surface: the projected line, or the full biaxial raster are collected by a camera (*NAVITAR*) and processed by a software for extracting the opening angles(see Fig. 4.6a). An indirect measure of the opening angles can also be done by means of the piezoresistive sensors. Indeed, when the mirror is in torsion, their resistivity value varies, and this can be related to a variation in the stress level in the area, which in turns corresponds to a certain angular opening of the mirror.

Calibration consists in programming the daugtherboard via GARNET, in order to supply the device with the right amount of current, so that the mirror reaches
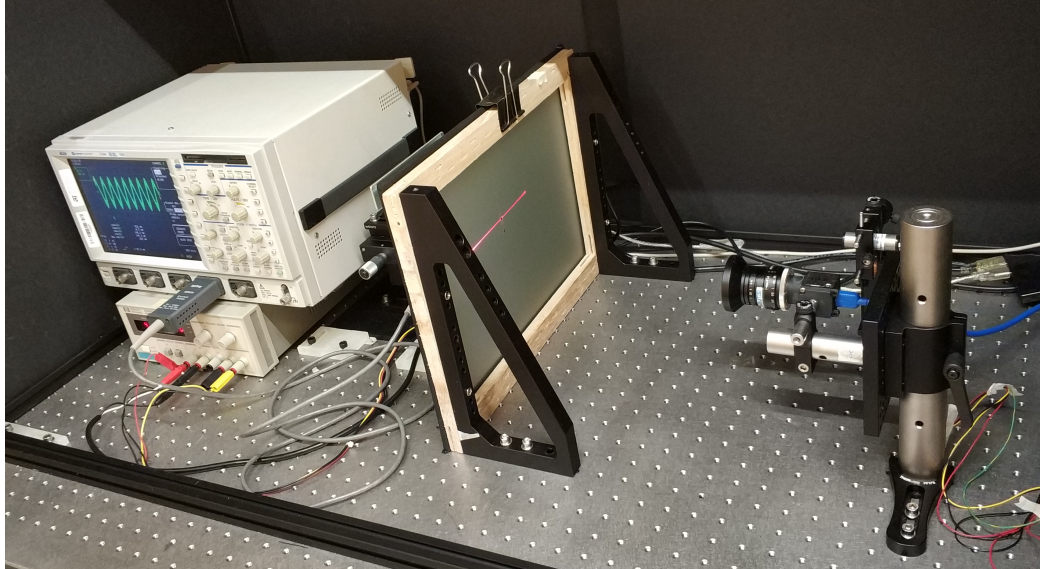
(a) Setup for optical acquisition of mechanical opening angles
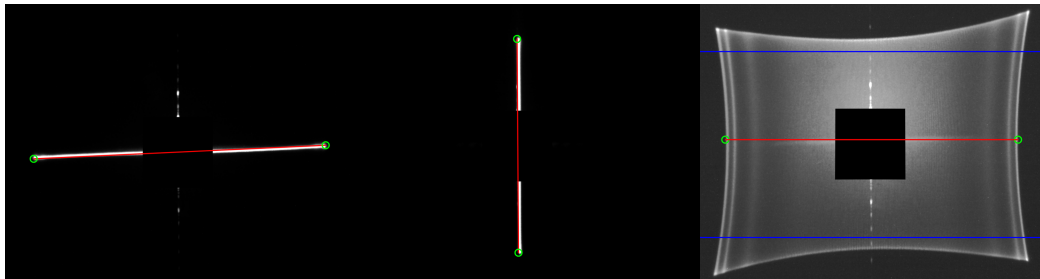
(b) Output results of the station. On the left side slow-axis, in the center fast-axis, and on the right side the full-raster projections.

Figure 4.6: In figure is reported the calibration station during angles measurement and its output results.

the desired opening angles (12.5°, 14°, and if needed 15° for the fast-axis, and 15.7° and 18° for the slow-axis). These current values are stored in the GARNET, so that each device has its own specific driving signal to reach the operating conditions. In this way, they will always be guided with the same signal, even after completing their tests, so any changes or degradation in their functional parameters can be discovered by comparison with data collected at t_0 (such as mirror's opening angles or resonance frequency of fast-axis spring). It is clear that, after this step, each TV must have a one-to-one correspondence with its daughterboard for the rest of its life.

Just after the calibration step, the first measurement of the parameters of interest is made. The values of these parameters are the reference points from which to start in order to perform an accurate data analysis. Obviously, there could be variations of values measured in different sessions due to intrinsic errors of measurement setups from time to time. To overcome this problem, each group of devices to be tested is accompanied by five reference TVs that are never subjected to stressful conditions, and which can therefore be used to align the measurements made in different sessions and thus to obtain consistent data.
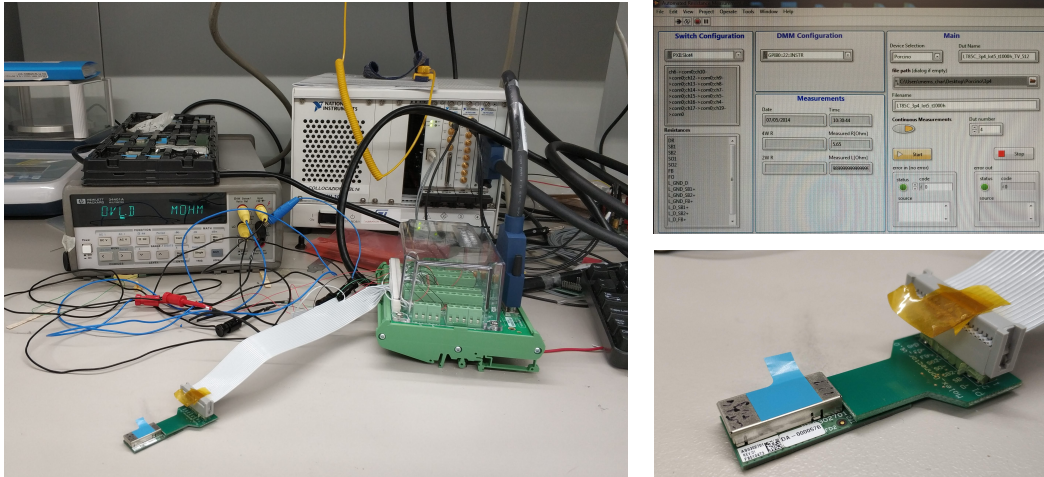
Figure 4.7: The picture on the left shows the set up used for resistance measurements. In top-right picture is reported a screenshot of the LabView tool used for this station. In bottom-right picture is reported a close-up of the connector used to connect TVs to the station.

Furthermore, several resistance values are also measured. In addition to the coil drive resistance, the BIAS and output resistances of the Wheatstone bridges of piezoresistive sensors are also measured, through which it is possible to establish if there are current leaks and open or short circuits in the MEMS. Also in this case some reference devices have been used to align the resistance values measured in different sessions. For these measurements another automated station prepared by Characterization Team has been used (Fig. 4.7), for which only the TV was needed, without the corresponding daughterboard. This setup consists in a multimeter (*HP 34401A*) and a PXI chassis (*NI PXI-1031*) that, connected to the device via a connector, are able to send a signal to each pad sequentially, thanks to a tool generated in LabView. The software is able to record the measured resistance values in an Excel spreadsheet, that can lately be used to analyze data.

All the key parameters mentioned in this section have been quantitatively collected at every scheduled readout, along with a visual inspection (VI). Furthermore, some photographs have been acquired, aimed at showing differences in samples conditions between t_0 and after the test.

4.2.2   Mechanical Tests

The task of mechanical tests is to verify the mechanical robustness of the MEMS by subjecting it to different types of conditions. Thanks to them it is possible to establish whether the device can withstand certain levels of acceleration or vibration.
This kind of tests can be performed both with static or actuated devices. These two approaches serve to better study certain types of failures. In case of Porcino, the MEMS weren't actuated. However, after these mechanical tests, the choice was to further stress the device with 168h of life test (carried out in a *MSL*

Technoven 300), in order to check whether any damage reported could affect the fatigue life of the device.

4.2.2.1 Shock Test

Shock test consists in providing the devices (suitably housed on steel plates made on purpose to be mounted on the machinery) a certain acceleration for a certain duration of time (pulse), along a specific axis.
The goal of this test on Porcino was to find out the maximum acceleration level that the MEMS structure could withstand. This means that, at the end of the test, there shouldn't be breakages in the MEMS structure and/or no functional parameters variations (Tab. 4.3), in particular loss of stiffness due to delamination or breakage of the oxide under fast-axis spring. In this case also chipping wasn't allowed, because, as already explained, it may create some chips on the die that could generate extra spots during mirror projection (due to incident laser reflection on the chips themselves).

This test has been performed on an *Avex SM-105-MP* shock machine, and two *Dytran 3200B5M* accelerometers have been used to measure the acceleration achieved and to assure planarity of the system, acquiring data by means of TP3 software. Following the specs reported in standard JEDEC[24], five shocks for each positive and negative direction ($\pm X$, $\pm Y$, $\pm Z$) have been performed, in two different stress conditions: the first with an acceleration of $1500g$ and a pulse duration of 0.5 ms (harder), and the second at $1000g$ and 0.7 ms (softer).

As reported in section 4.2.2, after mechanical shocks the devices have been subjected to a further 168h life test. Readouts were made immediately after the mechanical test and after the life tests 168h, with VI scheduled at each step of the test.
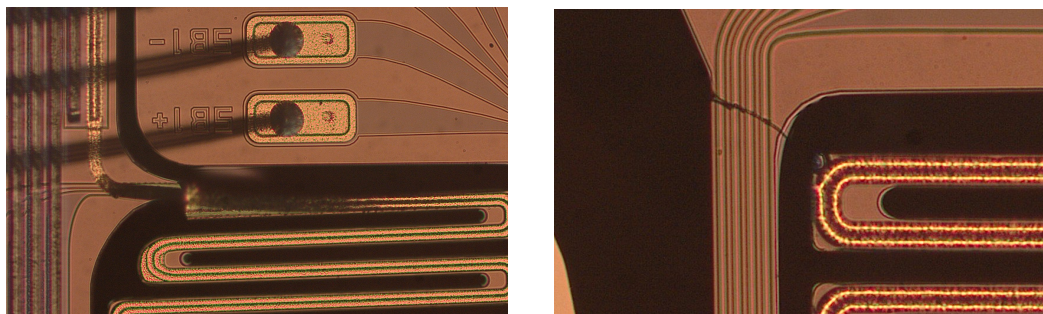
Figure 4.8: Two typical failure modes found out during mechanical shock test are reported in figure On the left, the breakage of the slow-axis spring anchorage is shown; on the right, the "bridge" of the frame is broken, probably due to a shock with the slow-axis folded spring (which is also chipped).

Tests at $1500g$ and 0.5ms have shown that this level of stress is too high for Porcino, which presented breakages on slow-axis springs and/or chipping on all the

tested samples. A typical failure mode of Porcino for this kind of test is shown in
Fig. 4.8.

Instead, shock tests performed at 1000g and 0.7ms haven't shown any issue of
this kind. Also angles, frequencies, resistances and sensitivity did not show sig-
nificant variations.

4.2.2.2 Random and Sweep Vibration Tests

These tests consist in subjecting TVs to vibrations along the three axes (X, Y, Z).
Their purpose is similar to that of shock test, but imposing different conditions to
devices, in particular low amplitude accelerations at high oscillating frequencies.
Also in this case, at the end of the test, there shouldn't be breakages in the MEMS
structure and/or no functional parameters drifts beyond the limits.
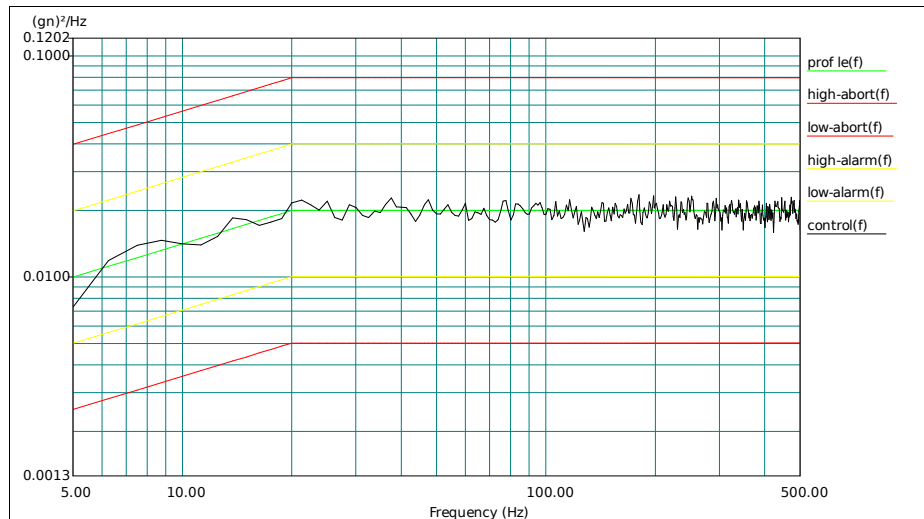
(a) Random vibrations operating conditions
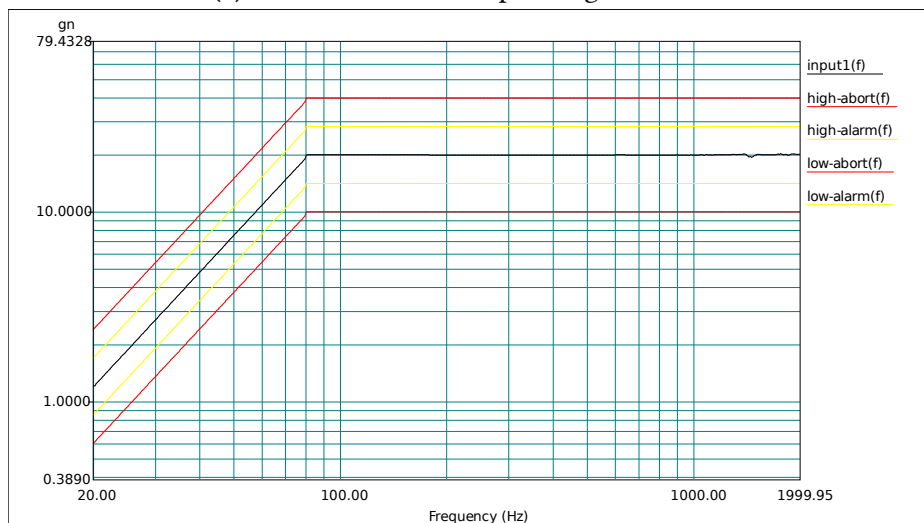
(b) Sweep vibrations operating conditions

Figure 4.9: In figure are reported two graphs showing the operating conditions used for vibration
tests (random and sweep vibrations). Adapted from [25]
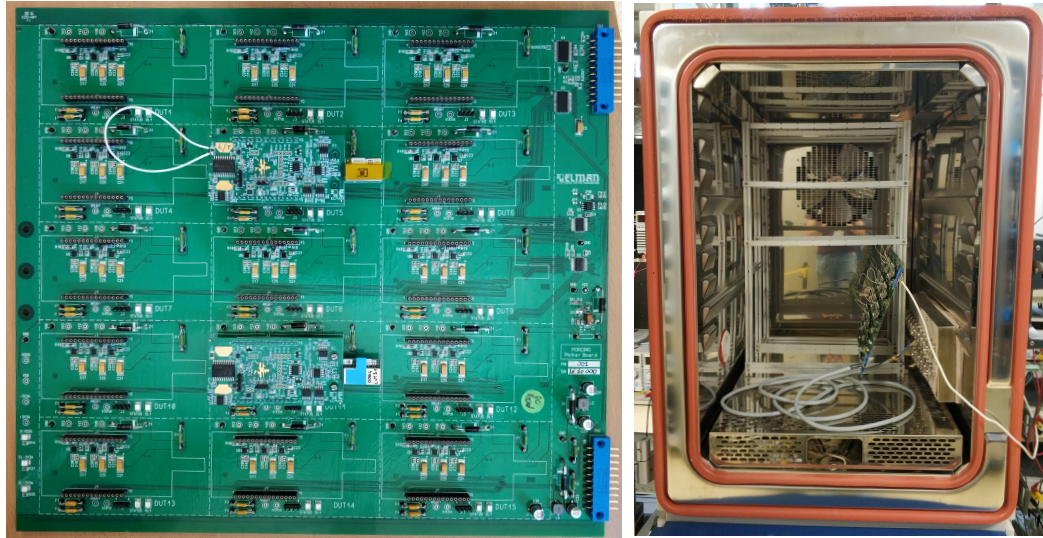
Figure 4.10: In figure it's shown a motherboard with two housed TVs. Its whole capacity is fifteen samples.

Vibration tests have been performed on an *Unholtz-Dickie* vibration machine, controlled by an LSD controller.

Random vibration test was inspired to the standard *MIL-STD-810E, Method 514*[25], but some modifications have been done, according to customer's needs. It consists in shaking the devices with an increasing acceleration of $3.13g$ RMS at various frequencies. It starts at 5Hz and $0.01g^2$/Hz and arrives at 20Hz and $0.02g^2$/Hz with a ramp, and then it goes from 20Hz to 500Hz at constant $0.02g^2$/Hz (see Fig. 4.9a). These conditions have been applied to all the axes for $10 \min/axis$.

Vibration sweep frequency test has been done following the standard *MIL-STD-883, Method 2007.3, Condition A*[24]. It consists in applying a vibration to the samples with an acceleration of $20g$, and with the frequency going from 20Hz to 2000Hz and then back to 20Hz (see Fig. 4.9b). Every cycle lasted 4 min, and each device has been subjected to $4cy/axis$.

After vibration tests, TVs have been subjected to a further 168h life test. Readouts were made immediately after the mechanical test and after the 168h of life tests, with VI scheduled at each step.

These tests haven't shown particular problems. Indeed, there weren't neither relevant drifts in the key parameters (reported in Tab. 4.3) nor breakages and chipping.

4.2.3 Powered Tests

Powered tests have been all performed in *Elman*[26], an external supplier of *STMi-croelectronics*. These tests have in common the fact that a driving current always
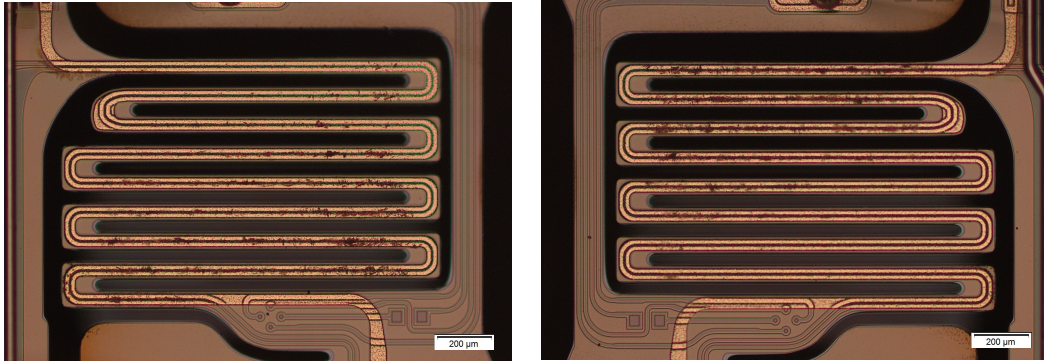
Figure 4.11: In figure is reported the skew-symmetric plastic deformation of gold on slow-axis springs. This is caused by the pitch spurious mode, which generate an asymmetric cyclic fatigue phenomenon.

flows inside the devices. Obviously testing conditions were all given by *ST*, and the key parameters have been internally collected at every readout. *Elman* supplied the ovens, the motherboards on which to house TVs (see Fig. 4.10), and the monitoring system used to carry out the tests described below. Three ovens were used throughout, two with only temperature control (*MSL Technoven 300* and *ACS Climatic System*), and one with both temperature and humidity control (*MSL Evolution Clima*). Each motherboard can accommodate 15 samples, and each oven can host 5 motherboards, resulting in a total capacity of 75 samples per oven at a time.

4.2.3.1 Life Test in Dry Environment

Life test is aimed at simulating the fatigue life of the device, in order to understand how much time the mirror can oscillate (and so how many cycles it can perform) without the object losing performances beyond certain limits (Tab. 4.3). In particular the major risk is the delamination of the reinforcing oxides, placed under the mirror and the anchorage points of fast-axis springs. This may cause a loss in stiffness that can translate into a variation in the resonance frequency of the device. Another failure mechanism could be the fast-axis spring breakage due to fatigue.
Life test has been performed in a *MSL Technoven 300* at 85°C in dry condition, and the micro-mirrors have been tested at two different opening angles ($14° \times 18°$ and $12.5° \times 15.7°$, where the first is the fast-axis angle and the second is the slow-axis one).

This test was designed for a duration of 1000h. Data and images have been collected at every readout, which have been scheduled at 168h, 500h and 1000h.

In these conditions frequencies and angles haven't shown any issue. For what concerns drive resistance, there is a gradual increase in its value, due to the progressive oxidation of the copper coil caused by the increase in power dissipation (increase in coil temperature). However no samples exited from the imposed limit

of 10% resistance drift.

Another remarkable result was the skew-symmetric plastic deformation of the gold covering the folded springs, reported in Fig. 4.11. This created a darkening of the interested areas, but hasn't affected the functionality of the device, without relevant changes in the key parameters (indeed, it was noticeable only by VI). The hypothesis is that partial oscillation of the frame along fast-axis (*pitch spurious mode*, see section 4.3) caused this phenomenon, generating an asymmetric alternation between compression and tensile stresses (fatigue).

4.2.3.2 DC Current

The task of DC current test (or simply DC test) is to verify how much current can pass inside the device without degrading it beyond the established limits (Tab. 4.3). Indeed, high current densities lead to great heat dissipation, which causes a considerable increase in the temperature of Cu-coil and surrounding areas (up to more than 250°C). Consequently the coil tends to oxidize at quite high rates, causing a progressive increase in its resistance [27]. Obviously this is bad, because the device needs increasingly higher current densities to keep the mechanical opening angle unchanged, and this cause an increase in temperature that augment Cu oxidation rate. Using a system driven in closed-loop (like that of *ST*'s customer) may create problems at system driving level, because the goal is to keep the operating angle fixed providing more and more driving current as the coil resistance increases (see section 3.2.

It's needed to point out that the MEMS does not fail in an absolute manner with a resistance increase, since in any case it remains functional for its application.

In any case, due to customer's method of driving (see chapter 3), it is still necessary to set a limit for the maximum increase in resistance of the coil, so that consumption remains contained and that the ultimate failure of the device (*thermal runaway*, see section 4.3) is not reached. This limit in resistance drift was set to $\Delta R_{coil} \leq +10\%$. Finally it is important to verify the integrity of piezoresistive sensors when subjected to these conditions.

For this test, TVs without magnets have been used, as actuation is not desired, in order to avoid any contribution of fatigue on failure and to stay in more severe conditions in terms of current densities.

However, although current flow was enough for studying Cu-coil resistance variation (Cu-oxidation), considering that mirror didn't oscillate, it was necessary to find a way to measure possible variations in sensors' sensitivity. This was feasible because piezoresistors are not only sensitive to changes in mechanical stress, but also to temperature variations in their surroundings. Indeed, as temperature changes, their resistivity modifies, and so does their output. In this way, by means of an accurate piezo-sensors calibration, it was possible to correlate the value they give as output to the temperature reached in their surroundings.

Calibration and measurement of sensitivity, and DC test itself have been performed in *Elman* with an *ACS Climatic System* oven.
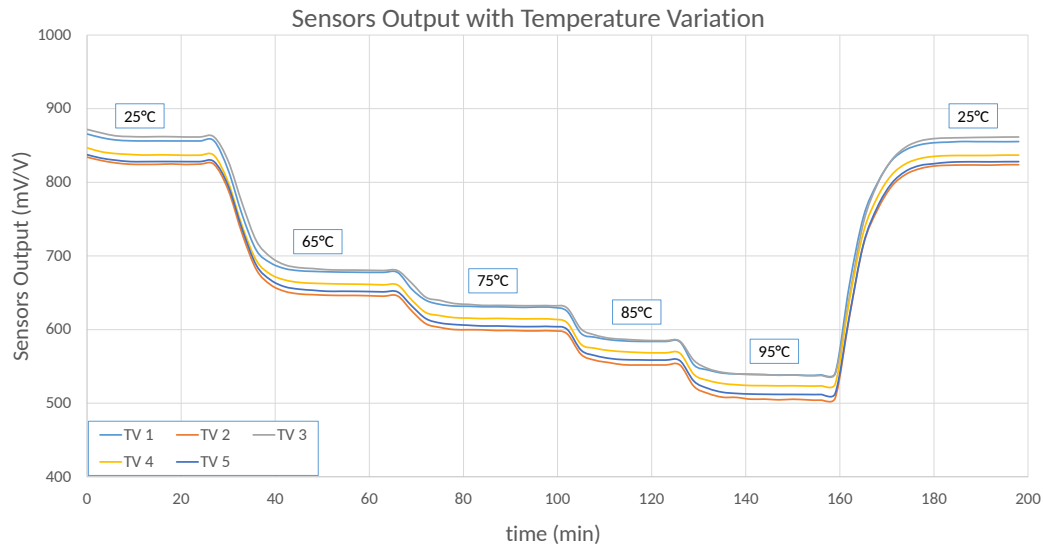
Figure 4.12: In figure is reported a graph showing sensors output with changing furnace temperature.

Piezoresistive sensors calibration procedure consisted in the following steps:

1. Motherboards with their TVs have been inserted in the oven, and the temperature has been progressively raised following precise steps. Temperature steps were chosen so as to cover the operating conditions of the device both during its actual application ($T \sim 60°C$) and during the accelerated test ($T \sim 85°C$). Starting from $T_{room} \sim 25°C$, the temperature steps were at 50°C, 65°C, 75°C, 85°C and 95°C, returning then to T_{room}. By using an external monitoring system, piezoresistive sensors' signals have been collected for every TV. At each stage it was necessary to wait the output signal to become stable and constant: this means that TVs have reached a thermal equilibrium with the ambient temperature of the furnace. (see Fig. 4.12)

2. Data about oven temperature and sensors output for each device under testing (DUT) were collected about every 3min by means of *Elman*'s monitoring system. In this way, a correlation between piezoresistive sensors' outputs and oven's temperatures (at thermal equilibrium) have been done, and it turned out that these two quantities are rather well correlated by a linear dependence (see Fig. 4.13). As already mentioned, to be as precise as possible, this correlation has been made for each individual device. Indeed, although the sensors are all similar, they always present different characteristics and output values.

3. At the end of the DC test, when the devices have reached a high level of thermal stress, the process is repeated again, to see if there have been significant variations with respect to the initial measurement of the sensors' outputs.

Through this procedure it is possible to verify the integrity of Porcino piezore-

63

SENSORS THERMAL BEHAVIOR
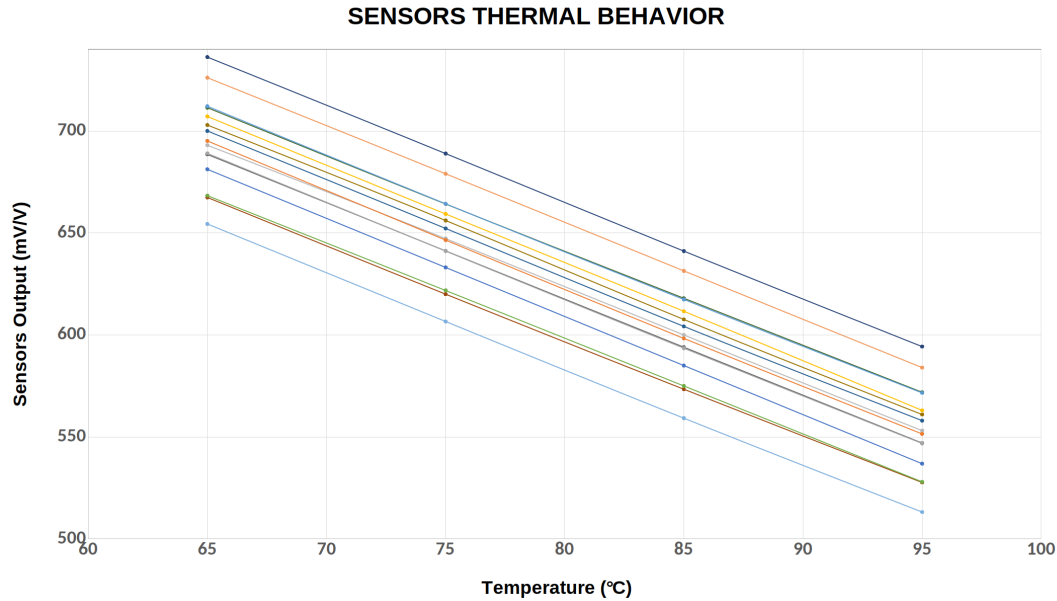
Figure 4.13: In figure is reported a graph showing the thermal behavior of Porcino's sensors. This is obtained processing data coming from sensitivity calibration procedure, carried out before DC test.

sistive sensors (Wheatstone bridge) by checking that their thermal response remains unchanged after a DC test at high current density. Additionally, it is always possible to know the temperature reached by the DUTs during operation and to understand if something is going wrong.

One thing to take into account is that only slow-axis sensors have been used for these measurements, as fast-axis one showed a non-linear trend at high temperatures, more difficult to describe. The problem is that the output of this sensor is more meaningful because it is placed right below the Cu-coil (the temperature of which is the most interesting), while the others are more distant. To overcome this problem and obtain the actual coil temperature, a physical model have been developed, which will be presented in section 5.1.2.

Passing to the actual DC test, it was conducted at an oven temperature of 85°C, in dry conditions, and MEMS were tested without actuation (no magnets) at different current levels (180mA, 200mA, 210mA and 220mA). It should be noted that these currents are all higher than the one reached during the application operating conditions (with 14°×18° opening mechanical angles), which settles at around 160mA.

The test was designed for a duration of 1000h. Data and images have been collected at every readout, scheduled at 72h, 168h, 336h, 500h and 1000h. In this case only resistances, current and sensors output have been considered, as other parameters required device actuation.

DC test results revealed some useful information. First of all, the device cannot withstand currents above 220mA, as the critical failure condition (*thermal runaway*) is reached (see Fig. 4.20). In particular, this is a problem, as the 250mA

64
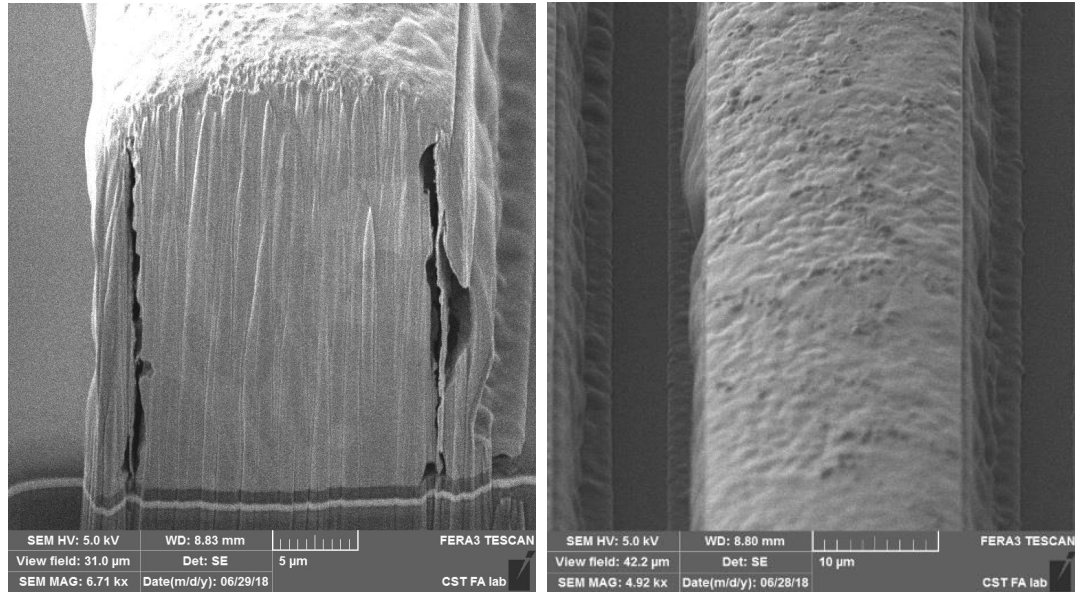
(a)
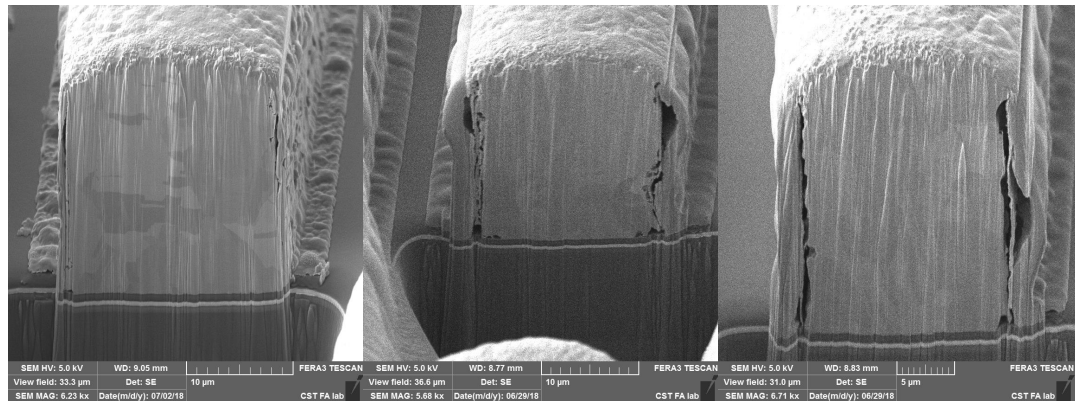
(b)

Figure 4.14: In Fig. 4.14a are reported some pictures of a Cu-coil after a DC test of 1000h at 210mA and 85°C. Pictures have been taken with a SEM microscope. In Fig. 4.14b are reported three pictures of coils subjected to different DC test conditions for a duration of 1000h. In order, from left to right: a coil with 180mA driving current, one with 200mA and the last with 220mA.

specification wasn't respected and it was necessary to lower it by customer side. Furthermore, the condition $\Delta R_{coil} \leq 10\%$ wasn't achieved, for some versions of Porcino (3.1 and 3.2), which exceeded this limit even with a current of 200mA. This means that progressive oxidation of the copper coil is significant, and this was confirmed by VI during readouts and failure analyses (see Fig. 4.14a). A comparison between coil oxidation with different driving currents is also reported in Fig. 4.14b. A trial to overcome and investigate this problem was to increase the thickness of the coil from 22μm to 27μm (versions 3.4 and later), so that it could withstand higher current densities.

A level of 220mA remains however too high, as ΔR_{coil} exceeds the limit of 10% in a fairly short time, but for lower current values the improvement is substantial, and even if some device does not comply with this condition, they still remain

marginal.

Since these problems are relevant for Porcino and its application, both a physical model, to describe the oxidation phenomenon, and a statistical one, to allow an extrapolation of the device life under different conditions, have been developed. These models will be presented and explained extensively in section 5.1.

4.2.3.3 Power On-Off in Humid Environment (COR)

Power On-Off in a wet environment (*COR*) is a test aimed at studying the behavior of the device when it is switched on, and in particular at verifying that there are no problems with the instant BIAS applied in presence of humidity (metal corrosion, burned points, etc...). Furthermore, during power-up there may be current peaks that can lead to malfunctions and to deterioration of delicate parts such as sensors. The fact that this test is effectively powered for just half of the total testing time means that the effects at 1000h should be equivalent to those at 500h of DC test, except for possible effects introduced by humidity. Furthermore, Power On-Off results can also be compared with THS ones (see section 4.2.4.2), that has the same testing conditions except for the flowing current. So, this test makes it possible to compare corrosion in a dry (DC test) or humid environment, and with powered or unpowered devices, without wasting time in setting up redundant tests.

Also for Power On-Off, TVs without magnets have been used, in this case to avoid possible failures due to fatigue in humid environment (see section 4.2.3.4). This test has been performed in *Elman* with a *MSL Evolution Clima* at 85°C and 85%*RH* (relative humidity), with a current of 180mA. Peculiarity of the test is that TVs receive current for 30 min (On condition) and then they remain unpowered for another 30 min (Off condition). These conditions have been chosen to let the device cool down during the 30min Off-state, allowing humidity to better collect on the surfaces, and thus to enhance its effect.

Power On-Off test in humid environment was designed for a duration of 1000h. Data and images have been collected at every readout, which have been scheduled at 168h and 1000h. As in the case of DC test, only resistances, current and sensors output have been considered, as other parameters required device actuation.

Results haven't shown any particular problem, as coil resistance drift is well below the 10% threshold (comparable with the resistance drift at 500h of DC test at 180mA). No relevant corrosive phenomena have been pointed out, in particular if compared with DC and THS tests, and also current peaks due to powering-on weren't a problem.

4.2.3.4   Life Test in Humid Environment

Life test in humid environment has the same goal of the dry one, but it's used to investigate the effect of relative humidity when the device is subjected to cyclic fatigue. The effects of humidity on silicon (both mono and poly-crystalline) have been extensively studied starting from the nineties [28–38, 54–58]. This test has been set up to verify if also Porcino was affected by these problems and to eventually study its failure rate.

This test has been performed in a *MSL Evolution Clima* at 85°C and 85%RH (relative humidity). Since the heat dissipated by current flowing in the coil tends to lower the relative humidity around the mirror, it was decided to carry out the test under the following conditions:

- bi-axial actuation at operating mechanical angles (14°×18° and 12.5°×15.7°);

- only fast-axis actuation at 12.5°;

- only fast-axis actuation at 14°;

- only fast-axis actuation at 15°.

The fact is that slow-axis actuation requires much more driving current than fast-axis one. Actually, from current measurements at calibration station it can be noted that, e.g. for mechanical angles of $14° \times 18°$, the full-raster RMS current is ~ 180mA, the one of only slow-axis ~ 170mA and that of fast-axis only ~ 65mA (**N.B.** Full-raster current is not the sum of the other two). Therefore, actuating TVs only on the fast-axis allows to dissipate much less heat and thus to have a relative humidity level very close to that of the oven itself. However, the test was carried out also with a bi-axial actuation in order to verify this theory and to have a direct comparison with life test in dry conditions. Devices actuated at different fast-axis mechanical angles have been tested in order to obtain a trend that could justify a loss in performances or breakages with increasing levels of stress, which is typical of cyclic fatigue.

Life test in humid environment was designed for a duration of 1000h. Data and images have been collected at every readout, which have been scheduled at 168h, 336h, 500h and 1000h.

  Results obtained from the test showed that there are no problems for devices actuated on both axes, as no breakages have been recorded. Instead, results of those driven only on the fast-axis were problematic. Indeed, TVs at 15° all broke within 300h of testing and those at 14° within 1000h. Most of those at 12.5° survived until the end of the test, but anyway some of them broke, which is not encouraging considering that this testing condition presents a mechanical stress lower than the application one (14°). Failures were all of the same type, with the breakage at about half the height of the fast-axis spring. Some images of this peculiar failure mode are shown in Fig. 4.15a and Fig. 4.15b.
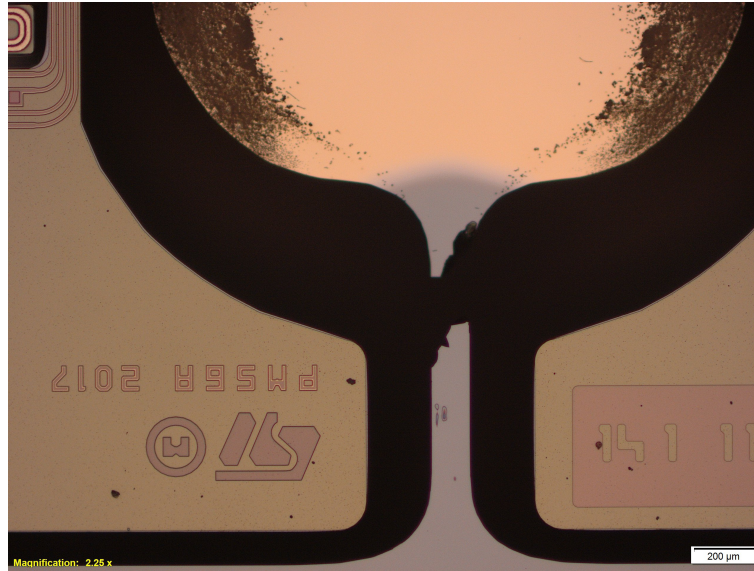
(a) Picture taken with an optical microscope during VI.
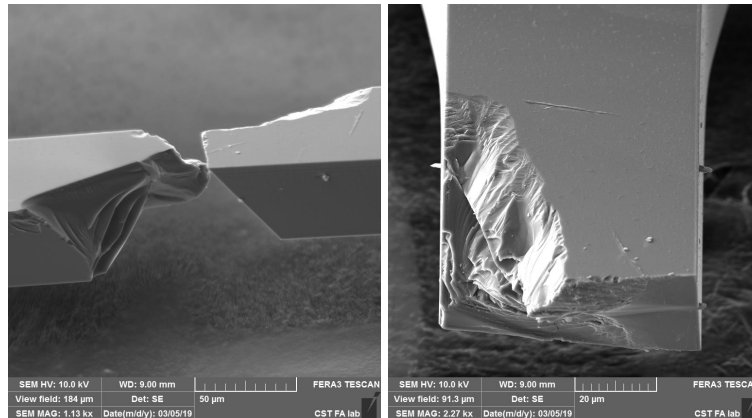
(b) Pictures taken with SEM during a failure analysis.

Figure 4.15: In figure are reported two pictures of the breakage on fast-axis spring occurred during a life test in humid environment.

Devices tested with bi-axial actuation showed results similar to those of life test in dry environment in terms of performances variations (key parameters drift). These observations have verified the theory for which the heat dissipated by the flowing current tends to lower the local relative humidity around the micromirror, turning the humid test into a one almost in dry conditions.

Considering these issues, further tests have been set up, as well as surface treatments on the device itself (in collaboration with *Politecnico di Milano*) to better study the phenomenon. With data obtained from these activities a model was developed to predict the life of the device in different conditions of cyclic mechanical stress and humidity. These activities activities, along with hypothesis and theories about this particular failure mechanism will be presented and explained in section 5.2.

4.2.4 Unpowered Tests

Unpowered tests have been performed internally at *STMicroelectronics*. They are designed in order to study the interaction between MEMS and its package in different environmental and stressing conditions. All these tests share the fact that no driving current flows inside the devices, so TVs are not actuated even if magnets are present. As explained in chapter 3, the package used by *ST* is not the same that will be used for application, but the client has assured that the two are completely equivalent and compatible, so the outcome of these tests remains valid.

4.2.4.1 Low-Temperature Storage (LTS)

LTS is aimed at verifying that the device, together with its package can withstand low temperatures [39]. Investigated induced failures include ice formation, structural changes, hardening and augmented brittleness. From an electrical point of view, there could be some parameters drifts.

The test was performed in a *Weiss WK340/40 Environmental Chamber* at $-40°C$ in dry environment, and TVs with magnets were used. In this way it is possible to verify if storage a low temperature may affect the MEMS mechanical response.

LTS was designed for a duration of 1000h. Data and images have been collected at every readout, which were scheduled at 168h and 1000h.

After testing in these conditions, there was no evidence of key parameters drift. Indeed, neither the mechanical performances nor the electric ones have been affected.

4.2.4.2 Temperature-Humidity Storage (THS)

The objective of THS is to ensure that the MEMS and its package are not subject to degradation or parameters drift in a hot and humid environment [40]. For Porcino, possible physical failures in these conditions could be related to corrosion and electrolysis, while electrical ones may include parameters drift, insulating resistances, leakage currents and shorts [19].

The test was performed in a *Weiss WK340/40 Environmental Chamber* at $85°C$ with $85\%RH$, and TVs with magnets were used.

THS was designed for a duration of 500h. Data and images have been collected only before and after the test, as a single readout at 500h was scheduled.

TVs tested in these conditions showed no problems whatsoever. The key parameters presented very low drift, and even from the corrosive point of view no issue were found.

4.2.4.3 Thermal Cycles (TC)

TC is a test designed to verify that mismatches between thermal expansion coefficients of the various materials which compose the device (MEMS + package) do not generate residual stresses and deformations that can be harmful for the operation of the system. Indeed, this could generate damages both on mechanical and electrical components, causing a loss of performances or even the failure of the device [41].

The test was performed in a *Weiss WK340/40 Environmental Chamber* in dry conditions, with temperature cycling between $-40°C$ and $85°C$ (see Fig. 4.16). TVs with magnets have been used.

TC was not designed on a time basis, but on the number of thermal cycles to be performed. In particular the test lasts $1000cy$, and data and images have been collected at each readout, scheduled at $250cy$ and $1000cy$.

In the end, test results were good. The drift of key parameters has remained abundantly within the set limits, and even optical inspection did not reveal deformations of any kind.
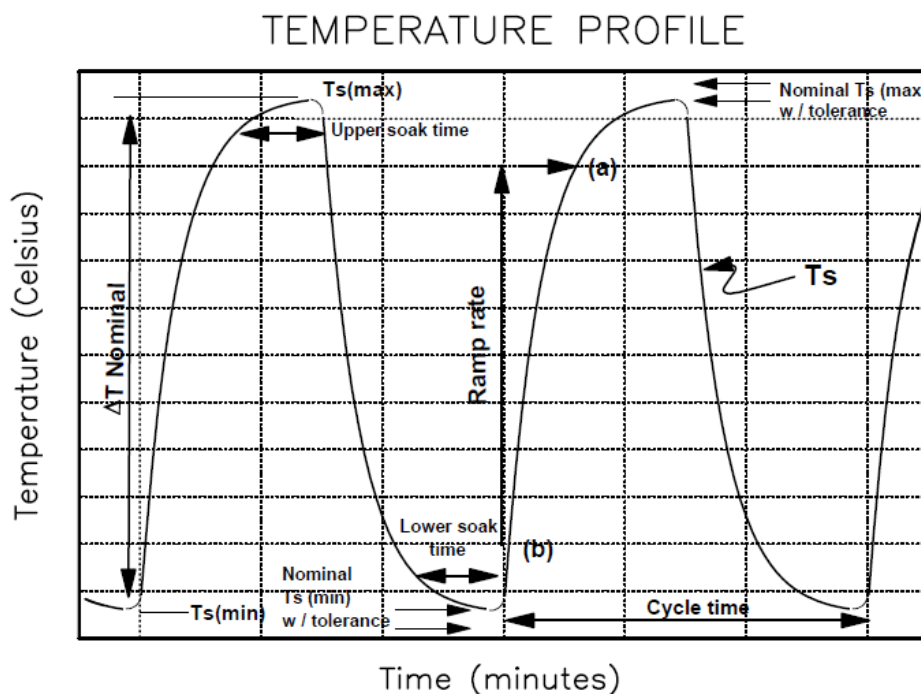
Figure 4.16: In figure is reported the temperature profile typical of thermal cycles test. Adapted from [41]

4.2.4.4 Electrostatic Discharge (ESD)

An electrostatic discharge (ESD) is a rapid discharge event that transfers a finite amount of charge between two bodies at different potentials (zap). Thus, a source of known and controlled ESD is needed to perform a test. ESD simulators should be able to reproduce the characteristics of the charge transfer processes which occur in the real world. Three different models have been developed: *human body model (HBM), machine model (MM)* and *charged device model (CDM)*. However only *HBM* has been used for testing Porcino.

HBM attempts to reproduce an ESD waveform generated by the discharge of a human being through a low impedance path. The rise time for the input signal to reach its maximum value is between 2ns and 10ns, while the decay time is within 130ns and 170ns (see Fig. 4.17). Specifications for this test are reported in standards *JEDEC*[42] and *MIL-STD-883 Method 3015*[24].
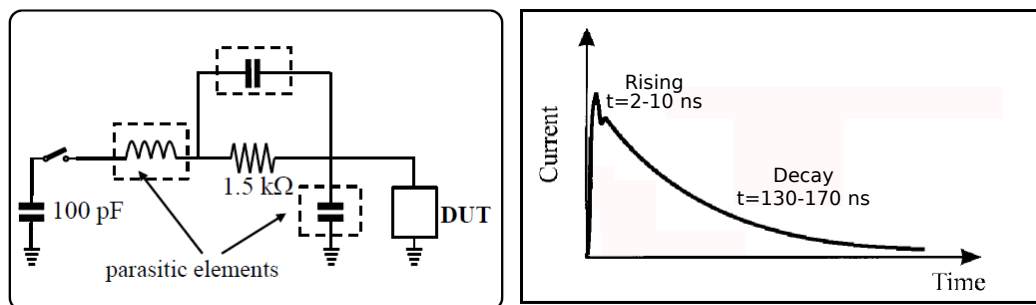
Figure 4.17: In figure is reported a schematic of an ESD test following the human body model (HBM). Adapted from [42].

The task of ESD test is to verify that there are no unwanted current paths inside the device and its package (current leakage), and that the system is able to withstand voltages of a certain level without creating problems, such as burns of sensors or other components.

The testing equipment used for ESD zapping was a *Hanwa W5100* with two pins. This is a cumulative stress test, in the sense that every single combination of pins on the device has been zapped, for each applied voltage level (500V, 1kV and 2kV).

ESD is an instant test, it does not include any kind of cycles, so data and images have been collected only before and after the test.

The results obtained weren't good. Porcino cannot sustain any of the three applied voltages, showing in most cases burns on the sensors or on the electrical paths (see Fig. 4.18).

To find out the maximum voltage level applicable to the system, a further test was set up. This consisted in applying to the same device higher and higher levels of voltage, to understand what its actual limit was. Two different conditions have been used:

- zapping from 350V up to 500V with steps of 50V;

- zapping from 400V up to 475V with steps of 25V .

Results are clear, the device is likely to withstand voltage levels $\leq$ 425V, as no failure have been registered below 450V. This means that the final system should not be subjected to voltages higher than this threshold, or that some modification should be done at package level in order to enhance device resistance to ESD. This last option must be a choice of the customer, since, being the owner of the package and the final device, he knows what the conditions of the application are, and therefore if these changes are actually necessary.
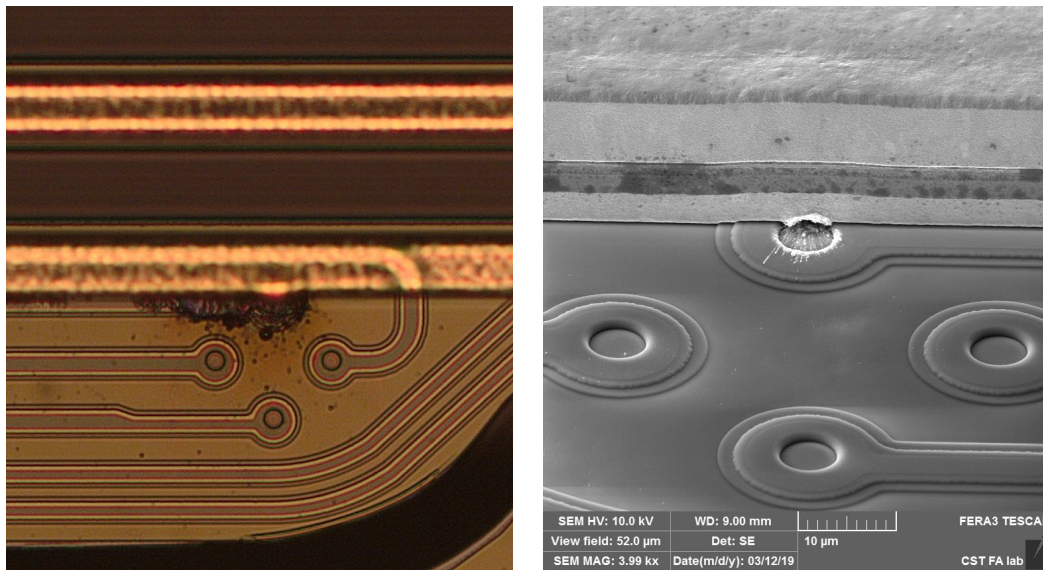
Figure 4.18: In figure are reported two pictures of a failure mode typical of ESD test (burnt sensor). Picture on the left has been taken by an optical microscope, the one on the right with a SEM.

4.3   Failure Modes

As reported above, each device has its own characteristic failure mechanisms, that can be different even depending on the application. Also Porcino presents some weaknesses, and thus certain possible failure modes were expected, and investigated during reliability tests by measuring the key parameters (see section 4.2). Below are the most critical points of Porcino, and the failure mechanisms encountered during reliability test (it's suggested to look at Fig. 4.19 to better understand the discussion):

- The coil that runs along the MEMS frame is made of copper (Cu), so it is subjected to oxidation (producing CuO), especially when it reaches high temperatures. This happens by raising the ambient temperature, or by increasing the current density that flows inside of it (increase in power dissipation, $P = Ri^2$). Cu oxidation progressively increases the electrical resistance of the coil, that, by cascade, increases power dissipation.
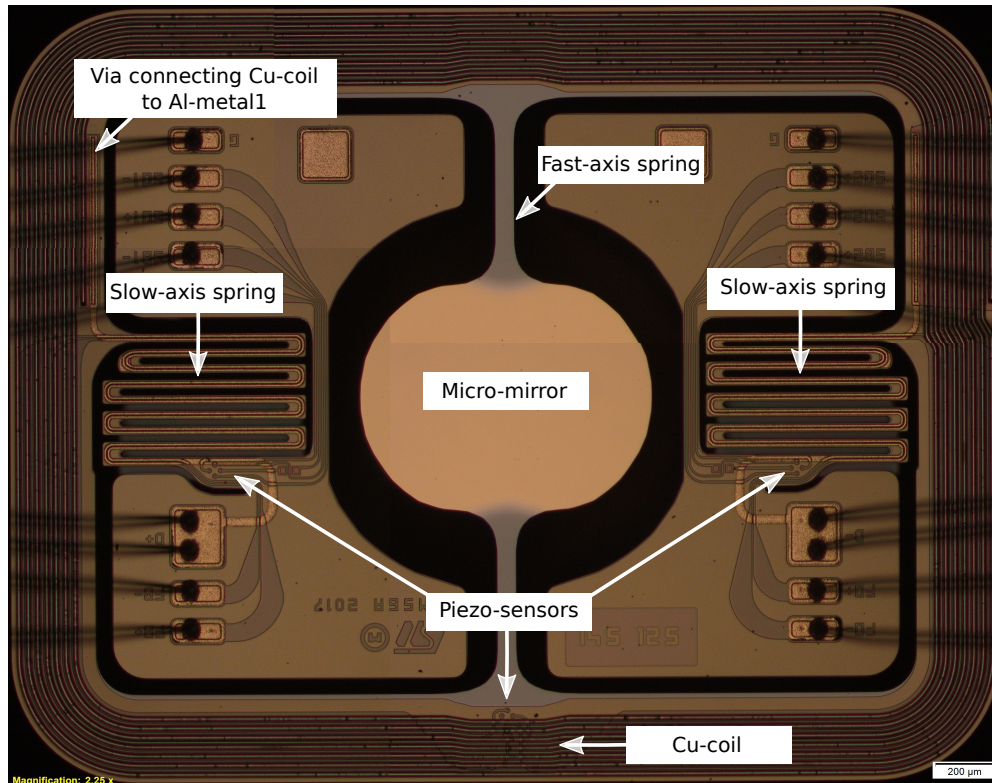
Figure 4.19: In picture is reported a top view of Porcino. All the main components are visible, except the reinforcing oxides under the mirror and at the fasteners of the fast-axis springs, and the four magnets on the sides.

If too high temperatures are reached, there is risk of incurring in the so-called "*thermal runaway*" (see Fig. 4.20), whose effect is the complete degradation of the contact surface between Cu-coil and Metal$_1$ or Cu-seed layer. This event causes the catastrophic failure of the device. In any case, under normal current conditions, the main effect would be only copper oxidation, that would not compromise functioning of Porcino (target opening angles). In principle, CuO formation is not a catastrophic failure mode, but, as customer drives the device with a closed-loop driving current, this could be a problem for the driving system. Thus, variation in coil resistance is taken into account by setting the maximum limit of $\Delta R = 10\%$.

- During a sharp acceleration or if subjected to vibrations, Porcino may have problems regarding its mechanical strength. Indeed, as explained in chapter 3 fast-axis spring is very rigid and therefore quite fragile. Regarding slow-axis folded springs, they risk a breakage at the attachment point with the frame.
  Another failure mode can occur when a folded spring hurts the frame bridges (frame sections on micro-mirror side, next to the slow-axis springs), creating chips that are harmful to the operation of the micro-mirror. Indeed they can generate some extra spots during mirror projection by incident laser reflection.

73
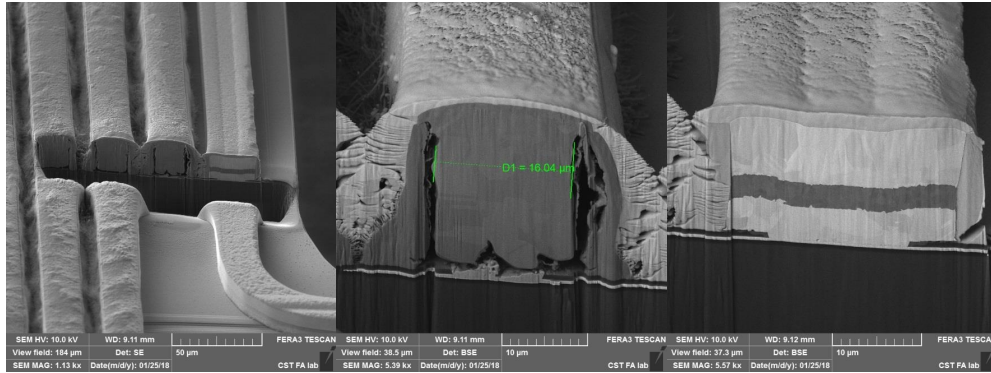
Figure 4.20: In figure are reported some pictures taken with a SEM. They show the complete degradation of the contact area between Cu-coil and Cu-seed layer.

A visual inspection (VI) with an optical microscope is done in order to verify these failures (if they are evident). To check also if micro-defects not visible at VI are present, a monitoring of mechanical angles amplitude and fast-axis spring frequency have been done.

- Piezoresistive sensors play a fundamental role in monitoring Porcino's functioning, and also in its driving. Thus, it is very important that these components don't undergo any kind of degradation, being it of mechanical or electrical nature (one of the biggest risks is to burn a sensor due to a high current peak). To assure the correct functioning of the sensors, their sensitivity[2] has been monitored.

- Mechanical stress and fatigue phenomena can cause delamination of oxides (stiffners) under fast-axis spring. This type of failure is studied by monitoring the resonance frequency of fast-axis spring that tends to decrease as oxides delaminate, because spring's stiffness progressively decreases. The decrease of mechanical opening angles is also a good indicator for this event.

- Cyclic fatigue, especially when associated with a humid environment, can cause the breakage of fast-axis spring. This is due to imperfections and micro-cracks present on the native oxide that covers the side-walls of the spring. Monitoring of this failure mode is not as simple as in other cases because silicon and its oxides are brittle materials, and so failure is sudden. In theory the progressive decrease in fast-axis frequency should be a good parameter for this, but a system able to perform a very dense monitoring (almost continuous) would be necessary in order to be able to read these variations before the breakup event. Unfortunately this wasn't possible during the tests, but through monitoring system it was still possible to obtain the failure time of each TV with an error of about 3min, extracting it by looking at PZR sensors output. Further studies have been done on the broken pieces through optical inspections and failure analysis.

---

[2]Sensitivity is measured as mV/deg V, and in practice is the output of the unbalanced Wheatstone bridge divided by the measured mechanical angle on the same axis.

Modeling of Main Failure Modes

According to results obtained from the test matrix discussed in chapter 4, some conditions have proved to be more aggressive and problematic for the device than others. To better study and describe these phenomena, models have been created, both of physical and statistical nature, trying to describe and study these phenomena. In particular, the two tests that showed failures were DC tests and life tests in humid environment, and both have been taken into consideration.

5.1 Copper Coil Oxidation

As already described in section 4.3 and section 4.2.3.2, a possible failure mode is the progressive oxidation of the Cu-coil caused by high temperatures, up to the point where coil's driving resistance augment beyond the limit set to $\Delta R = 10\%$ (or even worse, when thermal runaway occurs).
More in detail, DC test creates critical conditions for coil oxidation, as power dissipation is quite severe ($P = Ri^2$) due to high flowing currents ($180 - 220$mA), and coil temperature can reach even $T \sim 280°$C.

Since Cu oxidation process is thermally driven, first of all it is necessary to find a method to establish its temperature when a certain amount of current flows inside of it. To do this, before the beginning of this thesis work, Design Team of *ST* created a FEM thermal model based on Porcino 3.1. The model has been also validated with experimental measurement (see section 5.1.1).

5.1.1 Thermal Model Description and Validation

The FEM thermal model includes the following main elements, as shown in Fig. 5.1:

- the chassis, that is a thermally equivalent substrate (k_{th});

- the MEMS structure (Si);

- the driving current path, which consists in coil and slow-axis springs lines, respectively made of Cu and Au;

- the slow-axis (SA) and fast-axis (FA) PZR sensor probes;
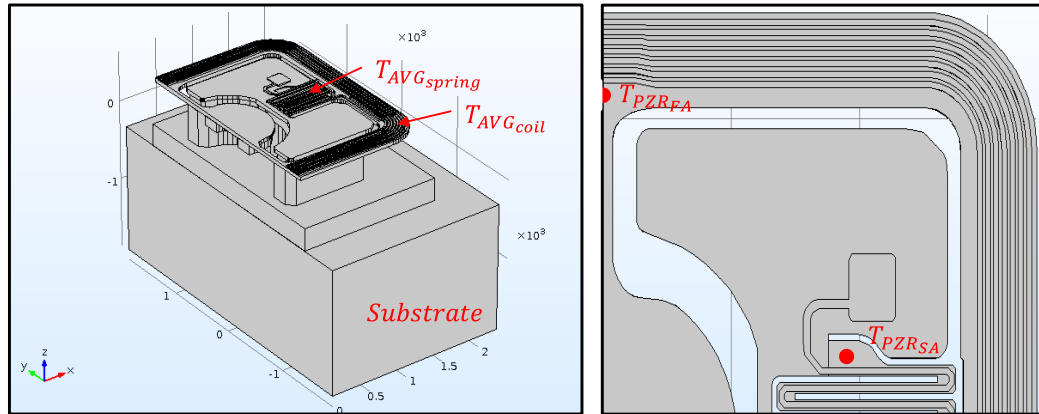
Figure 5.1: In figure are reported two images of the model used for the FEM thermal analysis.

- the surrounding air, set to T_{room} to simulate the conditions close to the device when placed on a hotplate at a certain temperature.

Results obtained through this FEM thermal model have been validated comparing them with experimental data collected under different testing conditions, covering a wide range of room temperatures and driving current for the MEMS.

The test matrix included data collection at T_{room} of 25°C, 45°C and 55°C (replicated by placing TVs on a hotplate), and driving currents of 100mA, 150mA, 180mA, 200mA and 220mA.

The output parameters were coil driving resistance R_{drive} (measured only at readouts) and slow-axis PZR sensors resistances R_{PZR-SA} (real-time monitoring through sensor output). It was chosen to take into consideration only R_{PZR-SA} (and not R_{PZR-FA}) because it presents a linear behavior with temperature even when a driving current flows inside the coil (being further away from the coil it doesn't overheats). On the contrary, the fast-axis PZR is situated right under the Cu-coil and reaches too high temperatures due to Joule effect when a driving current is present; as a result R_{PZR-FA} shows a non-linear behavior with temperature and cannot be used for the system monitoring.

In order to convert R_{PZR-SA} in terms of local temperature, a preliminary calibration of the SA sensors have been done, as shown in Fig. 5.2. In this way it is always possible to know the temperature in correspondence of the slow-axis PZR starting from the measured R_{PZR-SA}.

SA temperatures extracted by the FEM thermal model have been compared with data measured at each room temperature of the test matrix for devices under different current conditions ($100 - 220$mA). As a result, FEM model predicts quite well the thermal behavior, with an error that remains within 5% (e.g. see the case at $T_{room} = 55$°C in Fig. 5.3).

On the other hand, in order to calculate the coil temperature and evaluate the accuracy of results, an indirect method must be exploited. Indeed, the electrical resistance of the MEMS driving path is used as a comparative parameter, as it is directly related to coil and serpentine springs average temperature ($T_{avg-coil}$

76
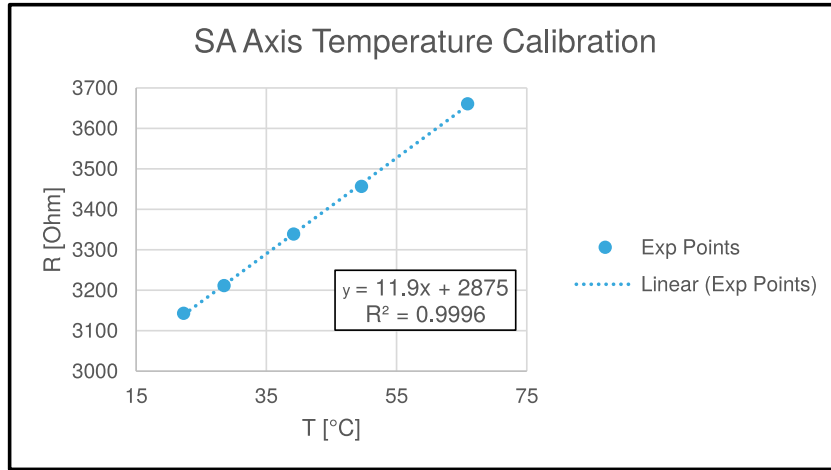
Figure 5.2: In figure is reported the relationship between SA PZR sensor resistance and ambient temperature. It is noticeable that in this range the behavior is linear.
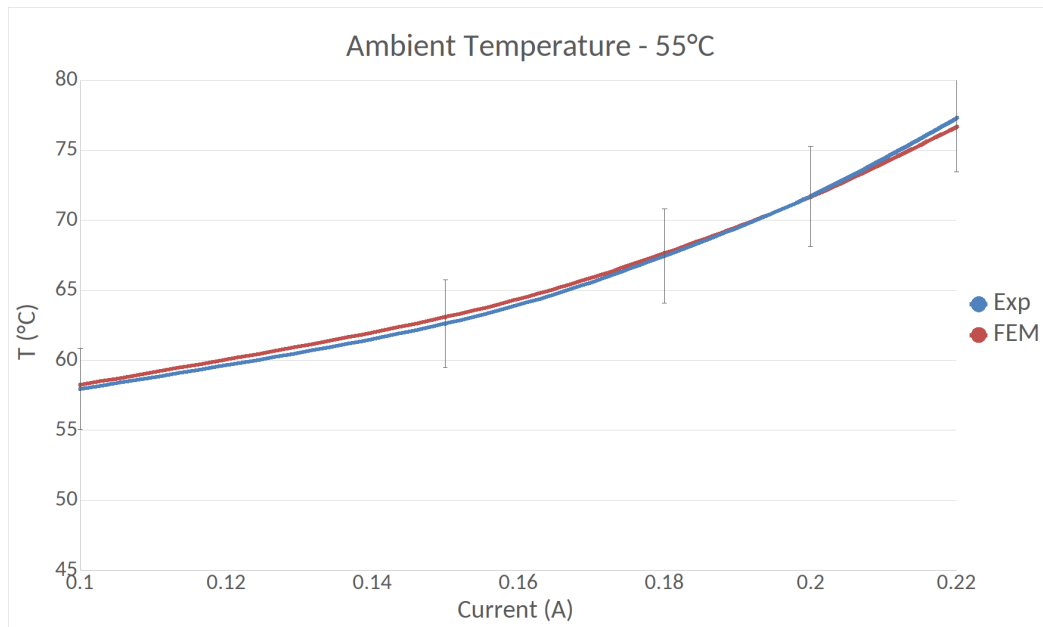
Figure 5.3: In figure is reported a graph with results of FEM thermal analysis. It is possible to see that they describe quite well the real thermal behavior of the system.

and $T_{avg-spring}$, which can be calculated in first approximation considering room temperature and the power dissipation caused by the driving current):

$$R_{MEMS} = R_{Cu_0}(1 + \rho_{Cu}(T_{avg-coil} - T_{ref})) + R_{Au_0}(1 + \rho_{Au}(T_{avg-springs} - T_{ref})) \quad (5.1)$$

where R_{Cu_0} and R_{Au_0} are the resistances of Cu and Au in standard conditions, ρ_{Cu} and ρ_{Au} the resistivities of Cu and Au and T_{ref} the reference temperature used for FEM modeling.

However, measurements are carried out not just on the MEMS alone, but on the whole TV, comprehensive of a series of elements such as driving paths, wires and resistances that give a non-negligible contribution to the resistance measurement itself. Thus, to compare FEM results with measurements done on TVs, a resistive
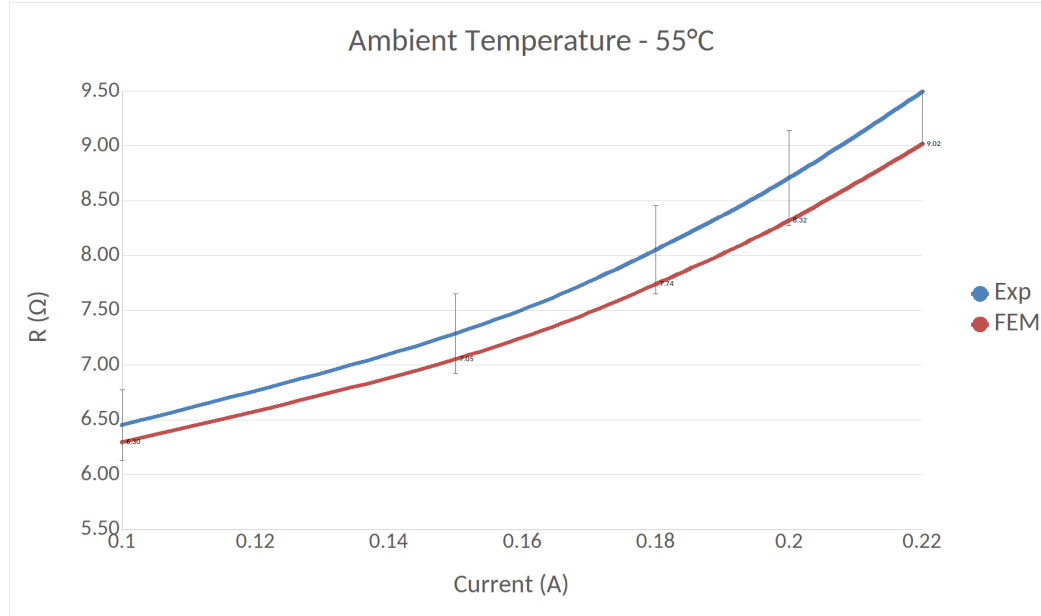
Figure 5.4: In figure is reported a graph showing thermal model validation results. FEM model seems to underestimate the drive resistance up to an error of 5% for the highest current levels. This error dependence on current may be explained by the introduction of the parasitic contributor, which could itself be subjected to variations with different driving currents.

parasitic contributor must be considered, which is described as a function of room temperature:

$$R_{TV} = R_{MEMS} + R_{par_0}(1 + \rho_{Cu}(T_{room} - T_{ref})) \tag{5.2}$$

where R_{par_0} is the resistance of the parasitic contributor in standard conditions and T_{room} the room temperature (hotplate temperature).

In any case, as visible in the example at $T_{room} = 55°C$ reported in Fig. 5.4, FEM model seems to underestimate the coil drive resistance up to an error of 5% for the highest current levels. This error dependence on current may be explained by the introduction of the parasitic contributor, which could itself be subjected to variations with different driving currents.

As already explained, one problem is related to the fact that R_{PZR-FA} cannot be used as a monitoring parameter (due to non-linear behavior with temperature), even if it would be a much better indicator of the effective coil temperature, as much closer to it (see Fig. 5.1).

To overcome the problem that R_{drive} is difficult to monitor in real-time (as not related to sensors output) and that R_{PZR-FA} cannot be used, the choice has been to evaluate the temperature reached by the slow-axis PZR (exploiting the relation obtained through the calibration step), to which must be added a new variable $\Delta T_{coil-SA}$ that defines the relation between T_{SA} and T_{coil}. In this way, it is possible to obtain the temperature at coil position starting from the one measured through slow-axis PRZs:

$$T_{coil} = T_{SA} + \Delta T_{coil-SA} \tag{5.3}$$

78
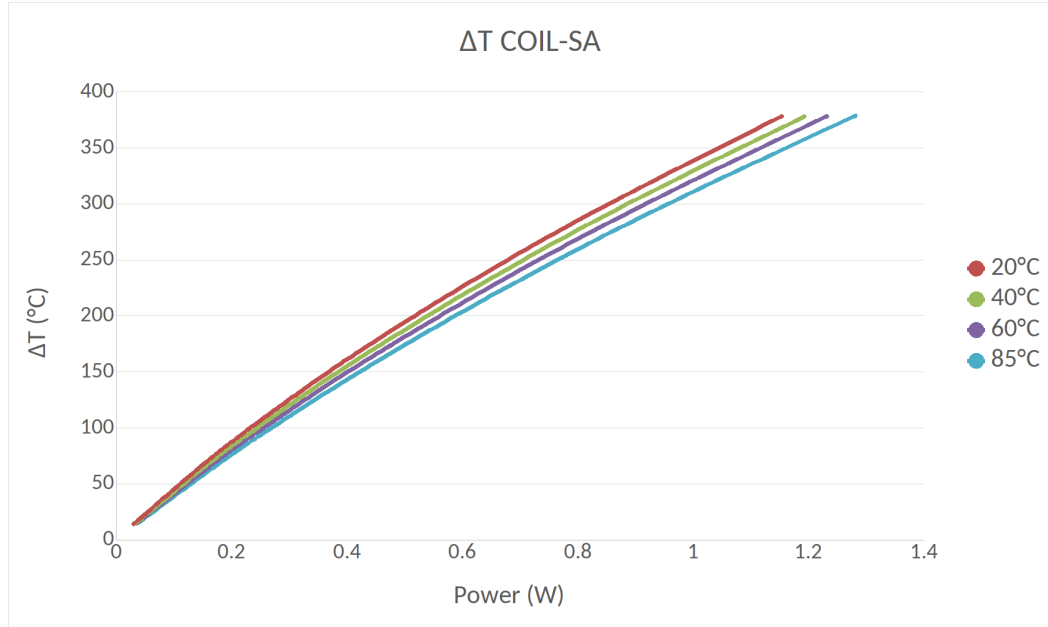
Figure 5.5: In figure are reported thermal model results, with the temperature difference between coil and SA sensor correlated with the power dissipated, for a set of four room temperatures $(20, 40, 60, 85°C)$.

Being the thermal resistance not constant (mainly due to changes in air thermal conductivity with temperature), the following relation is considered:

$$\Delta T_{coil-SA} = g(T_{amb}, P) \tag{5.4}$$

where g is a function of the ambient temperature and the power dissipated by a current flowing into the MEMS.

Through the FEM data fit, the following relation for the thermal model is derived:

$$T_{coil} = T_{SA} + \sum_{i=1}^{3} \left(\sum_{j=0}^{2} g_{ij} T_{room_j} \right) P_i \tag{5.5}$$

where the parameters g_{ij} are fitted from the FEM data and $P = R_{MEMS} i_{RMS}^2$ is the power dissipated by the considered current flowing into MEMS.

Through eq. (5.5) it is always possible to find a rather accurate value of the temperature reached by the coil by knowing three quantities: MEMS driving resistance (R_{MEMS}), driving current (i_{RMS}) and the room temperature at which the whole device is subjected (T_{room}). T_{SA}, instead, can be simply obtained thanks to the initial calibration (as shown in Fig. 5.2). In Fig. 5.5 are reported the relationships between $\Delta T_{coil-SA}$ and power dissipated ($P = Ri^2$) at different T_{room} conditions.

Based on assumptions and results presented until this point, a physical and a statistical model related to Cu-coil oxidation will be developed in the following sections.

5.1.2 Physical Model

A physical model have been developed in order to describe the oxidation process of Cu-coil, and to relate it with the progressive growth in its electrical resistance. A further purpose of this work is providing an assessment on acceptable current levels in Porcino device in relation to oxidation, taking into account environmental temperature effects.

For this activity, an experiment with tight control on test parameters have been set up by Characterization team. TVs of Porcino 3.1 without magnets have been tested in a set of DC currents (200mA, 210mA, 220mA, 230mA 240mA) and chassis temperatures (25°C, 40°C, 60°C, 73°C) relevant for device application and compatible with the on-going reliability tests. Driving current was provided by a DC generator, while room temperature was set by a hot plate. A schematic of the test setup is reported in Fig. 5.6.
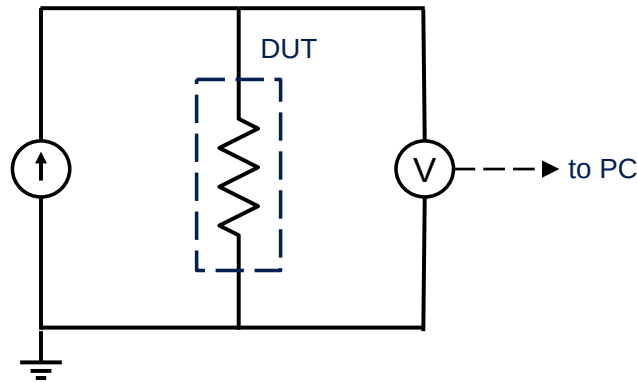
Figure 5.6: In figure is reported a schematic of the experimental setup used to collect data for oxidation model.

During these experiments, coil resistance have been monitored in real-time, and its relative variation has been taken as the parameter to estimate the level of oxidation of the coil. Such data have been fitted with a law for oxide evolution in time modified with respect to those typically found in literature [43–48]. It must be specified that a uniform growth of the oxide layer has been assumed. The relation used is the following one:

$$x_{ox}(E_a(T_{coil}), \alpha(T_{coil}), t) = \left[ct \exp\left(-\frac{E_a(T_{coil})}{RT_{coil}} \right) \right]^{\alpha(T_{coil})} \quad (5.6)$$

where x_{ox} is the oxide thickness at a certain time t, c is a constant, T_{coil} is the coil temperature that can be accurately estimated by eq. (5.5), and $E_a(T_{coil})$ is the activation energy of the system, function of the coil temperature, as well as the power exponent $\alpha(T_{coil})$. In particular, these two parameters follow the laws reported below:

$$E_a(T_{coil}) = E_{a_0} - E_{a_1} T_{coil} \quad (5.7)$$

$$\log(\alpha(T_{coil})) = -\alpha_0 + \alpha_1 T_{coil} \quad (5.8)$$

80
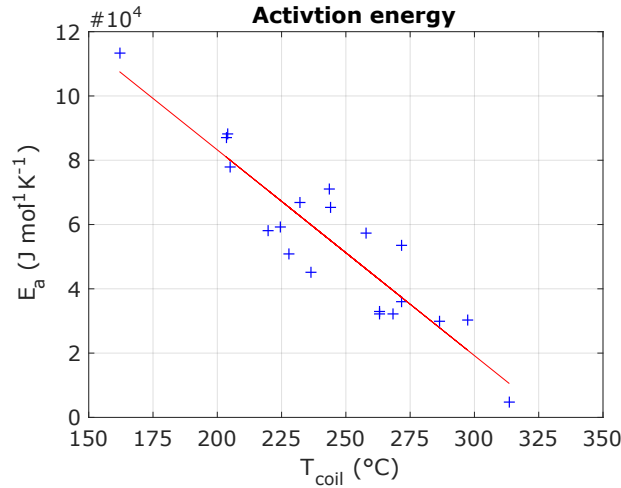
(a) Fitting of physical model parameter E_a with respect to coil temperature.
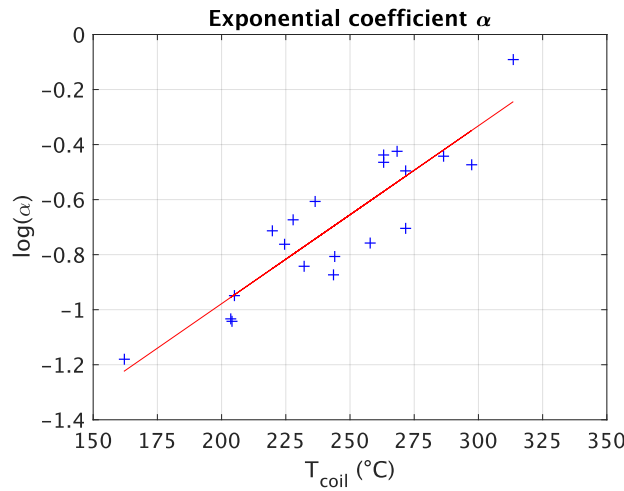
(b) Fitting of physical model parameter α with respect to coil temperature.

Figure 5.7: Fitting of physical model parameters (E_a and α) with respect to coil temperature. Each blue cross has been evaluated itself through interpolation of experimental data.

where E_{a_0}, E_{a_1}, α_0 and α_1 are the coefficients of these functions of coil temperature, found through a linear fitting of experimental data (see Fig. 5.7).

From oxide thickness, resistance variation can be easily derived. Indeed, coil resistance can be expressed as:

$$R_{coil} = \rho_{Cu} \frac{L}{wt} \tag{5.9}$$

where ρ_{Cu} is copper resistivity, L the coil length, w the coil width and t the coil thickness.

As oxidation goes on, the only variable that can change in eq. (5.9) is w, as coil length L is obviously a constant and t doesn't change because Cu is protected by Ni on top of it. Thus, when comparing the value of coil resistance at two different times ($R(t)$ and $R_0(t_0)$), from eq. (5.9) the following is obtained:

$$\frac{R(t)}{R(t_0)} = \frac{w(t_0)}{w(t)} \tag{5.10}$$

81
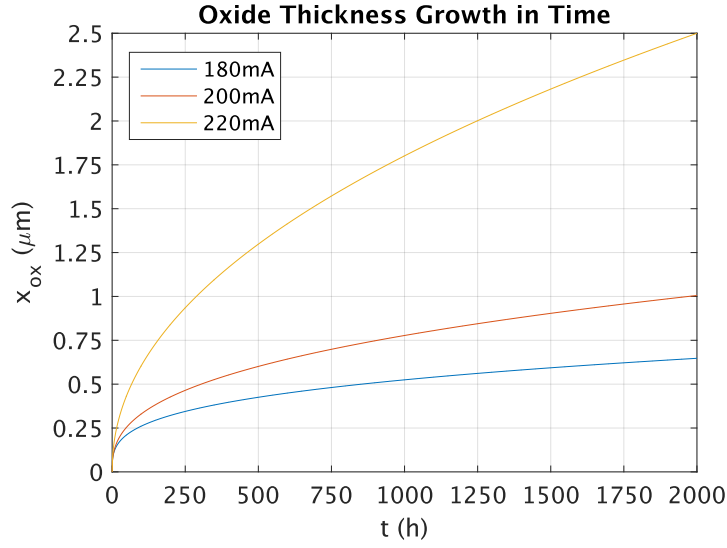
(a) Oxide thickness growth in time at different current levels (180, 200, 220mA)
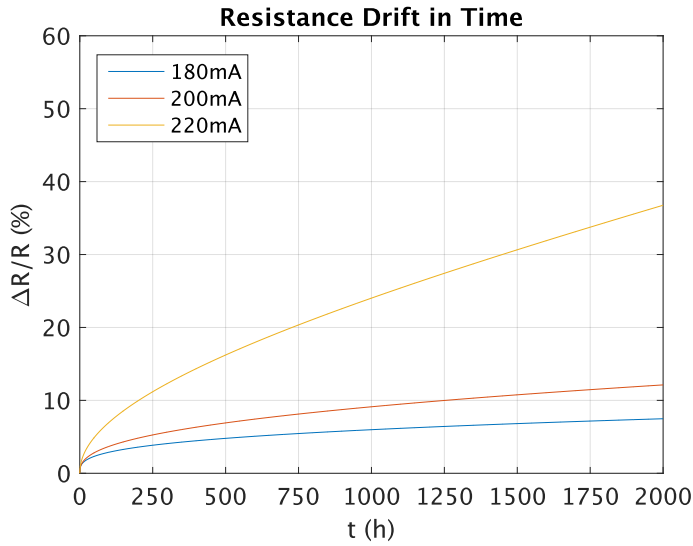
(b) Resistance drift in time at different current levels (180, 200, 220mA).

Figure 5.8: Oxide growth in time predicted by the physical model at different current levels.

It is clear that eq. (5.10) can be simply related to oxide growth, as while this process goes on Cu section becomes smaller and smaller (because Cu is progressively converted in CuO and doesn't conduct anymore). In first approximation, this phenomenon can be described at any time t as follows:

$$w(t) = w(t_0) - 2x_{ox}(t) \tag{5.11}$$

where the coefficient 2 is added to take into consideration the growth of oxide on both sides of the coil. As a final result, from eq. (5.9) and eq. (5.11) a relation between R_{coil} and x_{ox} is obtained:

$$R_{coil}(t) = \rho_{Cu} \frac{L}{t} \frac{1}{w(t_0) - 2x_{ox}(t)} \tag{5.12}$$
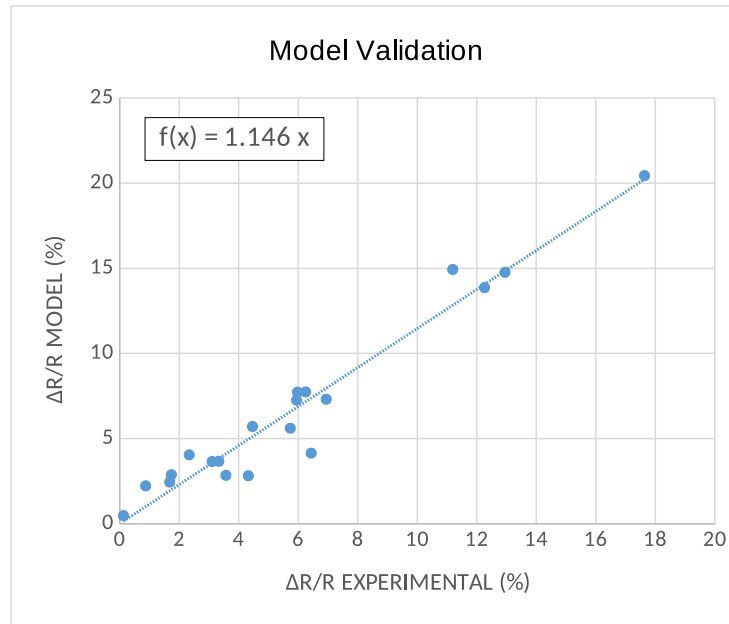
Figure 5.9: In figure are reported the resistance drifts calculated through the physical model against those measured experimentally, for a given current of 200mA. The fact that the slope of the fitting line is ~ 1, is a proof that model well describes the real oxidation behavior of Cu-coil.

Some results of the model are reported in Fig. 5.8a. They show oxide growth for a typical MEMS resistance value of Porcino 3.1 ($R = 5.2\Omega$) and maximum operating room temperature ($T_{room} = 60°C$). Each curve is related to a different current level during the test (180mA, 200mA and 220mA), and by using eq. (5.12) they can be transformed into their counterpart in terms of resistance Fig. 5.8b.

The validation of this empirical model has been done comparing results with available experimental data. As noticeable from Fig. 5.9, a good correlation has been found between the two. Indeed, the best fitting curve should have slope close to 1, which translates in a good average accuracy of the model. In this case, the slope is slightly higher than 1, but this isn't a problem, as it indicates that, on average, the empirical model is generally conservative.

 Another comparison has been done with data provided by Reliability team, coming from a DC test at 50°C. The graph in Fig. 5.10 shows that model predictions describe quite well experimental data for high currents (200mA and 220mA), while significantly overestimate them at lower current (180mA). This means that the model could be subjected to a loss of accuracy for low oxidation rates (maybe due to the fact that some assumptions made are no longer valid) or maybe that there are variations in oxidation dynamics at lower current levels (and so lower temperatures). It is clear that the behavior under these operating conditions is not well described, but the model is extremely conservative, so it can still be used to make useful considerations on the mean time to failure.

Finally, resistances variation at different times, obtained with data coming from the empirical model, have been compared with those measured by Reliability
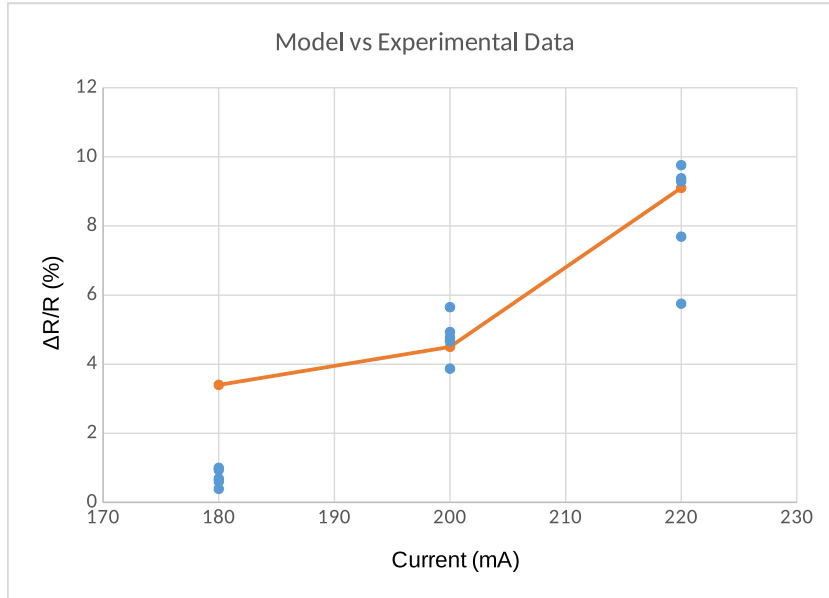
Figure 5.10: In figure are reported the results predicted by the physical model (orange line) and the experimental measurements (blue dots) against different driving currents. The model seems to describe well the real behavior of the device for high currents (200, 220mA), while highly overestimates resistance drifts at lower ones.

team during a DC test at 85°C with different driving currents (200 − 220mA), which was part of a pre-qualification activity with non-definitive setups, used just to find out the best testing conditions for the subsequent qualification. Data from these test are significantly scattered, even at equal nominal current (see Fig. 5.11). This spread is supposed to come from limitations in terms of control in testing conditions. Anyway, experimental data mostly fall inside expected range of the model, providing an indication that at least the oxidation trends are correctly evaluated.

Finally, results of the model applied to Porcino 3.1 (typical $R_{MEMS} = 5.2\Omega$) have been compared with those of the model applied to an older version (Porcino 2.3, typical $R_{MEMS} = 5\Omega$). Experimentally, a different oxidation rate has been seen for the two versions, with the older one showing a slower degradation. Taking into account the typical MEMS resistance difference, the model predicts a factor ~ 2 of oxidation acceleration in version 3.1 with respect to version 2.3 (see Fig. 5.12), in line with experimental observations.

Summarizing briefly, the empirical model seems to provide a good estimation of oxidation phenomenon occurring during DC test. Resistance change prediction is quite accurate for data collected in the DC test at 50°C, while a bit worse for the one at 85°C, anyway affected by limitations in terms of testing conditions control (however, trends and general behavior are correctly evaluated). Furthermore, accuracy at low current (less power dissipation, so lower temperatures) seems not that good, but the model results very conservative, so it can be effectively used to estimate current performances.

84
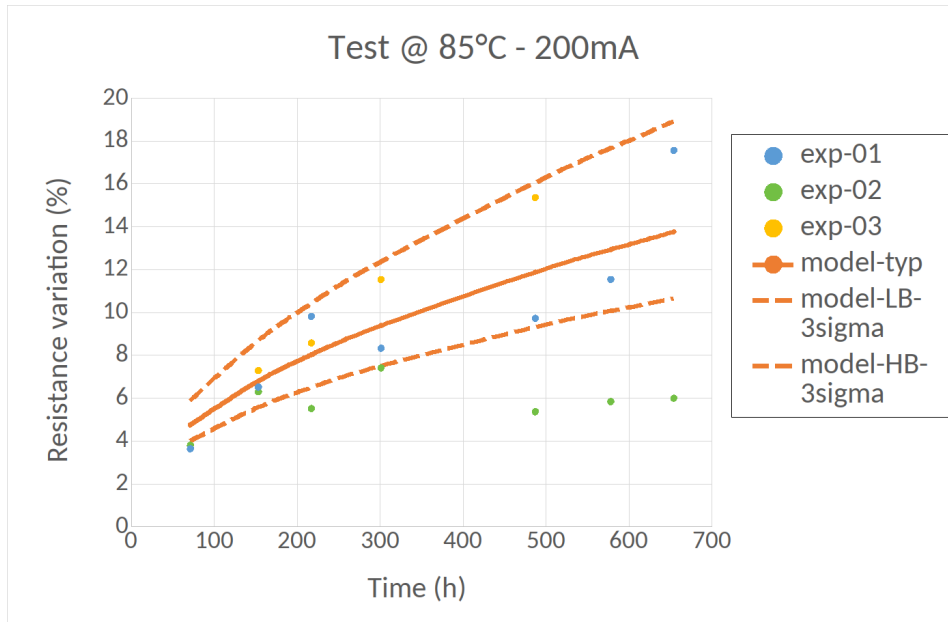
(a)
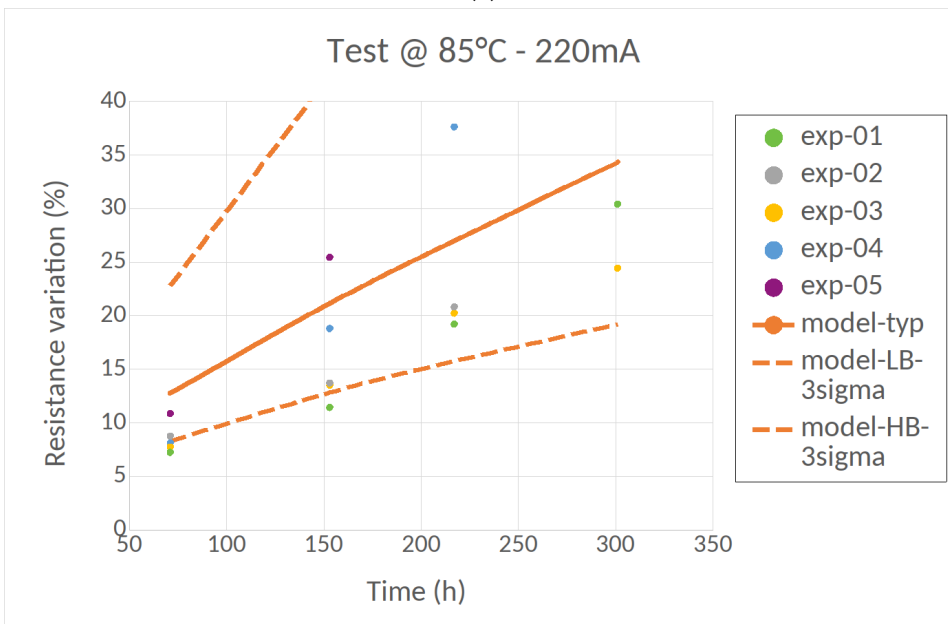
(b)

Figure 5.11: In figure are shown the results of coil oxidation model compared with some sets of experimental data at different testing currents and 85°C. These data are quite spread due to limitations in setup control (85°C are very close to hotplate maximum achievable temperature, so it can become unstable).
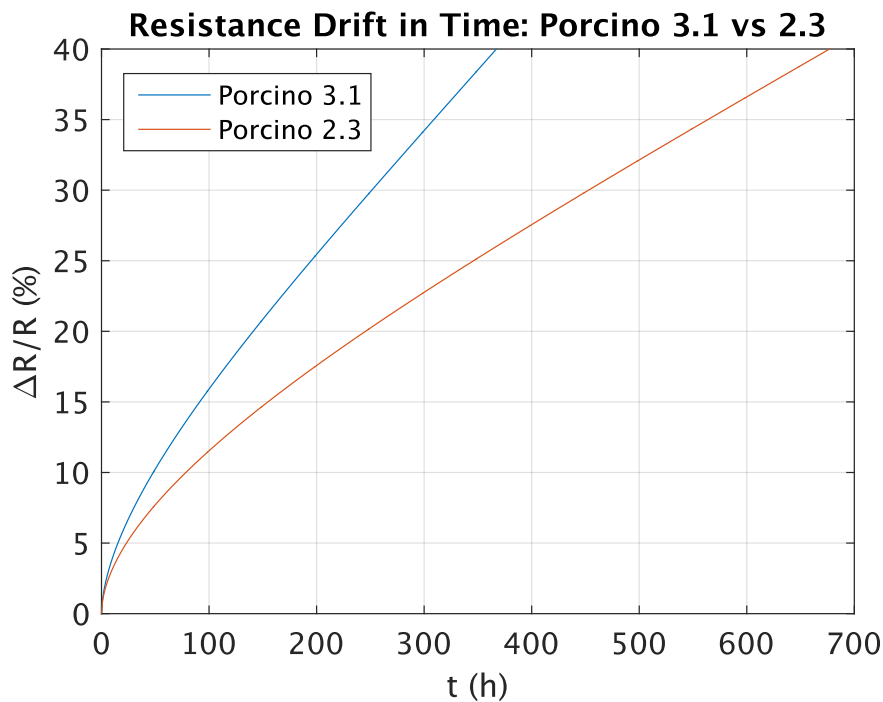
Figure 5.12: In figure is reported the plot of resistance drift in time for two different versions of Porcino. Porcino 2.3, as expected, shows a lower oxidation rate, because the coil resistance is typically smaller with respect to version 3.1.

5.1.3 Statistical Model

After physically modeling Cu oxidation he next step was the development of a predictive statistical model, able to describe Porcino failure probability over time under certain current and temperature conditions. As already explained, T and i are correlated quantities, and in this model, for what concerns current, only the thermal contribution have been considered, as Cu-coil oxidation is supposed to be driven mainly by temperature.

The work has been carried out exploiting concepts reported in chapter A, and was divided into three main phases:

1. Choice of the right statistical distribution to best describe the collected experimental data, and creation of a preliminary model that takes into account only devices considered as failed.

2. Improvement of the model through the *maximum likelihood estimate* (MLE), which takes into account not only failed TVs, but also those that survived beyond a certain time threshold (1000h for TVs at $180, 200$mA and 45h for TVs at 220mA).

3. Implementation of an Arrhenius-like relationship in order to be able to transpose model results to any temperature different from that of testing, or reached due to power dissipation ($P = Ri^2$).

86

This model was developed starting from experimental data collected during DC tests on Porcino 3.2, for which enough data were available to make the predictive model meaningful. TVs subjected to three different driving current (180, 200, 220mA) at 85°C for 1000h were considered. They came from two different lots, so as to try to take into consideration the possible differences in performance between one production batch and another, making the model of more general validity.

As reported in section 4.3, for DC test the failure condition was set for a drift in coil driving resistance of 10% but, for modeling purposes, also lower thresholds have been taken into account, in order to be even more conservative with respect to specs (e.g. $\Delta R_{th} = 5\%$).

Summarizing, data coming from many readout (168, 336, 500, 1000h for TVs at 180, 200mA, and 15, 36h for TVs at 220mA) of 50 samples were used, 20 of which were subjected to 180mA, 20 to 200mA and 10 to 220mA.

After the completion of this model, the same procedure was repeated with data collected from 1000h of DC test at 85°C on Porcino 3.4, which, as described in section 3.6, has a coil 27µm thick (5µm thicker than version 3.2), and therefore is able to withstand higher driving currents. For this reason, TVs of version 3.4 have been tested at higher current levels (200, 210, 220mA) providing good results that showed an appreciable improvement in oxidation resistance. In this case the readouts were carried out at 168, 336, 500, 1000h for TVs at 200, 210mA and at 72, 168, 336, 500h for TVs at 220mA. Also in this case 50 samples coming from two different batch were used: 20 of them were subjected to 200mA, 20 to 210mA and 10 to 220mA.

At the end, the two models have been compared in order to see if obtained results were coherent with the differences experimentally observed between version 3.2 and 3.4.

5.1.3.1 Failure Distribution Choice

The first step in the development of a statistical model is the collection of enough data and the choice of a failure condition, that is set as a threshold beyond which the device will be considered as failed, even if still functional (for example $\Delta R_{th} = 10\%$). After that, it is possible to verify which statistical distribution best fits experimental data and create a simple predictive model by following the procedure reported below.

This phase is divided in multiple steps, which must be carry out for each individual testing condition (i.e. for each current):

1. First of all, once the failure threshold condition has been chosen, the time t_i at which this condition is reached must be found for each device. In this way, also the total number of failed devices n can be indirectly obtained, which is an important quantity for step 2. To do this it is necessary to collect all the experimental data in a table (as the one reported in Tab. 5.1) and look for those samples that reached the failure condition within the testing time. As there wasn't a real-time monitoring of coil driving resistance, the only available data were those coming from readout measurements (four

Table 5.1: In table is reported an example of data collection for a DC test. In this case, data come from TVs of Porcino 3.2 subjected to 200mA for 1000h, but the same has been done for all the testing currents (180, 200, 220mA for version 3.2, and 200, 210, 220mA for version 3.4)

TV ID	$\Delta R\%$(168h)	$\Delta R\%$(336h)	$\Delta R\%$(500h)	$\Delta R\%$(1000h)	$t_i(\Delta R \geq 10\%)$
1	3.91	7.23	9.38	13.77	497.68h
2	3.27	7.34	9.91	13.85	486.54h
3	3.15	7.98	9.44	14.85	451.05h
4	2.48	4.90	7.93	9.21	no fail
5	4.17	6.15	9.18	10.07	870.07h
6	6.08	10.04	12.20	15.84	282.14h
7	7.46	12.88	16.85	23.93	176.16h
8	4.19	7.27	10.79	14.27	434.05h
9	5.26	9.17	11.43	15.54	333.22h
10	8.05	11.40	12.37	14.61	200.72h
11	4.81	7.66	10.04	10.96	631.47h
12	5.79	9.53	11.24	15.16	324.09h
13	4.48	6.85	9.08	12.06	621.47h
14	5.97	9.38	12.22	16.05	294.67h
15	5.36	9.45	12.85	15.86	303.25h
16	4.84	8.41	11.93	17.18	324.30h
17	6.26	10.13	12.49	16.45	267.51h
18	3.73	6.03	7.62	9.07	no fail
19	4.34	6.98	8.24	10.85	801.24h
20	1.53	3.23	7.65	6.12	no fail

data points for each tested TV between 0h and 1000h in this case). Obviously, considering the times to failure only in correspondence of the readouts would be a too rough approximation, since a TV survived at 336h but failed at 500h would have an uncertainty on the *TTF* of 164h (about a week!), and this wouldn't be acceptable for the predictive validity of the model. To overcome this problem and estimate the time at which failure occurred with a certain accuracy, a plotting of experimental data of coil resistance against time have been done, and then they have been fitted with a trend-line in order to best describe the behavior. It has been seen that an exponential trend-line is the one that best fit experimental data (also according to what described in section 5.1.2) and so it was used where more than two data-point were available, while it was necessary to settle for a linear fitting when only two data-points were available (version 3.2 at 220mA). In order to be as precise as possible, a threshold of $R^2 \geq 0.9$ has been set to have a good approximation for the fitting (see eq. (5.23)); if this condition wasn't satisfied, a bad data point was removed from the curve to improve the fitting, assuming some possible errors in the measurements. At this point, by using equations coming out from the fitting curves and combining with the desired resistance failure condition, it was possible to obtain a relatively accurate time to failure for each individual TV (see Fig. 5.13).
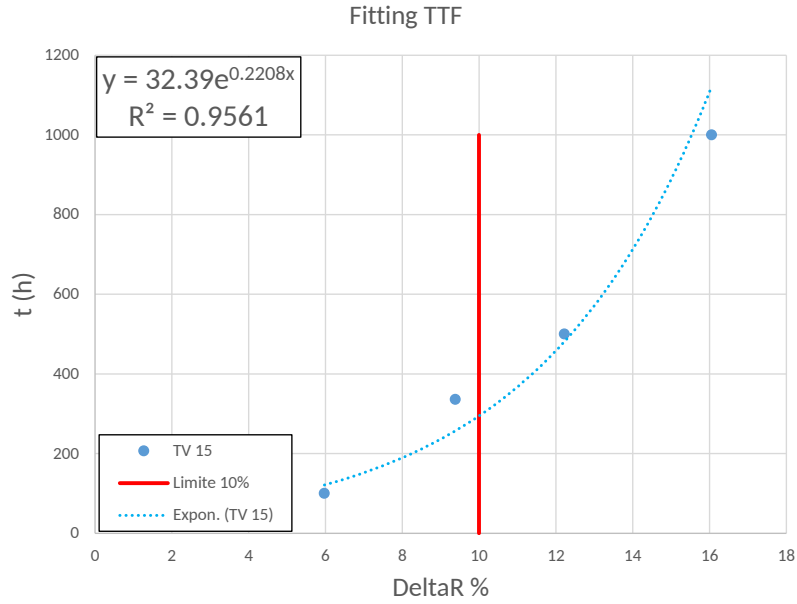
Figure 5.13: In figure is reported the fitting of time-to-failure (TTF) of a TV tested at a certain current. From the fitted equation, setting a failure condition considering a ΔR_{th} (10% in this case), a TTF can be predicted.

In this way the TTF vector t_i has been built (Tab. 5.1), and the number of failed devices n has been found (**N.B.** the device is considered as failed only if $TTF \leq testing\ time$!).

2. Next step is to build the empirical cumulative probability curve. To do this, the elements of t_i must be sorted in ascending order, from the smallest to the largest, and an index i must be assigned to each component of this sorting. The empirical cumulative probability q_i must be defined depending on the number of available data (number of failure events n) and it is an estimate for the cumulative probability function $F(t_i)$. Indeed, according to [21]:

   - $q(t_i) = q_i = \frac{i}{n+1}$ for $n > 10$

   - $q(t_i) = q_i = \frac{i-0.3}{n+0.4}$ for $n \leq 10$

   Thus, depending on results from every testing condition, a formula has been used instead of the other one.

   The empirical probability q_i at a given condition can be compared with results coming from the following models, as it is a statistical description of experimental data points.

3. The final step consists in building the probability paper for each failure distribution considered as a candidate to describe the experimental data (some examples are normal, log-normal, negative exponential and Weibull distribution; for more information see section A.2).

   Through this passage, cumulative distribution functions (CDF) are linearized, so that it is possible to verify their validity and to estimate the correspondent parameters (e.g. $\mu, \sigma, \lambda, \alpha, \beta$, see section A.2) through a linear fitting, after data have been accurately plotted on a proper scale.

For this model, negative exponential distribution wasn't taken into account, as it is not suitable for describing degenerative phenomena such as oxidation of the copper coil.

As each failure distribution must be linearized, the quantities to be plotted are different depending on the considered distribution. In particular, starting from the percentile of each of them, which indicates the values below which a certain percentage of the data in a data set is found, it is possible to obtain these linear relationships:

- The relationship that linearize $F(t_i)$ for the **Weibull distribution**, considering $F(t_i) \asymp q_i$, is easily obtained by the percentile formula (see section A.2):

$$t_i = \alpha[-\ln(1 - q_i)]^{\frac{1}{\beta}} \tag{5.13}$$

By simply using the natural logarithm on both sides:

$$\ln(t_i) = \ln(\alpha) + \frac{1}{\beta}\ln[-\ln(1 - q_i)] \tag{5.14}$$

This means that, if $[t_i, \ldots, t_n]$ are realizations of a sample coming from a population with Weibull distribution, the points $(\ln(-\ln(1 - q_i)), \ln(t_i))$ should be approximately placed on a line with $m = 1/\beta$ and $q = \ln(\alpha)$. Thus, α and β are estimates of the Weibull distribution parameters (where α is the scale factor and β the shape factor of the distribution).

- Also for **normal distribution** let's start from some typical relations, reported in section A.2. The percentile formula for this distribution is:

$$t_p = \mu + z_p\sigma \tag{5.15}$$

where z_p is the percentile of the standard normal distribution $\Phi(z)$. Also, it is true that:

$$F(t_i) = \Phi(z) \rightarrow z = \Phi(F(t_i))^{-1} = \Phi(q_i)^{-1} \tag{5.16}$$

where $\Phi(q_i)^{-1}$ is the inverse of the normal standard distribution of the empirical cumulative probability q_i.

Combining these equations results:

$$t_i = \mu + \Phi(q_i)^{-1}\sigma \tag{5.17}$$

So, if $[t_1, \ldots, t_n]$ is the realization of a sample from a population with normal distribution, the points $(\Phi(q_i)^{-1}, t_i)$ should be arranged approximately on a line with $m = \sigma$ and $q = \mu$. Thus, μ and σ are estimates of normal distribution parameters (where μ is the mean time to failure and σ the standard deviation of the distribution).

- **Log-normal distribution** behaves almost in the same way as a normal one. Indeed, the assumption is that if $x = \ln(t)$ is a random variable following a normal distribution, then t follows a log-normal one.

90

Starting from eq. (A.44), it is possible to linearize the log-normal CDF:

$$z = \frac{\ln(t/T_{50\%})}{\sigma} \rightarrow \ln(t) = \ln(T_{50\%}) + z\sigma \rightarrow \ln(t) = \mu + z_p\sigma \quad (5.18)$$

which is very similar to eq. (5.15). $T_{50\%}$ is the median lifetime ($F(T_{50\%}) =$ 50%) and $T_{50\%} = \exp(\mu)$.

From here the procedure is the same as for normal distribution. Indeed, as reported in section A.2, holds:

$$F(t_i) = \Phi(z) \rightarrow z = \Phi(F(t_i))^{-1} = \Phi(q_i)^{-1} \quad (5.19)$$

And so:

$$\ln(t_i) = \mu + \Phi(q_i)^{-1}\sigma \quad (5.20)$$

Thus, if $[t_1, \ldots, t_n]$ is the realization of a sample from a population with log-normal distribution, the points $(\Phi(q_i)^{-1}, \ln(t_i))$ should be arranged approximately on a line with $m = \sigma$ and $q = \mu = \ln(T_{50\%})$. So, m and q are estimates of the log-normal distribution parameters (where μ is the logarithm of mean time to failure and σ the standard deviation of the distribution).

To formulate a judgment on the significance of the representations (assuming a linear correlation between the variables), the first quantity to be calculated is the standard error:

$$S_{Y|X} = \sqrt{\frac{\sum(y_i - \hat{y}_i)^2}{n-2}} \quad (5.21)$$

which gives an idea of the dispersion of points around the trend line. Furthermore, defining:

$$S_Y^2 = \sum(y_i - \hat{y}_i)^2 \quad (5.22)$$

it is possible to introduce the coefficient of determination R^2:

$$R^2 = \sqrt{1 - \frac{S_{Y|X}^2}{S_Y^2}} \quad (5.23)$$

In this work, X is referred to the variable related to time t_i and Y to the one related to probability q_i. R^2 expresses the contribute of X to the variation of Y. In particular, this parameter allows to express a judgment on the correlation between two variables:

- for $R^2 \leq 0.5$ the correlation is not significant;

- for $0.5 < R^2 \leq 0.9$ there is moderate correlation;

- for $R^2 \geq 0.9$ the correlation is strong.

Results of this first step for Porcino 3.2 are reported in Fig. 5.14 for $i = 200\text{mA}$, and in Fig. 5.15 for $i = 220\text{mA}$, both at $T_{room} = 85°C$, considering a $\Delta R_{th} = 10\%$. From these, it is noticeable that the statistical distribution which best describes

Table 5.2: In table is reported an example of data processing for a DC test. In this case, data come from TVs of Porcino 3.2 subjected to 200mA for 1000h, but the same has been done for all the testing currents (180, 200, 220mA for version 3.2, and 200, 210, 220mA for version 3.4)

TV ID	$t_{i_{fail}}$(h)	i	$q_i(\%)$	$t_{pred_{fail}}$(h)
7	176.16	1	5.5	172.49
10	200.72	2	11.1	208.65
17	267.51	3	16.6	237.47
6	282.14	4	22.2	263.38
14	294.67	5	27.7	288.05
15	303.25	6	33.3	312.39
12	324.09	7	38.8	337.01
16	324.30	8	44.4	362.46
9	333.22	9	50.0	389.28
8	434.05	10	55.5	418.08
3	451.05	11	61.1	449.66
2	486.54	12	66.6	485.10
1	497.68	13	72.2	526.08
13	621.47	14	77.7	575.36
11	631.47	15	83.3	638.14
19	801.24	16	88.8	726.27
5	870.07	17	94.4	878.55

the oxidation phenomenon of the Cu-coil is the log-normal one. Indeed, as reported in literature [21], this distribution is particularly suitable for describing phenomena related to degradation, like resistance increase due to copper oxidation.

More in detail, curves have been plotted with their upper and lower predictive bands, taking into account a confidence level of 95%. In captions of Figures 5.14 and 5.15 are reported other than the coefficient R^2, also the parameter estimates for every analyzed distribution.

At this point, with parameters obtained through the linear fitting, it is possible to obtain a first model which, however, only considers failed TVs between 0h and 1000h (and not those that survived). Therefore its predictions are limited to this time interval, and they don't give a representation of the real distribution, as at 1000h corresponds a probability of failure of 100%, as visible in Fig. 5.16. Thus, if someone desires to predict the percentage p_i of TVs that will fail at a certain time t_i, it is possible by considering p_i as a function of t_i and the parameters μ and σ through the distribution that best describes experimental data (log-normal in this case). Calculations can be done by a software tool, like *Excel* or *MatLab* as:

$$p_i = LOG.NORM(t_i, \mu, \sigma) \tag{5.24}$$

or simply through the percentile:

$$\ln(t) = \mu + z_p \sigma \tag{5.25}$$
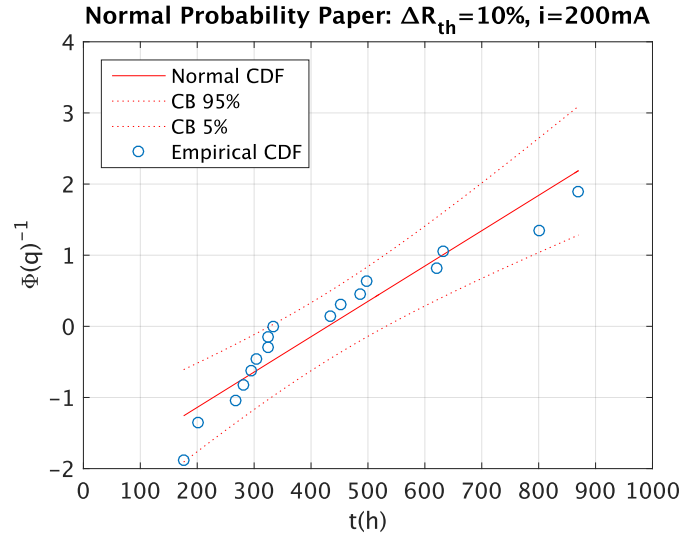
(a) Normal dist.: $\mu = 429.39, \sigma = 201.30, R^2 = 0.9095$
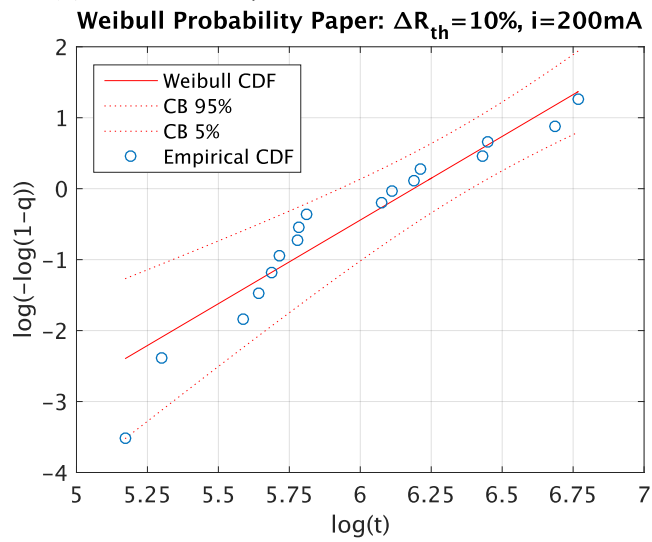
(b) Weibull dist.: $\alpha = 486.69, \beta = 2.36, R^2 = 0.9346$
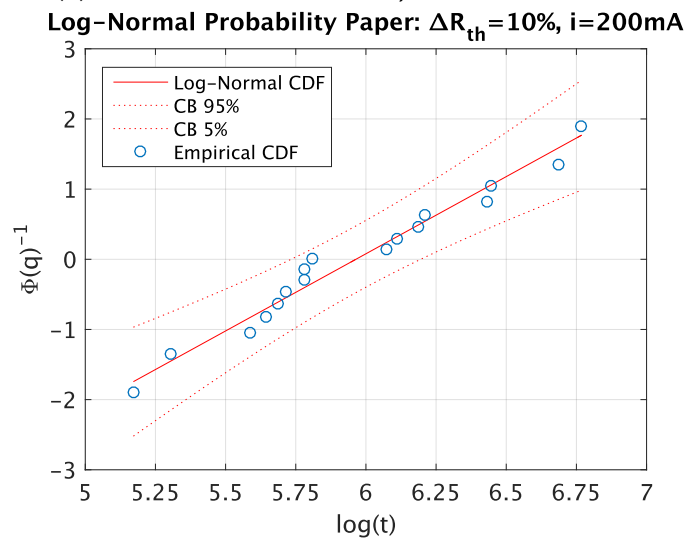
(c) Log-normal dist.: $\mu = 5.96, \sigma = 0.45, R^2 = 0.9756$

Figure 5.14: Probability paper for each failure distribution at 200mA and $T_{room} = 85°C$, considering $\Delta R_{th} = 10\%$.

(a) Normal dist.: $\mu = 34.88, \sigma = 3.63, R^2 = 0.9377$

(b) Weibull dist.: $\alpha = 36.55, \beta = 9.61, R^2 = 0.0.8696$

(c) Log-normal dist.: $\mu = 3.55, \sigma = 0.10, R^2 = 0.9546$
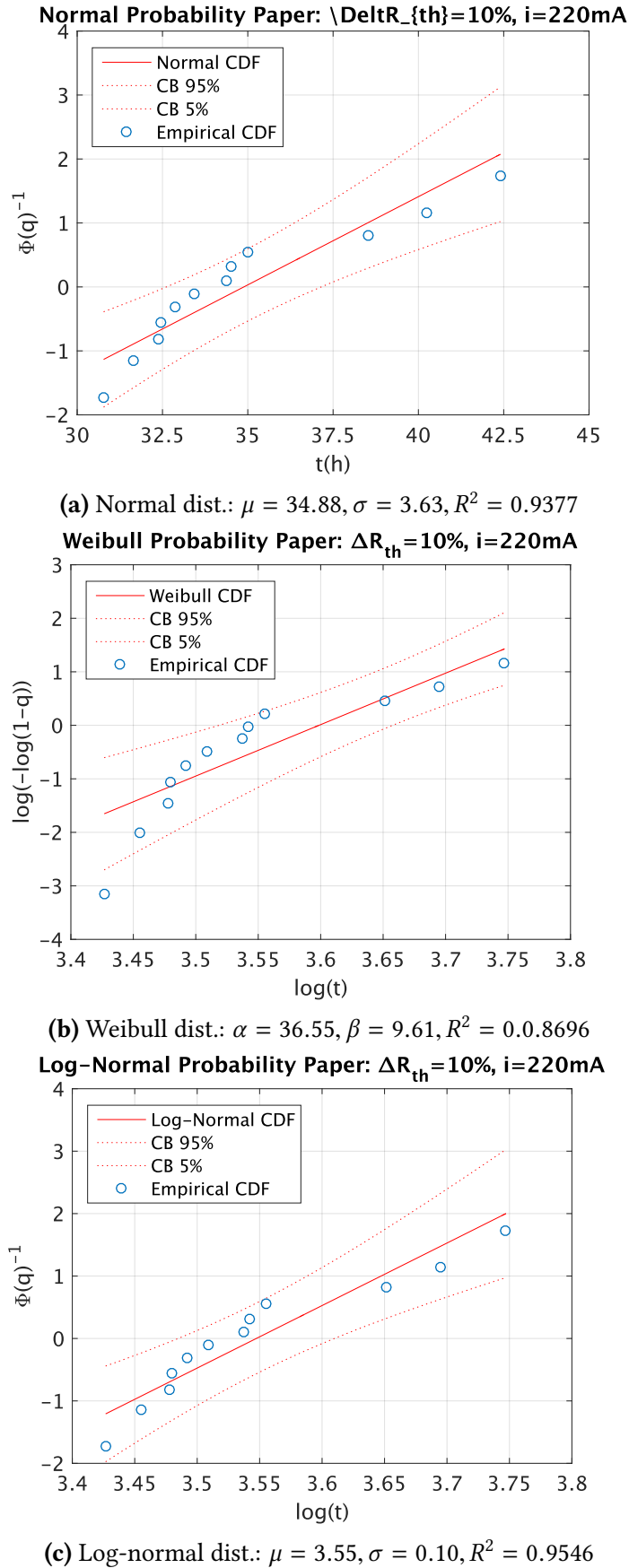
Figure 5.15: Probability paper for each failure distribution at 220mA and $T_{room} = 85°C$, considering $\Delta R_{th} = 10\%$.
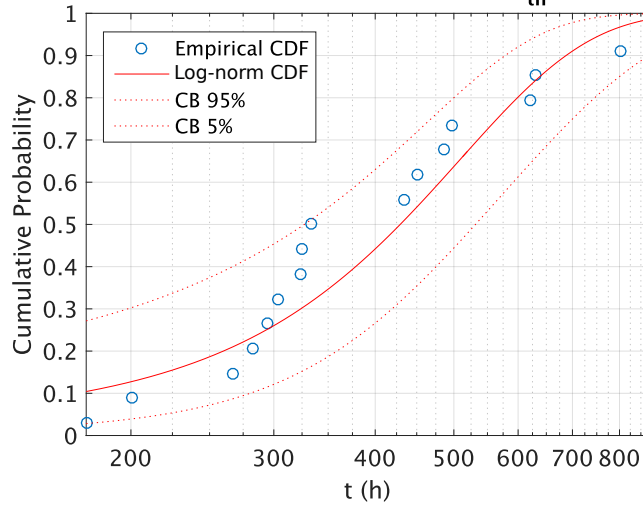
(a) Log-normal CDF at $i = 200$mA and $T_{room} = 85°$C
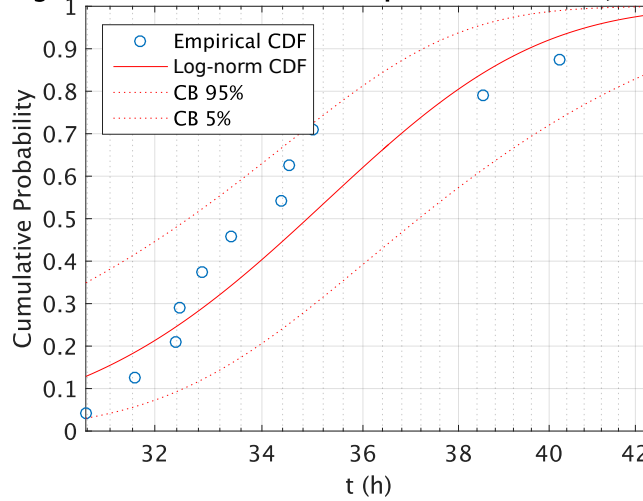
(b) Log-normal CDF at $i = 220$mA and $T_{room} = 85°$C.

Figure 5.16: Log-normal CDF at $i = 200, 220$mA and $T_{room} = 85°$C

Also the inverse calculation is possible, and so, if it is necessary to predict at what time t_i a percentage p_i of TVs would fail, it can be done as:

$$t_i = LOG.NORM.INVERSE(p_i, \mu, \sigma) \tag{5.26}$$

Of course the name of the functions will be different depending on the software used, but the concept is completely the same.

Finally, an example of some results obtained up to this point for the set of data at $i = 200$mA are shown in Tab. 5.2.

5.1.3.2 Maximum Likelihood Estimate (MLE)

After showing that the distribution which best describes DC tests experimental data is the log-normal one, the new objective is to estimate the distribution parameters μ and σ in a more precise way, taking into account both the number of failed devices and those that survived.
In this way, it is possible to extend the time range in which the model can predict the failure of TVs beyond the actual testing time, making it much more realistic.

To do this, the *Maximum Likelihood Estimate* (MLE) method has been employed, using the same data collected during the preliminary analysis (explained in section 5.1.3.1).

Let $[t_1, \ldots, t_n]$ be the values of time to failure extracted from a population having a log-normal probability density function $f(t) = f(t|\mu, \sigma)$, with μ and σ parameters of the distribution.
The probability of failure of a TV at a time within the interval $\left[t_i - \frac{dt}{2}; t + \frac{dt}{2}\right]$ is:

$$P_i = f(t_i|\mu, \sigma)dt \tag{5.27}$$

The probability that a TV will survive beyond the time t'_j is:

$$P'_j = 1 - F(t'_j|\mu, \sigma) \tag{5.28}$$

The effective probability of failure of a TV at a certain time can be obtained passing through the Likelihood function L:

$$L(\mu, \sigma) = \prod_i f(t_i|\mu, \sigma)dt \cdot \prod_j \left[1 - F(t'_j|\mu, \sigma)\right] \tag{5.29}$$

This function allows to estimate the parameters of the chosen distribution considering both the failed devices and the survived ones. Indeed the values of μ and σ that maximize $L(\mu, \sigma)$ are the parameter estimates ($\hat{\mu}$ and $\hat{\sigma}$) of the chosen distribution.
For convenience in the calculations it is better to use $l(\mu, \sigma) = \ln(L(\mu, \sigma))$:

$$l(\mu, \sigma) = \sum_i \ln\left[f(t_i|\mu, \sigma)\right] + \sum_j \ln\left[1 - F(t'_j|\mu, \sigma)\right] + n\ln(dt) \tag{5.30}$$

As the last term of eq. (5.30) is not dependent by μ or σ, and as to maximize the function a derivative operation with respect to this parameters must be done, it is not necessary to take it into consideration.

Thanks to this method, much more realistic parameters of the considered failure distribution (log-normal in this case) can be found. These calculations have been made at first with *Excel 2016*, and then carried out also with *MatLab*.

In this way the model is able to effectively predict the failure probability over

96

an unlimited time interval $[0; +\infty]$ rather than a limited one, as in the case described in section 5.1.3.1 $[0; t_{test} = 1000\text{h}]$.

Obviously, if all the TVs fails within the threshold time for survival, parameters estimates $\hat{\mu}$ and $\hat{\sigma}$ obtained through MLE converge to the values of those found with probability papers, and so this procedure becomes unnecessary. On the other hand, if none of the TVs fails within the threshold time, MLE loses its meaning, as it simply means that the considered operating conditions are safe for the device.

The methodology to predict the time at which a certain percentage of TVs is failed, or vice versa, is the same described at the end of section 5.1.3.1.

Results of the model for $i = 200, 220\text{mA}$ are reported in Fig. 5.17 with a confidence level of 95%, and also experimental data have been plotted to compare predictions with reality. Results at $i = 180\text{mA}$ are not present in the plot, as no failures occurred in these conditions.

5.1.3.3 Arrhenius-like Relationship

After having extended the prediction time range of the probabilistic model, the next step was to transpose the obtained results to temperatures different from those of testing. In this way, it is possible to completely disengage from the experimental set-ups and be able to predict the behavior of Porcino without the need to test devices at every operating condition of interest.

In particular, it is possible not only to predict the failure probability in time at different room temperatures, but also at different driving currents, as each of them corresponds to a precise coil temperature. Indeed, as already reported in section 4.2.3.2, a calibration procedure has been done in order to correlate slow-axis PZRs output with local temperature, and being able to evaluate coil temperature at every time instant using eq. (5.5), according to what explained in section 5.1.1. Testing driving currents were 180mA, 200mA and 220mA, approximately corresponding to a coil temperature of 205°C, 245°C and 285°C

The considerations and method are the same employed for the simple MLE (see section 5.1.3.2), but the mean-time-to-failure parameter μ used in the distribution (again log-normal) was rewritten as a function of temperature (T_i), as well as the standard deviation σ. More in detail, an Arrhenius-like relationship has been chosen as the more appropriate for describing this phenomenon, because the increase in coil resistance is due to the progressive narrowing of the coil section due to the oxidation of the Cu, which is a phenomenon that is mostly thermally driven:

$$t = A \exp\left(-\frac{E_a}{k_B T}\right) \tag{5.31}$$

where A is a pre-exponential factor, E_a the activation energy of the phenomenon, $K_B = 8.625 \times 10^{-5} \text{eVK}^{-1}$ the Boltzmann constant and T the absolute temperature.
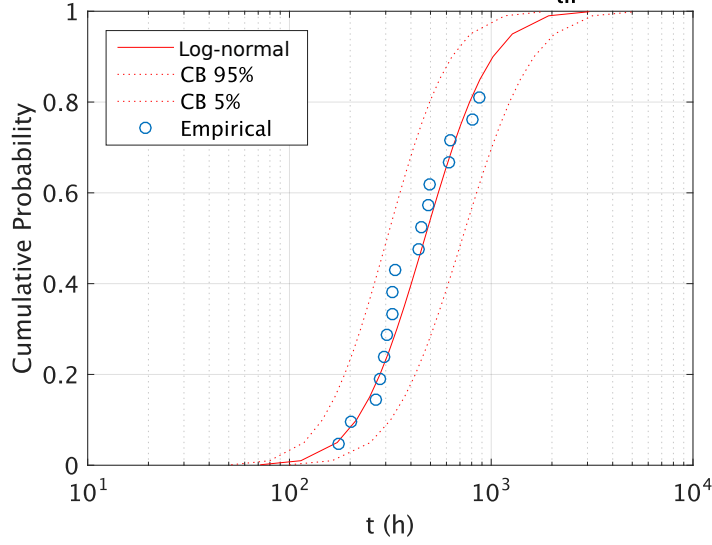
(a) Log-normal CDF at $i = 200$mA and $T_{room} = 85°C$: $\mu = 6.15$, $\sigma = 0.61$
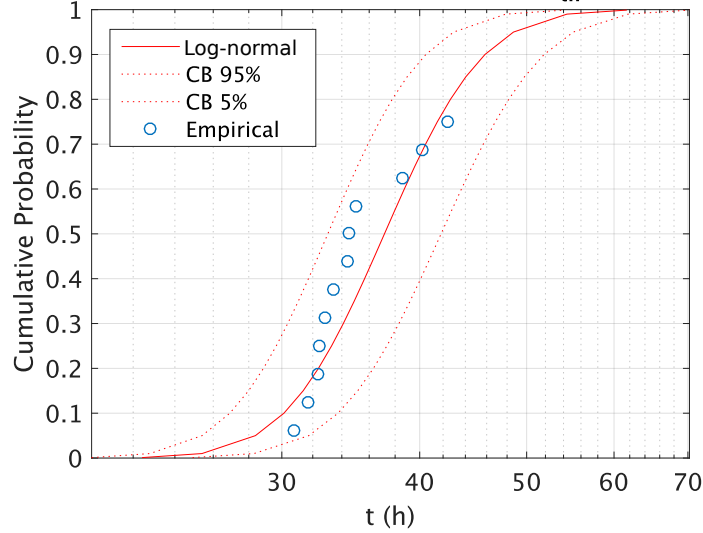
(b) Log-normal CDF at $i = 220$mA and $T_{room} = 85°C$: $\mu = 3.62$, $\sigma = 0.16$.

Figure 5.17: Log-normal CDF at $i = 200, 220$mA and $T_{room} = 85°C$ with distribution parameters calculated through MLE method.

Rewriting $-E_a/k_B = B$, this relation can be also linearized as:

$$\ln(t) = \ln(A) + \frac{B}{T} \tag{5.32}$$

Consequently, given that the average time to failure μ and the standard deviation σ are quantities both referable to a time value, they can be rewritten as a function of temperature as follows:

$$\mu_i = \mu_0 + \mu_1 \frac{1}{T_i} \tag{5.33}$$

$$\sigma_i = \sigma_0 + \sigma_1 \frac{1}{T_i} \tag{5.34}$$
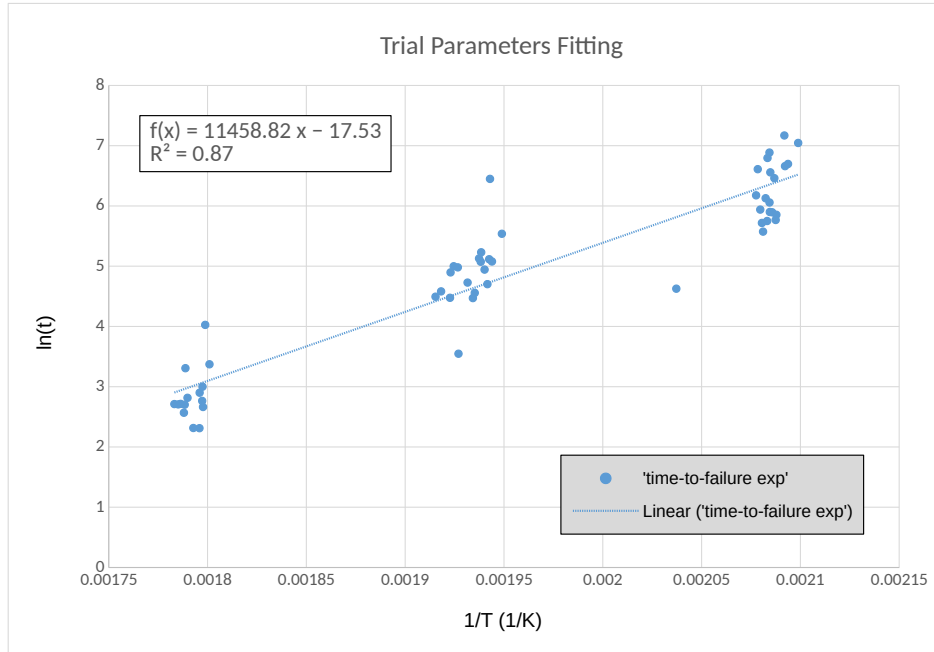
Figure 5.18: In figure is reported the fitting done in order to choose some good trial values of μ_0 and μ_1 to use in the MLE method.

where μ_0 and σ_0 are the pre-exponential coefficients of the Arrhenius-like relationship ($\ln(A)$), and μ_1 and σ_1 represent the terms including activation energy (B).

Thus, this time it was necessary to maximize the Likelihood function with respect to four different parameters: μ_0, μ_1, σ_0 and σ_1. This is a bit tricky, because there are many available parameters combinations able to maximize the function, so in order to start the maximization as close as possible to the maximum itself, some good trial parameters must be chosen. This is important because the risk is not to find out the absolute maximum of the function but just relative ones, preventing the right estimation of the distribution parameters.

To do this, a linear fitting of logarithm of experimental failure times versus the inverse of coil temperature of each TV, independently from the driving current has been done (see Fig. 5.18). From the linear trend-line equation, the starting trial parameters have been found as $\mu_0 = q$ and $\mu_1 = m$. Please note that having a low value of R^2 is not a problem in this case, because these are just starting coefficients that will be automatically corrected during Likelihood function maximization, keeping constant the starting value of σ_0 and σ_1. After the estimation of μ_0 and μ_1, by keeping constant their result, also the estimates of σ_0 and σ_1 have been evaluated. In this case the right estimation was a bit tricky, because there wasn't a method to choose some good starting values for them. For this reason, some trials have been done in order to find effectively the absolute maximum of the function, checking every time if results were coherent with experimental data and if the effective value of σ itself at a certain temperature was reasonable with respect to previous results and values find in literature.

Once μ_0, μ_1, σ_0 and σ_1 have been estimated (using the code reported in Listing 1),
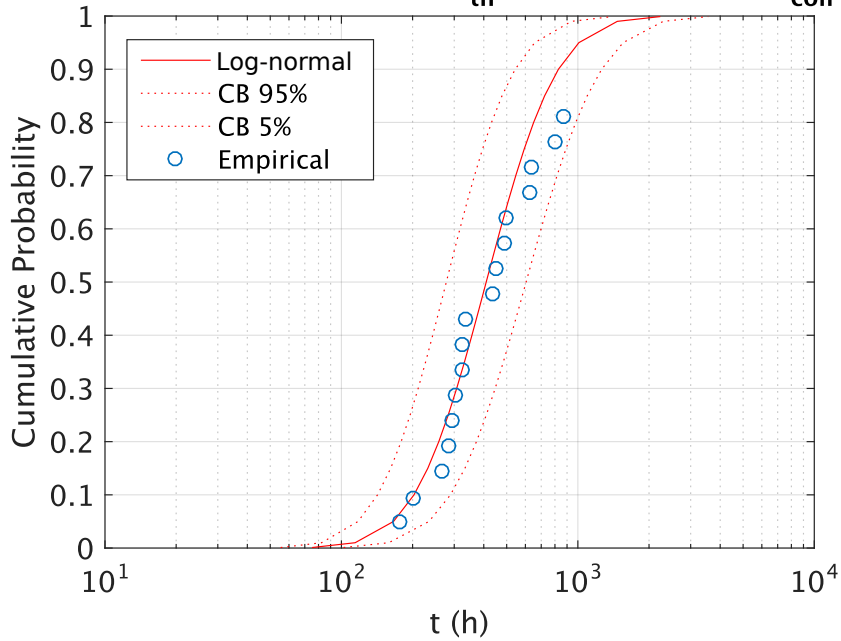
(a) Log-normal CDF at T_{coil} = 515K (corresponding to 200mA at T_{room} = 85°C) compared with experimental data.
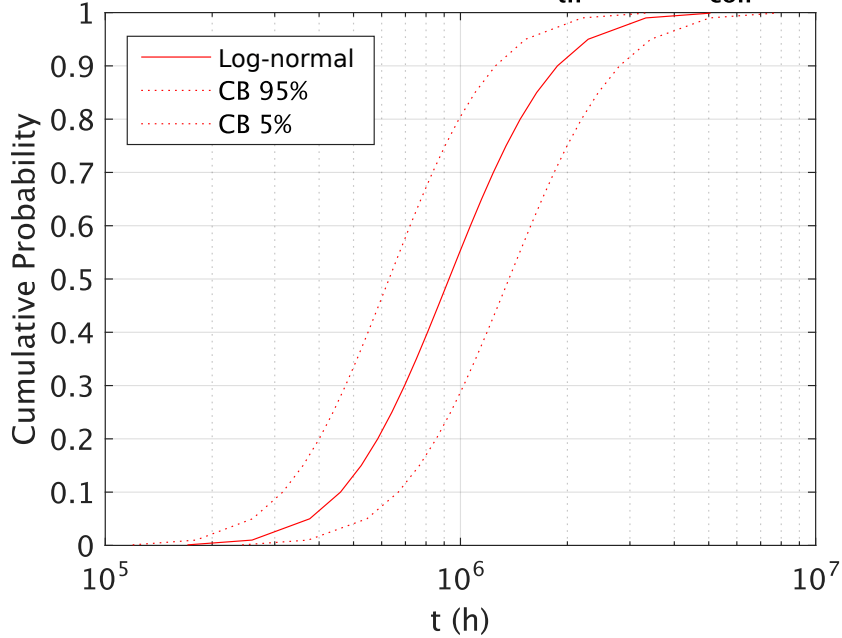
(b) Log-normal CDF prediction at T_{coil} = 400K (corresponding to operative conditions $\sim$ 150mA at T_{room} = 60°C).

Figure 5.19: Log-normal CDF with temperature dependent parameters (Arrhenius dependence) calculated through MLE method.

μ and σ can be recalculated with eq. (5.33) and eq. (5.34) for any temperature of interest, and from them, failure distributions related to a precise temperature (or better, to a precise driving current) can be obtained. To report some achievements, in Fig. 5.19a it is shown that results are consistent with experimental data, and in Fig. 5.19b is reported a prediction of times-to-failure in real operating conditions ($i \simeq 150$mA at $T_{room} \simeq 60°C \rightarrow T_{coil} \simeq 128°C \simeq 400$K), where the temperature of the coil has been evaluated thanks to the thermal model described in section 5.1.1.
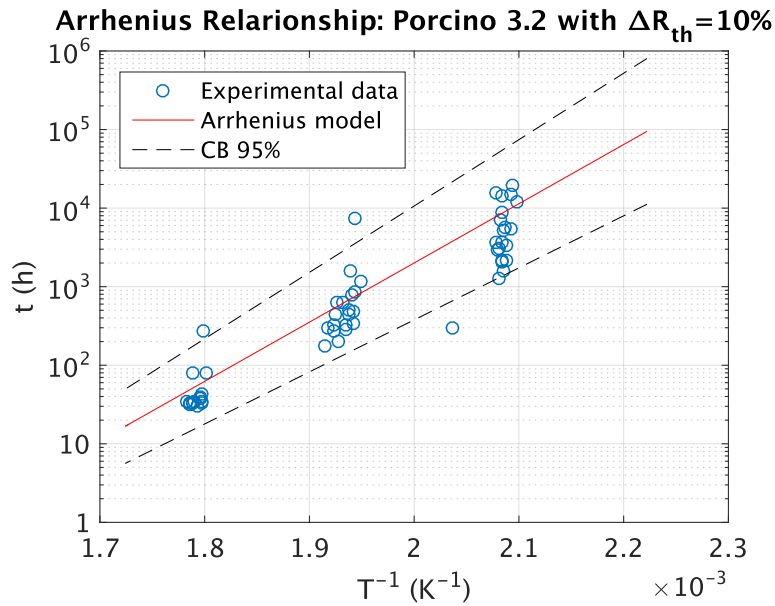
(a) MTTF ($F(t) = 50\%$) of Porcino 3.2 at different temperatures considering a $\Delta R_{th} = 10\%$.
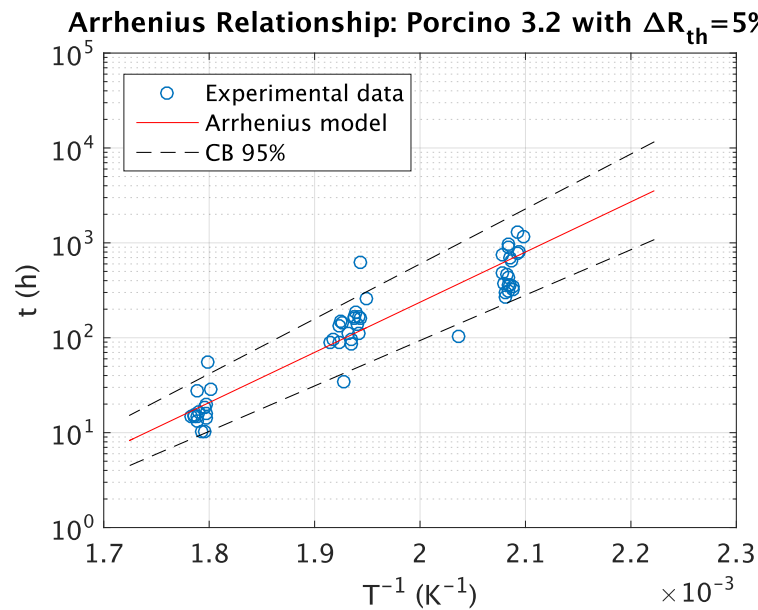
(b) MTTF ($F(t) = 50\%$) of Porcino 3.2 at different temperatures considering a $\Delta R_{th} = 5\%$.

Figure 5.20: In figure are reported the meat-time-to-failure (MTTF) of Porcino 3.2 at different temperatures considering two threshold resistance drifts ΔR_{th}.

Some other useful information can be obtained through this model. Indeed, exploiting eq. (5.33), it is possible to predict the mean time to failure $MTTF$ (time at which 50% of devices fails) of Porcino for every temperature, as visible in Fig. 5.20. It is interesting how the confidence on $MTTF$ increase at higher temperatures, because, as expected, these are more severe conditions for TVs and they tend to fail more surely. Thus, with increasing temperatures, accuracy on the prediction tends to gets higher and higher.
As visible in Fig. 5.20b, the whole procedure has been repeated considering $\Delta R_{th} = 5\%$, which is a more restrictive failure condition.
Looking to results and comparisons with experimental data, the model seems to predict quite well the behavior of Porcino 3.2 and its failure probability in time at different temperature (and so current) conditions.

5.1.3.4 Comparison Between Porcino 3.2 and 3.4

After the statistical model has been developed and validated for Porcino 3.2, the same work has been done identically on version 3.4, in order to see if any difference would be found. Indeed, as already reported, Porcino 3.4 has a coil thicker than version 3.2 (5μm more), and so it should be able to withstand higher values of driving current without failing. As already explained in chapter 4, this has been proved with experimental tes ts, thus also the statistical model is expected to emphasize this behavior.
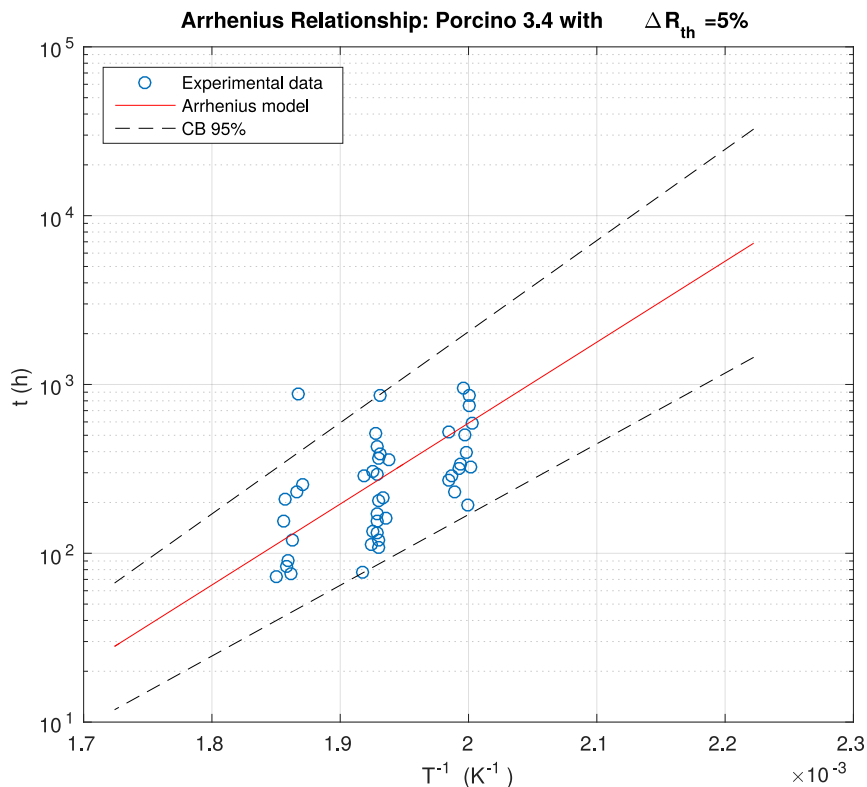
Figure 5.21: In figure is reported the MTTF ($F(t) = 50\%$) of Porcino 3.4 at different temperatures considering a $\Delta R_{th} = 5\%$.
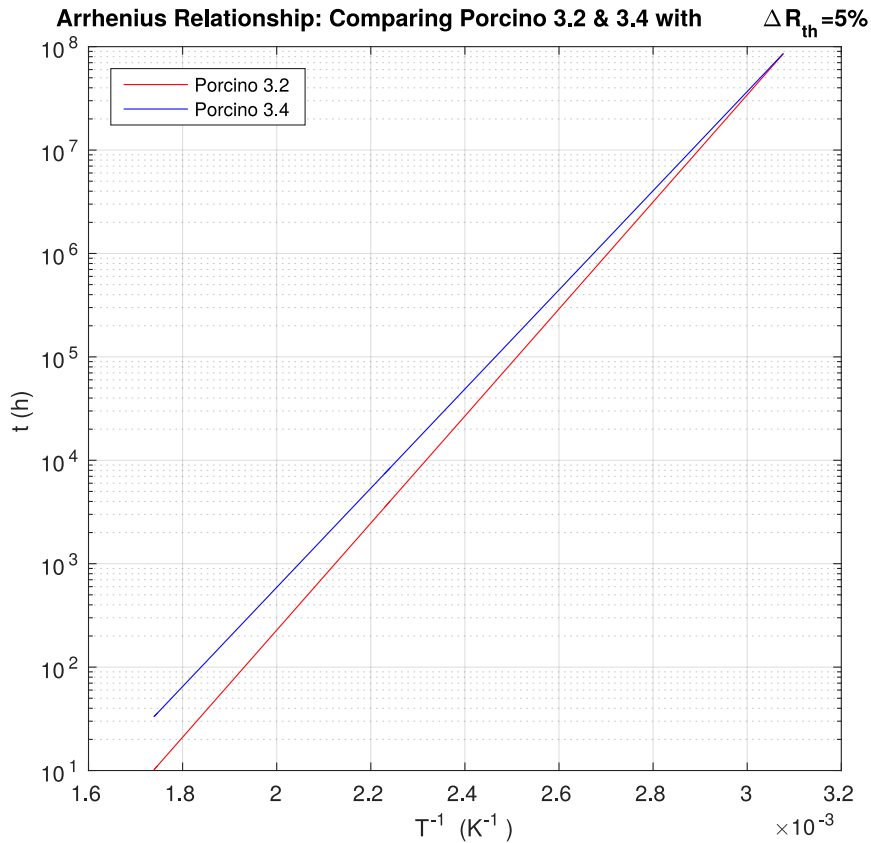
Figure 5.22: In figure is reported a comparison between the MTTF ($F(t) = 50\%$) of Porcino 3.2 and 3.4 at different coil temperatures. As noticeable, their values converge at low temperatures and diverge at higher ones.

In case of Porcino 3.4, a threshold failure condition $\Delta R_{th} = 10\%$ was too high, and not enough failures of TVs occurred to be able to construct a significant statistical model. For this reason, $\Delta R_{th} = 10\%$ was considered as a quite safe threshold for currents below 220mA, and a new limit of $\Delta R_{th} = 5\%$ was set to be more conservative and being able to build the model.

Also in this case, log-normal failure distribution was confirmed as the one best describing experimental data, and the same procedure described from sections 5.1.3.1 to 5.1.3.3 has been used.

In the end, this model seems to describe quite well the failure probability in time at different temperatures also for Porcino 3.4 (see results in Fig. 5.21). Furthermore, comparing results with those of Porcino 3.2 (with $\Delta R_{th} = 5\%$), a different trend of $MTTF$ has been found between the two versions, according to what was experimentally seen (see Fig. 5.22). In particular, the model predicts that at higher temperatures (and so at higher currents), Porcino 3.4 should be more resistant than Porcino 3.2, but, as temperatures get lower, this difference in behavior becomes more and more irrelevant, as the comfort zone is reached for both the versions of the device.

Listing 1: Likelihood function maximization considering an Arrhenius-like relationship of μ and σ.

```matlab
%% DATA LOADING
data=dlmread('Temperature_and_TTF.csv');
T=data(:,1);       %temperatures vector
t=data(:,2);       %TTF vector
i2=data(:,4);      %index for survived devices (1 or 0)

%% MLE: variable Sigma
t1=log(t);%time
T1=T;%temperature
fun=@(x) log(prod(normpdf(t1(i2==0),x(1)+x(2)./T1(i2==0),x(3)+x
    (4)./T1(i2==0)))*prod((1-i2.*normcdf(t1,x(1)+x(2)./T1,x(3)+x
    (4)./T1))));  %Likelihood function

x0=[-17.53 11458.82 1 -5];  %trial parameters (mu_0, mu_1,
%sigma_0, sigma_1)
x=fminsearch(fun,x0);          %Likelihood function maximization

R=x./x0;

while R(1) & R(2) & R(3) & R(4) ~= 1
x0=x;
x=fminsearch(fun,x0);
R=x./x0;

end

```

5.2 Failures in Humid Environment

According to information reported in section 4.2.3.4, a failure mode discovered for Porcino is the breakage of the fast-axis (FA) spring when the device is actuated only on the FA in presence of humidity ($T = 85°C$, $RH = 85\%$), as reported in Fig. 5.23. The test has been carried out at different mechanical stress levels (different operating angles) and a trend has been found that suggests a phenomenon similar to fatigue, as more MEMS failed at higher stress levels and their life has also been shortened.
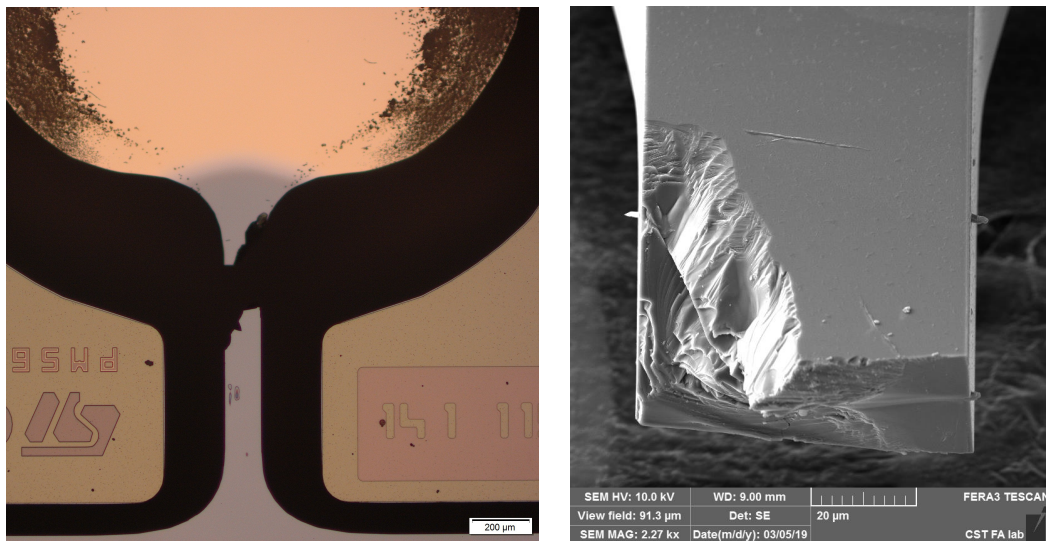
Figure 5.23: In figure are reported two pictures of the typical FA spring breakage, one taken with an optical microscope, and the other with a SEM.

5.2.1 Theories About This Mechanism

As FA spring of Porcino is entirely made by mono-crystalline silicon, its behavior during mono-axial life test in humid environment is quite unusual. Indeed, as reported in literature, silicon is a brittle material that doesn't exhibit any dislocation activity at low homologous temperatures, any extrinsic toughening mechanisms, or any evidence of susceptibility to environmentally induced cracking in moist air or in wet. Thus, on the base of this information, silicon should not fatigue in air at room temperature, and indeed there has been no evidence up to date of bulk silicon being susceptible to fatigue failure.

However, according to what was found in literature [28–38, 49–58], there's a strong evidence that silicon can suffer from fatigue phenomena at the micronscale, especially when samples are exposed to humidity. Indeed, as reported in many studies cited above, after fatigue lives exceeding 10^{11} cycles, both poly and mono-crystalline silicon shows failure stresses which are approximately half their single-cycle fracture strength [30, 31].

It must also be remarked that *Si* in presence of air is always covered by a thin native oxide layer (SiO_2), which, other than having an amorphous structure with

(a) Formation of wedges and "cantilever effect".

(b) Wear debris effect.
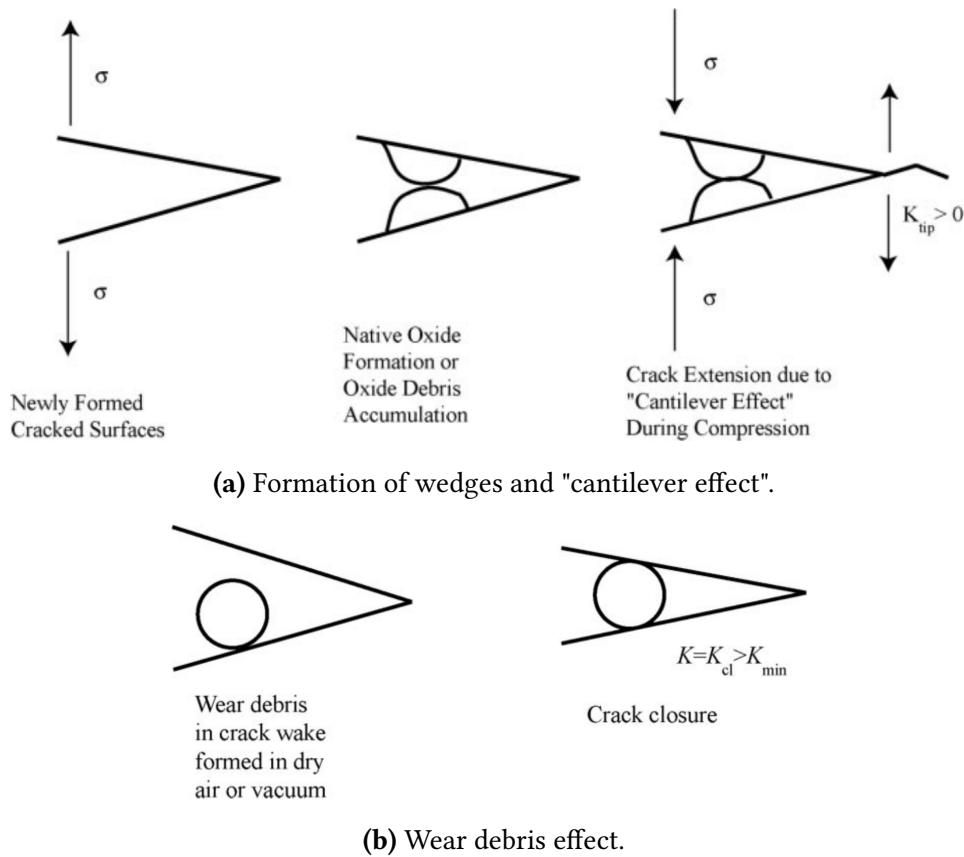
Figure 5.24: In figure are reported the main factors affecting the theory of mechanically induced subcritical cracking. Adapted from [49]

respect to silicon, could also undergo different reactions in presence of humidity (see section 5.2.1.2), and this could be the origin for crack initiation and propagation within FA spring.

From studies reported above, two main theories to describe the fatigue mechanism in micron-scale silicon have been considered: one that attributes its origin only to mechanical stress ("mechanically induced subcritical cracking" by *Kahn et al. [57, 58]*), and one that instead considers stress-corrosion cracking phenomena (SCC) ("reaction-layer fatigue" by *Muhlstein et al.* [54–56]).

5.2.1.1 Mechanically Induced Subcritical Cracking

The mechanically induced subcritical cracking model [57, 58] states that subcritical cracking occurs in the silicon itself when subjected to cyclic loads, in particular when cyclic loads with large compressive components are present.
To account for environmental effects, *Kahn et al.* postulated that thikened surface oxide on newly formed crack surfaces in air can cause wedging effects. In particular, asperities which generate on notches surfaces can come in contact during the compressive cycles, acting as wedges to create areas of local tension and additional subcritical cracking ("cantilever effect", see Fig. 5.24a).

106

An alternative hypothesis about effects of humidity is that increasing relative humidity in operating air greatly reduces the amount of wear debris formed by contacting poly-silicon components, which in fatigue life of bulk ceramics decrease crack growth by preventing crack closure and reducing the effective driving force for crack propagation (see Fig. 5.24b).

Thus, the theory proposed by *Kahn et al.* doesn't consider any corrosion phenomena for this failure mechanism.

However, in many studies found in literature there is no evidence for this type of fatigue mechanism, indeed, *Budnitzki et al.*[35] claims that the wedging effect should be associated with nanoscale debris visible through high resolution SEM, and that they failed to observe them in any of their tests. Moreover, they sustain also that the enhancement of crack driving force in presence of wedges is an incorrect notion.

For these reasons, other failure mechanisms able to better justify the influence of an harsh environment on fatigue life of silicon have been considered, among which the "reaction layer fatigue" presented in section 5.2.1.2.

5.2.1.2 Reaction Layer Fatigue

As already said, silicon in presence of air is always covered by a thin native oxide layer, that is known to suffer from phenomena like stress corrosion cracking (SCC), in which, under tensile stress conditions, small cracks can initiate and propagate due to hydrolysis of the native oxide layer in environments which contain water (also in vapor phase). These cracks tend to initiate in correspondence of pre-existing flaws, which can have many origins, e.g. in the case of Porcino process flow during FA spring silicon dry etch step. The hydrolysis process of SiO_2 is well described in [36–38], and showed in Fig. 5.25.

The crack propagation velocity (v) as a function of the applied stress intensity factor (K_I) generally presents three characteristic regions, as reported in Fig. 5.26 [59]:

1. *Region I* corresponds to *stress-corrosion regime*. Here the crack propagation speed is a strongly increasing function of the stress intensity factor, it has an almost linear dependence on humidity in moist air and it increases with temperature. These dependencies are generally described by Wiederhorn equation:

$$v^I = v_0 \exp(\alpha K) = A \left(\frac{p_{H_2O}}{p_0} \right)^m \exp \left(-\frac{\Delta E_a - bK}{RT} \right) \tag{5.35}$$

   where p_{H_2O} is the partial pressure of the vapor phase in the atmosphere, p_0 is the total atmospheric pressure, R the gas constant and $A, m, \Delta E_a, b$ are four adjustable parameters that take into account the dependence on the glass composition.

2. *Region II* represents the *transport limited propagation*. In this region the crack propagation velocity is substantially independent from the stress intensity factor, since the reaction rate is limited by the transport kinetics of
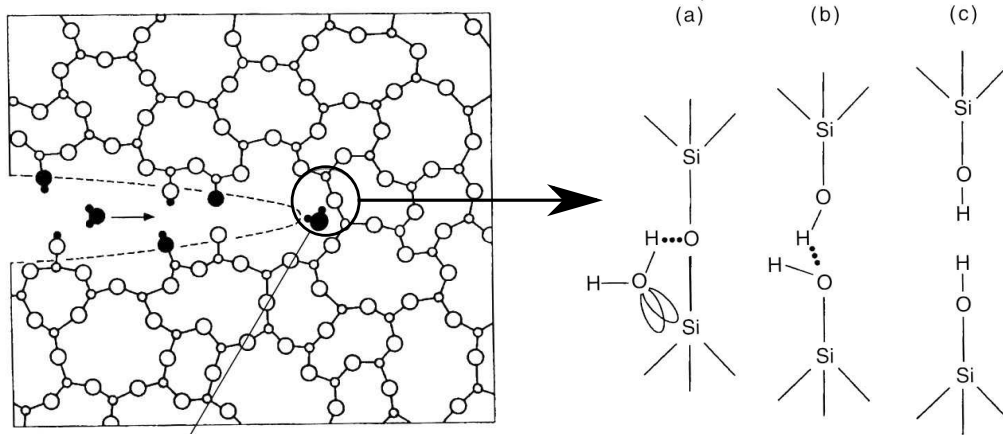
Figure 5.25: In figure is reported the process of hydrolysis of SiO_2 in presence of water and tensile mechanical stress. Adapted from [59].

reactive molecules towards the crack tip. The plateau value for propagation in moist air increases with humidity, according to the equation reported below:

$$v^{II} = v_0 p_{H_2O} D_{H_2O} \qquad (5.36)$$

where D_{H_2O} is the diffusion coefficient of water molecules in air.

3. *Region III* corresponds to *inert propagation and failure.* Here crack propagation speed starts increasing again with K, and the dependence is so strong that its measurement require special techniques. The position of region III is substantially independent of the local environment, in agreement with the expected suppression of the stress-corrosion reactions.

In this regard, another theory on this degradation mechanism has been proposed by *Muhlstein et al.*, which they called *reaction-layer fatigue* (see Fig. 5.27), and can be described as follows. They hypothesize that fatigue of silicon thin films occurs through a process of sequential, mechanically induced oxidation and environmentally assisted cracking of the surface layer of material that forms upon reaction with the atmosphere (e.g. the SiO_2 native oxide). Indeed, *Mulchstein et al.* noticed that during subsequent fatigue loading, the oxide at the root of a pre-existing notch thickened significantly. Moreover, the heat dissipation during mechanical stress was very low ($\Delta T \sim 1°C$), thus, the hypothesis is that the origin of cyclic oxide thickening process is purely mechanical. Indeed, stress, in particular of tensile nature, seems to be a key parameter for silicon oxidation kinetics. The deformation undergone by the SiO_2 reaction layer and the associated strain energy are enough to modify the diffusivity of oxygen and water and the kinetics of the reaction at the interface. Cracks are then initiated in the thickened amorphous layer, assisted by the already mentioned vulnerability of amorphous SiO_2 to SCC. This process goes on through the propagation of these cracks by successive oxidation and environmentally assisted cracking of the reaction layer, until a critical crack size is reached and failure occurs in the underlying silicon structure (see Fig. 5.27).
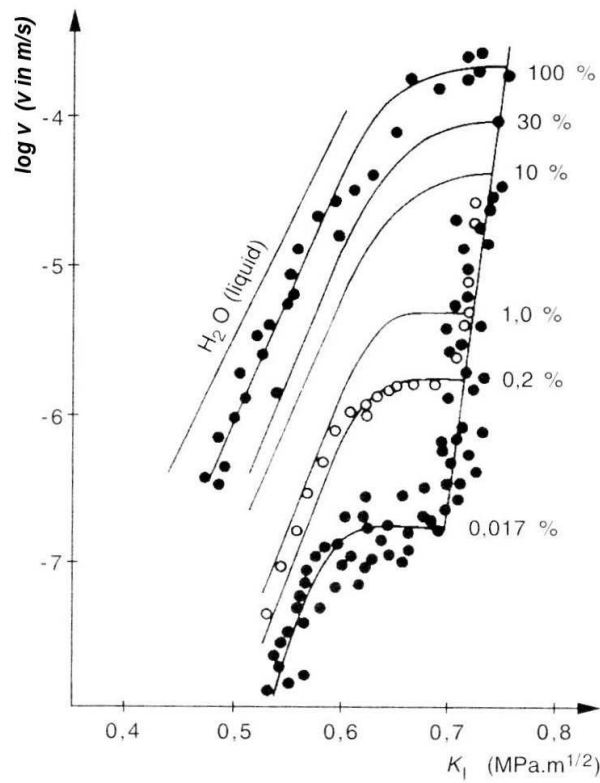
Figure 5.26: In figure is reported a graph showing the dependency of crack propagation velocity from stress intensity factor at different levels of relative humidity. Adapted from [59].
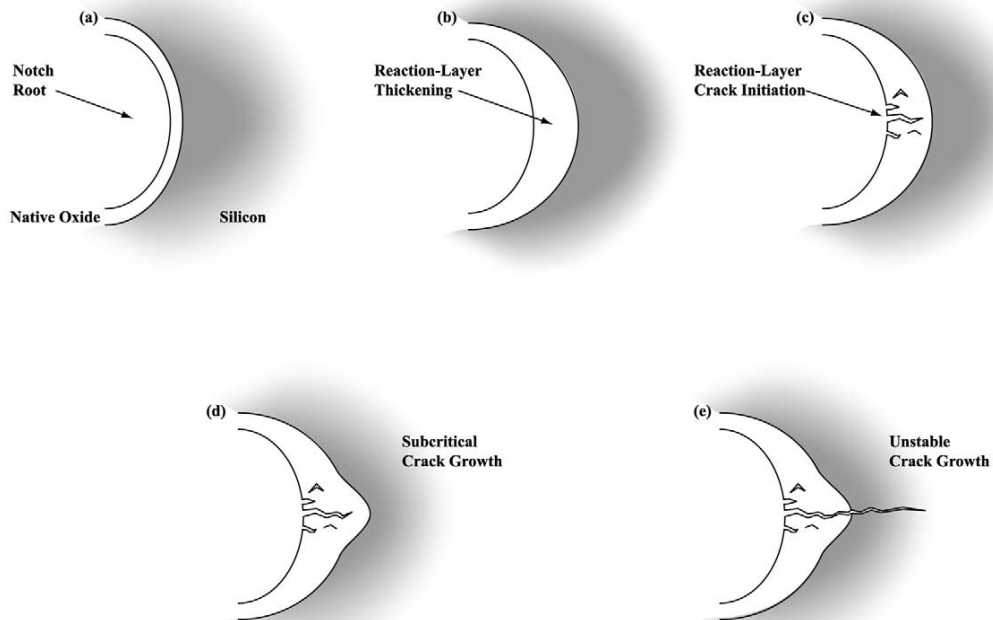
Figure 5.27: In figure is reported a representation of the crack growth mechanism through silicon oxide layer, typical of the so called "reaction layer fatigue". Adapted from [55].

5.2.2 Experimental Activities and Modeling

Regarding which is the mechanism that best describe the behavior of silicon under fatigue in humid environment, in literature the most accredited one seems to be the "reaction layer fatigue". However, even if in agreement with customer the decision was to solve this issue at their side by modifications at package level, it was also decided to internally study the fatigue life of Porcino in harsh environment.

Thus, a new test matrix has been prepared, which covers an operative window significant for the application of Porcino. In particular, it was decided to keep a fixed temperature of 85°C in order to accelerate the test, and to variate operating mechanical angle between 12.5° and 15°, and relative humidity (*RH*) level between 30% and 85%, according to what reported in Tab. 5.3. The mirror was actuated only on the FA, in order to generate less heat due to power dissipation and thus avoiding to have locally a too low relative humidity (different with respect to that set in the oven), not significant for the test itself. Tests have been performed in a climate chamber *WK11-340/40*, and each of them has been designed for a duration of 1000h, with readouts scheduled at 168h, 336h, 500h and 1000h.

A monitoring system was also set up in order to have real-time information about FA frequency and FA opening angle. Moreover, at every readout all the parameters have been measured (see Tab. 4.3 reported in section 4.2) in order to investigate if some drifts could correlate with any sign of degradation in the MEMS. One of the most interesting parameter for these tests was certainly the time to failure (*TTF*) of devices, which was collected thanks to the monitoring system itself.

No drifts in parameters have been found that could correlate with a degradation of the FA spring. According to what found in literature, a progressive decrease in resonance frequency (f_0) was expected, which would be related to a continuous loss in stiffness due to cracks propagating in the spring. However, none of this has been found, probably due to the fact that the monitoring system has a too low resolution to record these quick resonance frequency variations, or maybe because, unlikely studies done on samples made ad hoc, Porcino wasn't pre-notched, and so its f_0 may be less sensitive to *RH* variations.

The aim of this activity was to find a way to physically describe the phenomenon, in order to be able to approximately predict Porcino fatigue life in the investigated operating window. The expectation was that higher humidity levels should correspond to more severe operating conditions for devices, thus reducing their fatigue life. Obviously, results showed below are valid only for Porcino, but future activities will consist in completing this study with the development of a generalized model valid also for other type of actuators (or at least for other families of micromirrors).

Once data have been collected for all of the testing conditions mentioned above, they have been fitted both in a linear and a quadratic way with respect to mechanical stress and humidity level, in order to have two different levels of approximation and being able to choose the best one. This has been done through a

Table 5.3: In table is reported the test matrix used to study the failure of Porcino during fatigue in humid environment.

Mech. Angle\RH%	30%	60%	85%
12.5°	X	X	X
14°	X	X	X
15°	X	X	X

script developed on Python and reported in Listing 2, and by using the two general equation reported below (where x represent the mechanical angle and y the relative humidity):

- Linear equation (with parameters a, b, c):

$$TTF = ax + b\,y + c \tag{5.37}$$

- Quadratic equation (with parameters a, b, c, d, e, q):

$$TTF = ax + by + cxy + dx^2 + ey^2 + q \tag{5.38}$$

As noticeable in Listing 2, data have been imported and a grid for the fitting has been created. Then, the coefficients for both linear and quadratic equations have been estimated and used to re-calculate the time to failure on the grid. Finally, the coefficient of determination R^2 has been calculated for the two fittings in order to establish which is the best one to describe fatigue in presence of humidity.

Listing 2: Fitting of experimental data through a linear and a quadratic relationship.

```
1  #%% Import data
2  import csv
3  import numpy as np
4  import scipy.linalg
5  from mpl_toolkits.mplot3d import Axes3D
6  import matplotlib.pyplot as plt
7  import pandas as pd
8  from matplotlib import cm
9
10
11  # x = angles
12  # y = RH
13  # z = TTF
14
15  data = np.c_[x,y,z]
16
17  #Grid
18  mn = np.min(data, axis=0)
19  mx = np.max(data, axis=0)
20  X,Y = np.meshgrid(np.linspace(mn[0], mx[0], 18), np.linspace(mn
       [1], mx[1], 18))
21  XX = X.flatten()
22  YY = Y.flatten()
23
```

```python
24 #%% Fitting
25 k=2
26 a = np.array([angles])
27 b = np.array([RH])
28 c = np.array([TTF])
29 n=len(c)
30
31 for order in [1,2]:# 1: linear, 2: quadratic
32
33 if order == 1: #best−fit linear plane
34 A = np.c_[data[:,0], data[:,1], np.ones(data.shape[0])]
35 #Coefficients estimate
36 C_linear,_,_,_ = scipy.linalg.lstsq(A, data[:,2])
37 #Evaluate TTF on grid
38 Z_linear = C_linear[0]*X + C_linear[1]*Y + C_linear[2]
39
40 #Model results
41 Zhat = C_linear[0]*a + C_linear[1]*b + C_linear[2]
42 #Mean of experimental results
43 Zbar = np.sum(c)/n
44 #Explained sum of squares (devianza spiegata dal modello)
45 ESS = np.sum((Zhat−Zbar)**2)
46 #Total sum of squares (devianza totale)
47 TSS = np.sum((c − Zbar)**2)
48 #Residual sum of squares (devianza residua)
49 RSS = np.sum((c − Zhat)**2)
50 #Coefficient of determination (linear)
51 Rsquared_linear = ESS/TSS
52
53 elif order == 2: #best−fit quadratic curve
54 A = np.c_[np.ones(data.shape[0]), data[:,:2], np.prod(data[:,:2],
       axis=1), data[:,:2]**2]
55 #Coefficients estimate
56 C_quadratic,_,_,_ = scipy.linalg.lstsq(A, data[:,2])
57 #Evaluate TTF on grid
58 Z_quadratic = np.dot(np.c_[np.ones(XX.shape), XX, YY, XX*YY, XX
     **2, YY**2], C_quadratic).reshape(X.shape)
59
60 #Model results
61 Zhat = np.dot(np.c_[np.ones(a.shape), a, b, a*b, a**2, b**2],
     C_quadratic).reshape(a.shape)
62 #Mean of experimental results
63 Zbar = np.sum(c)/n
64 #Explained sum of squares (devianza spiegata dal modello)
65 ESS = np.sum((Zhat−Zbar)**2)
66 #Total sum of squares (devianza totale)
67 TSS = np.sum((c − Zbar)**2)
68 #Residual sum of squares (devianza residua)
69 RSS = np.sum((c − Zhat)**2)
70 #Coefficient of determination (quadratic)
71 Rsquared_quadratic = 1−((RSS / TSS)*((n−1) / (n−k−1)))
```
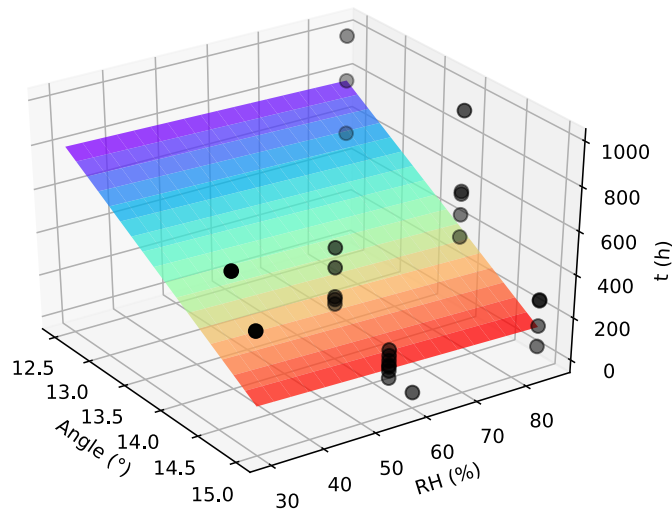
(a) Linear fitting, $R^2 \simeq 0.45$
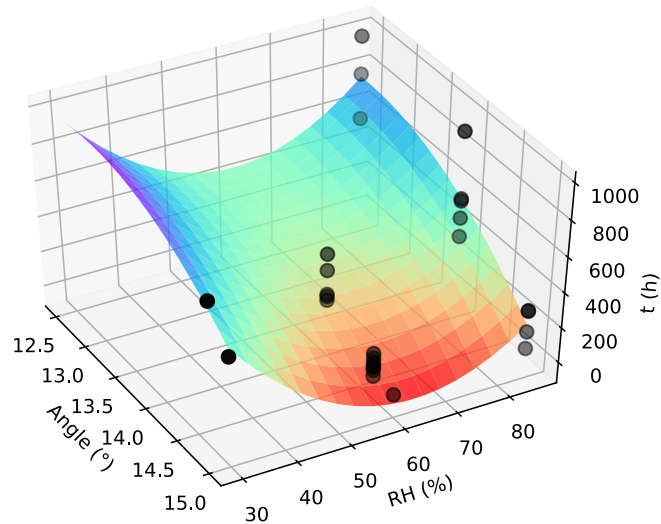
(b) Quadratic fitting, $R^2 \simeq 0.80$

Figure 5.28: In figure are reported two fitting curves for the failures in humid environment, one linear and one quadratic.

As noticeable from Fig. 5.28, the linear equation didn't lead to great results, while in first approximation the quadratic one gives a decent fitting of experimental data ($R^2 \simeq 0.80$).

What emerged from this activity is that the failure rate of Porcino tends to increase at high levels of relative humidity and its time to failure becomes lower.

Anyway, as noticeable from Fig. 5.28b, it has been also found that the intermediate condition ($T = 85°C$ and $RH = 60\%$) should be more aggressive for Porcino than the one at $RH = 85\%$ (which was hypothesized to be the most critical one). This result seems quite unreasonable, also considering what found in literature. One hypothesis is related to the fact that the test at $T = 85°C$ and $RH = 85\%$ was conducted before those at $RH = 30 - 60\%$, by means of a different experimental setup. This could have affected results of the test itself and thus, another run at this stressing condition will be done to confirm or reject the results shown in

Fig. 5.28. In particular, the hypothesis is that there was a misalignment between the two different set-up, and it seems quite reasonable that the real values of times to failure slightly decrease after the condition at $RH = 60\%$, or at most that the curve reaches a plateau between the conditions at $RH = 60\%$ and $RH = 85\%$ (as reported only at a representative level in Fig. 5.29).

If the current trend will be confirmed after the retest, it means that the activation energy of this peculiar failure mechanism actually reaches a minimum at a level of relative humidity close to 60%, and thus an explanation for this discovery should be found through a deep study.

In any case, humidity associated with mechanical stresses of a certain level seems to have a big impact on this particular failure mode, as can be noticed by the trend in Fig. 5.28.
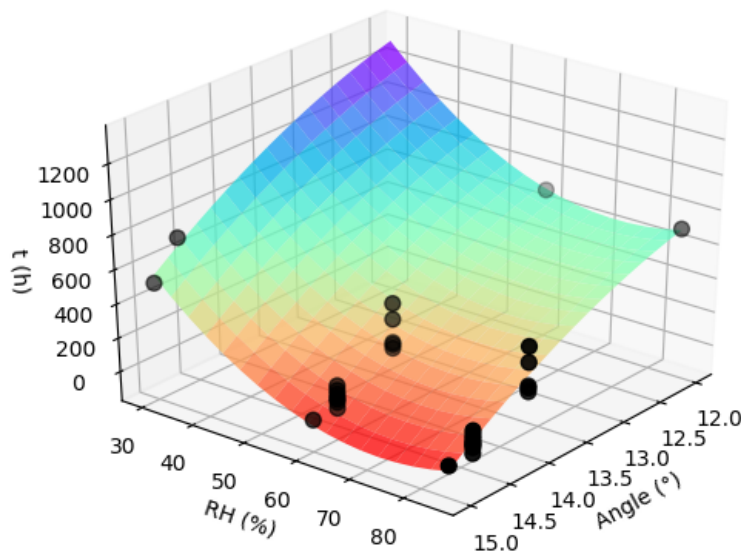
Figure 5.29: In figure is reported an image to show the expected behavior of Porcino for what concern failure in humid environment. In particular, failure rate should increase at higher values of RH. This is a qualitative representation, not based on real data.

After data collection and preliminary processing, the next step, as already done for copper coil oxidation, was their statistical treatment.

Considering the fatigue mechanism involved in this phenomenon, one among log-normal and Weibull distribution should be the suitable function to describe experimental data. In Fig. 5.30 is reported an example (at $RH = 60\%$ and 15°) showing that the best data fit is given by log-normal distribution ($R^2_{Weib} = 0.72$ while $R^2_{Logn} = 0.84$). In theory, as crack initiation could be related to the presence of some flaws in the SiO_2 layer, Weibull distribution should be the best one to describe collected data. However, considering the combination between chemical and mechanical contribution to the crack propagation (stress-corrosion cracking), log-normal distribution could actually be the best choice, as the most suitable to describe these kind of degradation phenomena.

As for the study of coil oxidation, when enough experimental data will be available, the Maximum Likelihood Estimation method will be used to take into ac-
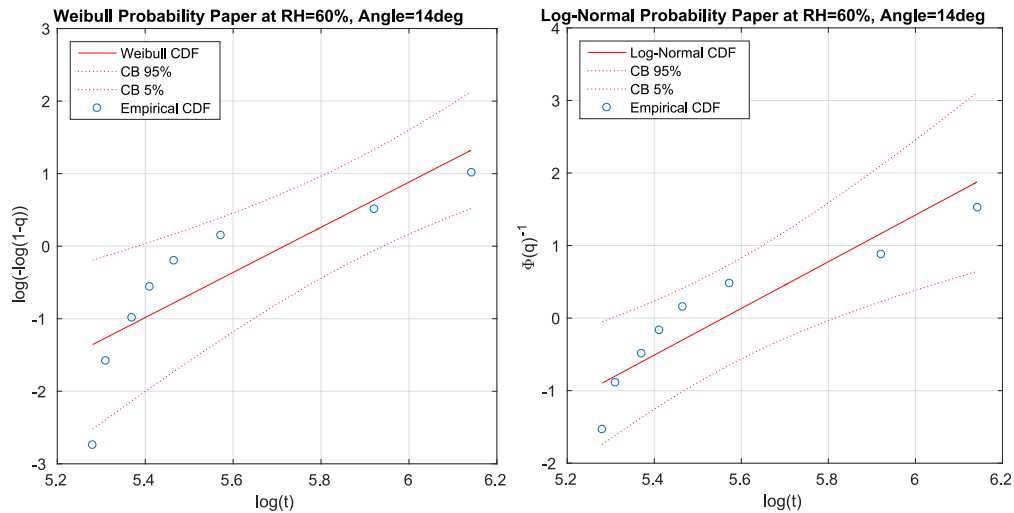
Figure 5.30: In figure is reported a comparison between Weibull and lognormal probability plots. In particular $R^2_{Weib} = 0.72$ while $R^2_{Logn} = 0.84$, and thus means that lognormal distribution should be the best one to describe this phenomenon (this can be explained not only mathematically, but also in a physical way, see section 5.2.2).

count not only the failed devices, but also the survived ones (see section 5.1.3.2). In this way, the estimated TTF will be much more realistic and could be used to predict the actual life of Porcino under different operating conditions within the tested window ($RH = 30 - 85\%, \theta = 12.5° - 15°, T = 85°C$). Parameters found through the quadratic fitting will be used in first approximation as starting values for the maximization of the likelihood function. Thanks to this procedures the optimal values of the parameters to fit experimental data will be found, and TTF would be predicted beyond the actual testing time also for conditions different from those of the tests. This will be done through a *MATLAB* code similar to that used in section 5.1.3.3, and reported in Listing 3.

Listing 3: Likelihood function maximization considering a quadratic relationship for μ and σ.

```matlab
%% DATA LOADING
data=dlmread('Data.csv');
RH=data(:,1);        %relative humidity vector
angle=data(:,2);     %mechanical angle
t=data(:,3);      %TTF vector
i2=data(:,4);        %index for survived devices (1 or 0)

%% MLE: Constant Sigma
fun=@(x) -log(prod(normpdf(t(i2==0),x(1)+x(2).*angle(i2==0)+x(3)
    .*RH(i2==0)+x(4).*angle(i2==0).*RH(i2==0)+x(5).*angle(i2==0).*
    angle(i2==0)+x(6).*RH(i2==0).*RH(i2==0),x(7))).*prod((1-
    normcdf(t(i2==1),x(1)+x(2).*angle(i2==1)+x(3).*RH(i2==1)+x(4)
    .*angle(i2==1).*RH(i2==1)+x(5).*angle(i2==1).*angle(i2==1)+x
    (6).*RH(i2==1).*RH(i2==1),x(7)))));
%MLE method
x0=[-14502.6 2575.43 -47.39 -1.33909 -97.8798 0.528518 400];
x=fminsearch(fun,x0);

R=x./x0;
```

115

```
15
16  while R(1) & R(2) & R(3) & R(4) & R(5) & R(6) & R(7) ~= 1
17    x0=x;
18    x=fminsearch(fun,x0);
19    R=x./x0;
20  end
```

In first approximation the current analysis is good enough to give an idea of the behavior of Porcino when working in these particular conditions, but a new, more accurate, relationship should be found to describe the acceleration factor of this degradation phenomenon. Moreover, as reported above the plan for the future will be to develop a general model, valid for a wider family of devices.

5.2.3 Summary and Future Perspectives

Looking at trends found through this activity for Porcino, and from the consensus obtained in literature by the studies of *Muhlstein et al.*, it seems reasonable to support the hypothesis of "reaction layer fatigue". Indeed, humidity appears to be a key parameter for the type of failure found on Porcino, and *Kahn et al.*'s theory apparently does not give enough importance to this factor.

Although, as mentioned above, it was decided to solve this problem at package level by the customer, at ST side, in order to study more deeply this phenomenon, a collaboration with the department of *Chemistry, Materials and Chemical Engineering "GIULIO NATTA"* of *Politecnico di Milano* has been started. In particular, to understand better the nature of crack initiation and propagation, a series of analyses (XRD, Raman spectroscopy, TEM) has been organized on stressed and pristine devices to find some measurable quantities which would allow to investigate the different cracks stages. Furthermore, trying to find a solution at MEMS level to fix the problem, it was decided to deposit a layer of self assembled monolayer (SAM) on the affected area, whose precursor is the trichlorosilane (FOTS) (see Fig. 5.31). These materials are known to be hydrophobic [60–62], and thus, if the degradation mechanism is actually the "reaction layer fatigue", the functionalization of the FA spring surfaces should prevent its breakage, or at least it should highly reduce the failure rate.

The process used was customized for Porcino but it wasn't yet optimized, so improvement will be done in the future to reach better, more reliable results. In any case, the deposition was done by vapor phase directly on the MEMS at *Politecnico di Milano*. The set up consisted of two connected vessels (that can be isolated through a valve), a vacuum pump and a heating system. The deposition process is explained in the following. First of all, the SAM precursor is placed in one vessel (VESSEL-1), while the samples of Porcino to be treated in the other one (VESSEL-2), where a certain level of vacuum is created. Then VESSEL-1 is heated at 250°C for 2 min, after which the valve is opened and the reactant flows toward VESSEL-2 thanks to the depression previously created. At this point the two vessels are cooled down and the treated samples are left in open air for a few hours to complete the reaction.

116
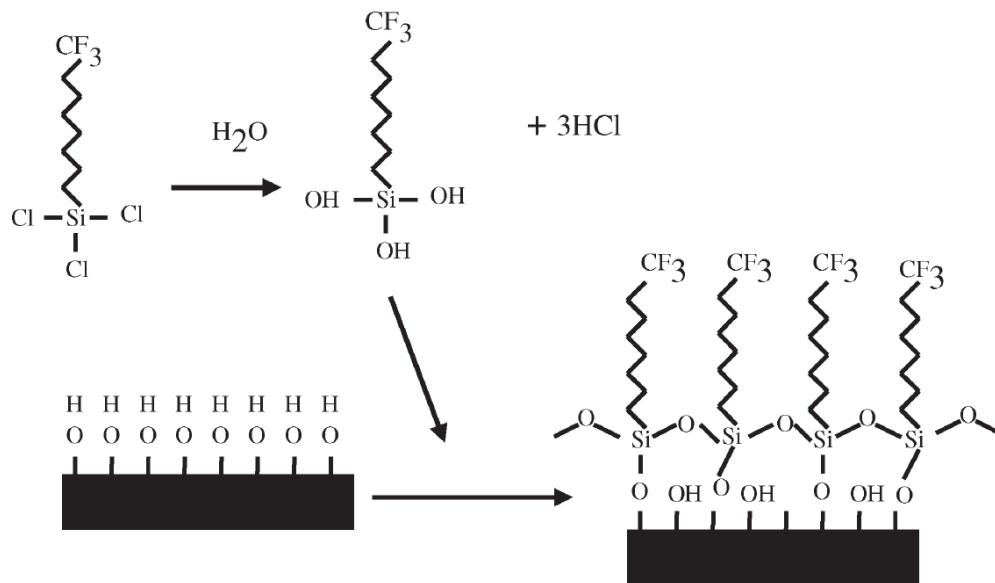
Figure 5.31: In figure is reported a representation of the precursor (FOTS) and the deposition of the self-assembled monolayer silanes. Adapted from [61].

The test matrix reported in Tab. 5.3 will be applied also for the devices treated with SAM. For the moment, a sample actuated at 14° have been put under testing at $T = 85°C$ and $RH = 60\%$, and up to now (250h of test) there were no failures. In any case, for untreated devices the typical TTF was found to be around $170-450h$, thus more time is required to assess if this treatment may actually be a solution for the problem, or if at least it could slow it down.

Furthermore, more samples should also be tested to be confident about the result as, from a statistical point of view, the device under testing may be simply out of the failures distribution of Porcino and the achievement could be actually not related to the treatment performed but on the casualty of taking a MEMS more robust than others even before treatments.

Conclusions and Future Activities

During this thesis work the reliability activity of an electromagnetic micro-mirror, called Porcino due to its mushroom-like structure, was followed and taken to the final stages.

The device was subjected to different types of tests, which were significant for its application and life: mechanical tests (shocks and vibrations), unpowered tests (low-temperature storage, temperature-humidity storage, thermal cycles, electrostatic discharge) and powered tests (life tests in dry and humid environment, static DC test and power On-Off). Porcino showed no failures or problems during mechanical and unpowered tests, while two failure modes were discovered during powered ones. More in detail, important problems have been found during static DC test and life test in humid environment.

For what concerns failure during DC test, they were related to power dissipation of the MEMS caused by the high driving currents flowing inside a copper coil, which presents a certain value of driving resistance. The heat generated by Joule effect favors the progressive oxidation of the copper coil, which in turn causes the power dissipation to increase, in a vicious circle. Briefly, up to version 3.2, in a relatively short period of time, Porcino reached a resistance drift that was too high for the customer to use it in the application ($\Delta R/R_0 = 10\%$), and sometimes it also failed catastrophically due to the complete degradation of the contact via below the coil (thermal runaway). The problem was solved at design level with the introduction of version 3.4. Indeed, the thickness of the copper coil has been increased by 5µm, allowing the flowing of higher currents, or, on the other hand, to dissipate less heat at fixed current. Furthermore, a physical model able to describe *Cu* oxidation as function of temperature (related to power dissipation) has been created. Finally, starting from data collected during reliability test matrix, a predictive statistical model has also been developed and validated, which well describe behavior and failure rate of Porcino under these kind of stressing conditions. Thanks to this model it is possible to predict time to failure of the device for coil temperatures different from those of testing (and thus for different driving currents, which are related to temperature through power dissipation). More in details the approach can be summarized as follows. Starting from collected times to failure (TTF), the failure distribution (among those used in reliability field to describe failure phenomena) that best describes experimental data has

been found, which turned out to be the log-normal one[1]. After that, assuming that TTF follows an Arrhenius-like relationship and that log-normal distribution is the best one to describe the phenomenon, by using a statistical method called Maximum Likelihood Estimation (MLE), the predictive model mentioned above was derived. As already said, this allows to calculate the TTF at conditions different from those of testing; e.g. in operative conditions for application of Porcino ($T = 60°C$, $i \simeq 150$mA and mechanical angles $14° \times 18°$) TTF is predicted to be $\simeq 10^6$h for this failure mode, which is considered to be very safe.

Regarding failures that have been found due to fatigue in humid environments, the mechanism is still not entirely clear. Several theories have been examined, starting from those for which the phenomenon should only have a mechanical origin, up to those that suggest stress-corrosion mechanisms. What seemed to be the most exhaustive one is the so-called "reaction layer fatigue" by *Muhlstein et. al*[54–56], according to which a cyclic mechanical stress would favor the growth of the native oxide in correspondence of a flaw, within which, in presence of humidity, cracks may propagate due to stress-corrosion phenomena. In the case of Porcino, failures were all catastrophic and affected the majority of devices. Considering that studies found in literature are all related to samples made ad hoc to study this phenomenon, up to now for Porcino, that is a custom device, it wasn't feasible to derive a law that could describe in an exhaustive way the fatigue effect in harsh environment of the silicon spring. For this reason, up to this point, the only thing that was possible to do consisted in setting up a series of experiments combining different levels of relative humidity and fatigue stress to obtain a fitting curve able to approximately describe the phenomenon. As for copper coil oxidation, a failure distribution to statistically describe experimental data has been found. In this case, Weibull and log-normal were the suitable distribution, as both of them well describe cyclic fatigue. However, considering that in this case degradation is not just related to mechanical fatigue, but also to chemical reactions occurring in presence of humidity within the native oxide layer on silicon surface, the log-normal distribution turned out to be the best choice. To solve this issue, the solution agreed with the customer was the design of a completely hermetic package. In any case, more innovative solutions acting directly on the MEMS itself have also been taken into account, for example the deposition of hydrophobic self-assembled monolayers (SAM), whose study is being carried out in collaboration with the department of *Chemistry, Materials and Chemical Engineering "GIULIO NATTA"* of *Politecnico di Milano*.

Future activities include the development of a physical model able to describe the behavior of Porcino for fatigue in humid environment. Furthermore, a definitive solution able to prevent this kind of failure at MEMS level should be found. Moreover all the models cited above should be generalized in order to make them viable also for other families of actuators, or at least for a wider range of micro-mirrors.

---

[1]Log-normal distribution usually describes quite well degradation phenomena like fatigue, oxidation, corrosion, etc. . .

Appendices

Statistics and Failure Distributions

In this appendix, the basic concepts of statistics will be presented, as well as the main statistical distributions typically used in reliability, according to [19–21].

A.1 Basics of Statistical Analysis

In statistics the process of random extraction of a sample of data from a population of data is called sampling. An event is instead defined as the possible result of an experiment. Y is the random variable that represents the possible result of the experiment, while y is the observed value, which is the result obtained from a single experiment (obviously $y \in Y$).
Random variables are of two types:

- discrete random variables if they assume discrete values in the field of existence;

- continuous random variables if they assume any real value in their field of existence.

Probability is a concept used to define the possibility of an event happening, and is related to the hypothesis of repetition of the event itself. Suppose it is possible to repeat infinite times the experiment described by the random variable Y. Let $(y_1, y_2, \dots)$ be the sequence of values contained in Υ that describes the results of the single experiments and let A be a subset of Υ. Then it is possible to define:

$$Prob(A) = \lim_{n \to \infty} \frac{n_A \{i \in (1, \dots, n) : y_i \in A\}}{n} \tag{A.1}$$

Obviously, the problem is being able to describe the tendency of experimental results to distribute, or the probability of occurrence of an event, having only a limited set of data (n).

A.1.1 Probability Density, Cumulative Probability, Reliability Functions and Failure Rate

Let Y be a continuous random variable and $y \in Y$. It is possible to define a probability density function:

$$f(y) = \lim_{\Delta \to 0} \frac{Prob(Y \in (y, y + \Delta))}{\Delta} \tag{A.2}$$

If $\Delta = dy$ is an infinitesimal increment, then it is possible to interpret the probability density function as the probability of finding Y in the range of observable values $(y, y + dy]$, ie:

$$Prob(y \leq Y \leq y + dy) = f(y)dy \tag{A.3}$$

The cumulative probability function is, instead, the probability that the random variable Y is lower than the argument value y:

$$F(y) = Prob(Y \leq y) = \int_{inf\Upsilon}^{y} f(y)dy \tag{A.4}$$

Obviously, the following equation is valid:

$$F(sup\Upsilon) = \int_{\Upsilon} f(y)dy = 1 \tag{A.5}$$

If instead Y is a discrete random variable with $\Upsilon = \{y_1, y_2, \dots\}$, a probability mass function is defined as:

$$p(y_i) = Prob(Y = y_i) \tag{A.6}$$

In this case, the cumulative probability function is simply:

$$F(y) = Prob(Y \leq y) = \sum_{i:y_i \leq y} Prob(Y = y_i) = \sum_{i:y_i \leq y} p(y_i) \tag{A.7}$$

From the previous definitions, it follows that the probability of finding the random variable Y in the interval $(a, b]$ is:

$$Prob(a < Y \leq b) = Prob(Y \leq b) - Prob(Y \leq a) = F(b) - F(a) \tag{A.8}$$

The percentile of order $p \cdot 100\%$ of the population Y is defined as the argument value y_p which corresponds to a cumulative probability p, ie y_p is such that:

$$Prob(Y \leq y_p) = p \tag{A.9}$$

Reliability is the complementary function of the cumulative probability, as it represent the probability that the random variable Y assumes values higher than the argument value y;

$$R(y) = Prob(Y > y) = 1 - F(y) \tag{A.10}$$
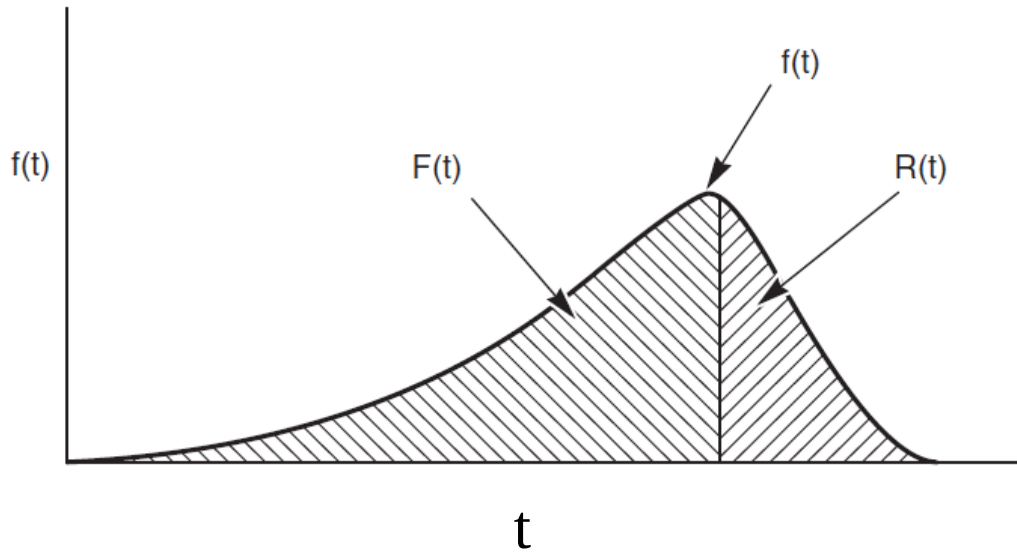
Figure A.1: In figure is reported a plot of the main probability functions, including PDF $f(t)$, CDF $F(t)$ and reliability $R(t)$. Adapted from [19]

A representation of probability density ($f(y)$), cumulative probability ($F(y)$) and reliability ($R(y)$) functions is reported in Fig. A.1.

Finally the failure rate $h(t)$ expresses the probability of the component to fail after reaching a time t. In particular, the failure probability of the component in the interval $(t, t + dt]$ is given by the product between the probability of the component to exceed the threshold t, and the probability of the component to fail after exceeding t. Thus:

$$f(t)dt = R(t) \cdot h(t)dt \tag{A.11}$$

from which results that:

$$h(t) = \frac{f(t)}{R(t)} \tag{A.12}$$

As the complexity of a component gets higher, the failure rate increases considerably. Considering eqs. (A.4) and (A.10), this can also be rewritten as:

$$h(t) = -\frac{1}{R(t)}\frac{dR(t)}{dt} = -\frac{d}{dt}(\ln R(t)) \tag{A.13}$$

The integral of the hazard rate is the cumulative hazard or failure rate:

$$H(t) = \int_0^t h(t')dt = -\ln R(t) \tag{A.14}$$

The dimension of $h(t)$ is (time^{-1}). Since $R(0) = 1$, the reliability rate over a time period t is the exponential of the cumulative hazard rate in the same period t:

$$R(t) = \exp\left(-\int_0^t h(t')dt\right) \tag{A.15}$$
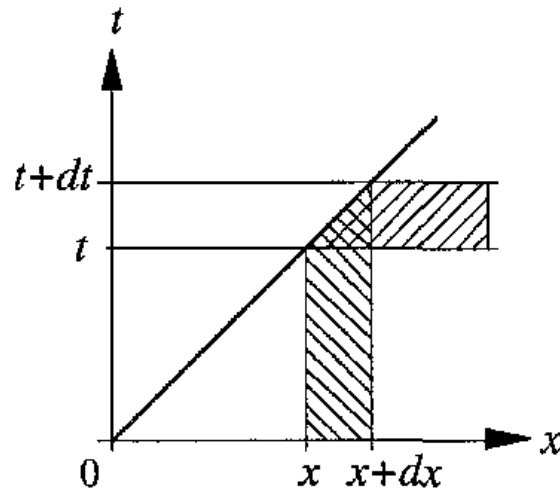
Figure A.2: In figure is reported a graph with the relation x-t, used to demonstrate the equivalence between eq. (A.18) and eq. (A.19). Adapted from [19]

In many practical applications, the failure rate can be assumed to be nearly constant for all $t \geq 0$ ($h(t) = h$). Thus, from eq. (A.13) follows:

$$R(t) = \exp\left(-ht\right) \tag{A.16}$$

An important quantitative reliability concept is how long the population will survive without a failure. This is also termed *mean time to failure* (MTTF), more specifically, the mean time to the first failure. The mean of a continuous random variable (t) with density $f(t)$ (PDF), provided the integral converges absolutely, is given by:

$$\bar{t} \equiv \int_{-\infty}^{\infty} t f(t) dt \tag{A.17}$$

For positive continuous random variables, eq. (A.17) reduces to:

$$\bar{t} \equiv \int_{0}^{\infty} t f(t) dt \tag{A.18}$$

For $\bar{t} \leq \infty$, eq. (A.18) can be expressed as:

$$\bar{t} \equiv \int_{0}^{\infty} (1 - F(t)) dt = \int_{0}^{\infty} R(t) dt \tag{A.19}$$

Let's demonstrate that eq. (A.18) and eq. (A.19) are equivalent[19].
From:

$$R(t) = 1 - F(t) = \int_{t}^{\infty} f(x) dx \tag{A.20}$$

follows that:

$$\int_{0}^{\infty} R(t) dt = \int_{0}^{\infty} \int_{t}^{\infty} f(x) dx dt \tag{A.21}$$

126

Changing the order of integration yields (see Fig. A.2):

$$\int_0^\infty R(t)dt = \int_0^\infty \left(\int_0^x dt \right) f(x)dx = \int_0^\infty x f(x)dx \qquad \text{(A.22)}$$

In many practical applications, the failure rate can be assumed to be nearly constant for all $t \geq 0$ ($h(t) = h$). In this cases it is common to define the *mean time between failures* (MTBF), which, putting eq. (A.16) inside eq. (A.19) becomes:

$$MTBF = \frac{1}{h} \qquad \text{(A.23)}$$

A.1.2 Trend Indicators and Dispersion Measures

Assuming to treat a random variable Y and to have its own distribution, it's possible to define as trend indicators those values that define the central tendency of the distribution. In particular they are:

- expected value of a discrete variable:

$$E(Y) = \mu = \sum_{y \in \Upsilon} y \cdot p(y) \qquad \text{(A.24)}$$

- expected value of a continuous variable:

$$E(Y) = \mu = \int_\Upsilon y \cdot f(y)dy \qquad \text{(A.25)}$$

- mode is the argument value that maximize the probability mass function $p(y)$ (if Y is discrete), or the probability density function $f(y)$ (if Y is continuous);

- median is the argument value corresponding to the percentile $p \cdot 50\%$ of Y.

Dispersion measures, on the other hand, define the dispersion of data around the average value of the distribution. In particular, they are:

- variance of a discrete random variable:

$$Var(Y) = \sigma^2 = \sum_{y \in \Upsilon} (y - \mu)^2 p(y) \qquad \text{(A.26)}$$

- variance of a continuous random variable:

$$Var(Y) = \sigma^2 = \int_\Upsilon (y - \mu)^2 f(y)dy = E(Y^2) - \mu^2 \qquad \text{(A.27)}$$

- standard deviation:

$$std(Y) = \sigma = \sqrt{Var(Y)} \qquad \text{(A.28)}$$

- variation coefficient:

$$CV = \frac{\sigma}{|\mu|} \tag{A.29}$$

Obviously, in practice it is not possible to carry out an infinite series of experiments. Thus, supposing that the number of experiments is finite (n), a succession of independent and identically distributed random variables will be obtained ($Y1, \ldots, Yn$), each of which represents the result of the i-th repetition of the experiment . The sequence $Y1, \ldots, Yn$ is called simple random sample, extracted from the population Y. Statistics can be defined by which it is possible to obtain information on the centrality and dispersion indicators of the variable Y. These estimators are:

- sample mean:

$$\hat{Y} = \frac{\sum_i Y_i}{n} \tag{A.30}$$

whose realization $\hat{y}$ is an estimate of the average $E(Y)$;

- sample variance and standard deviation:

$$S^2 = \sum_i \frac{(Y_i - \hat{Y})^2}{(n-1)} \tag{A.31}$$

$$S = \sqrt{S^2} \tag{A.32}$$

whose respective realizations s^2 and s are estimates of the variance σ^2 and standard deviation σ of the population.

A.2 Failure Distributions

Different probability distributions can be used to describe a failure statistic, and each has its advantages and is better than another depending on the phenomenon to be described. For this thesis work, the variable y is always referred to a time, so it will be rewritten as t in the following sections.

A.2.1 Normal Distribution

The most used statistical model for the distribution of a random variable is the normal distribution. This one is important above all because, thanks to the central limit theorem, it is proved that if any random variable is sampled, increasing the number of replication samples, the variable corresponding to the average value tends to assume a normal distribution.
A random variable Y follow this statistic if, for $-\infty \leq t \leq \infty$, its probability density function is:

$$f(t) = \frac{1}{\sigma\sqrt{2\pi}} \exp\left[-\frac{1}{2}\left(\frac{t-\mu}{\sigma}\right)^2\right] \tag{A.33}$$
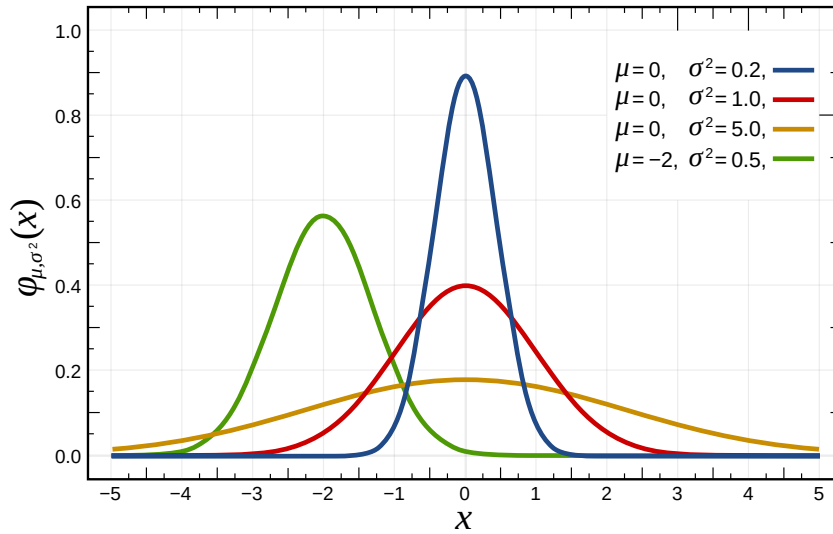
Figure A.3: In figure is reported a graph showing the main characteristics of a normal distribution. It is noticeable that μ influences the position of the curve, while σ the width of the peak. Adapted from [63]

The normal distribution is symmetrical with respect to the mean value μ (also equal to mode and median) with two inflection points in $y = \mu \pm \sigma$. From eq. (A.33) it can be deduced that μ controls the position of the distribution along the axis of argumentative values, while σ controls the width of the bell (see Fig. A.3).

The cumulative probability function is defined instead as:

$$F(t) = \int_{-\infty}^{y} f(t)dy = \int_{-\infty}^{y} \frac{1}{\sigma\sqrt{2\pi}} \exp\left[-\frac{1}{2}\left(\frac{t-\mu}{\sigma}\right)^2\right] dt \qquad (A.34)$$

It is useful to define the standard variable Z:

$$Z = \frac{T-\mu}{\sigma} \qquad (A.35)$$

In this way the probability density function of Z is normal with $\mu = 0$ and $\sigma = 1$:

$$\phi(z) = \frac{1}{\sigma\sqrt{2\pi}} \exp\left[-\frac{z^2}{2}\right] \qquad (A.36)$$

from which the cumulative probability function becomes:

$$\Phi(z) = \int_{-\infty}^{z} \frac{1}{\sigma\sqrt{2\pi}} \exp\left[-\frac{z^2}{2}\right] dz \qquad (A.37)$$

Through a simple variables substitution, from eqs. (A.33) and (A.36) follows:

$$\int_{t_1}^{t_2} f(y)dy = \int_{z_1}^{z_2} \phi(z)dz \qquad (A.38)$$

from which, through eq. (A.35) derives:

$$F(t) = \Phi\left(\frac{t-\mu}{\sigma}\right) = \Phi(z) \qquad (A.39)$$

Then, thanks to symmetry distribution results that:

$$\Phi(-z) = 1 - \Phi(z) \tag{A.40}$$

Finally, considering eq. (A.39) and inverting the variables, follows that:

$$t_p = \mu + z_p \cdot \sigma \tag{A.41}$$

where z_p is the percentile of the standard normal distribution. Characteristic values of z_p are tabulated and can be easily found in literature.

A.2.2 Log-Normal Distribution

When the variable $x = \ln(t)$ is normally distributed, then the variable t follows a log-normal distribution, and so from:

$$f(x) = \frac{1}{\sigma\sqrt{2\pi}} \exp\left[-\frac{1}{2}\left(\frac{x-\mu}{\sigma}\right)^2\right] \tag{A.42}$$

substituting $x = \ln(t)$, results:

$$f(t) = \frac{1}{t\sigma\sqrt{2\pi}} \exp\left[-\frac{1}{2}\left(\frac{\ln(t) - \ln(T_{50\%})}{\sigma}\right)^2\right] \tag{A.43}$$

where $T_{50\%}$ is the median lifetime ($F(T_{50\%}) = 50\%$) and $T_{50\%} = \exp(\mu)$.

In the case of log-normal distribution, $f(t)$ cannot be integrated, and hence an explicit equation is not available for $F(t)$, $R(t)$ and $h(t)$. The values of $F(t)$ can be obtained through numerical methods using the standard normal distribution, with variable transformation:

$$z = \frac{x-\mu}{\sigma} = \frac{\ln(t/T_{50\%})}{\sigma} \tag{A.44}$$

Results of the following integral are tabulated for many values of z:

$$\Phi(z) = \frac{1}{\sqrt{2\pi}} \int_{-\infty}^{z} \exp\left(-\frac{z'^2}{2}\right) dz' \tag{A.45}$$

so $F(t)$ can be easily obtained as:

$$F(t) = \Phi(z) = \Phi\left(\frac{\ln(t/T_{50\%})}{\sigma_T}\right) \tag{A.46}$$

Depending on σ (see Fig. A.4), log-normal distribution is able to model failure distributions related to physical and chemical degradation mechanisms as fatigue life, corrosion, electromigration and so on.
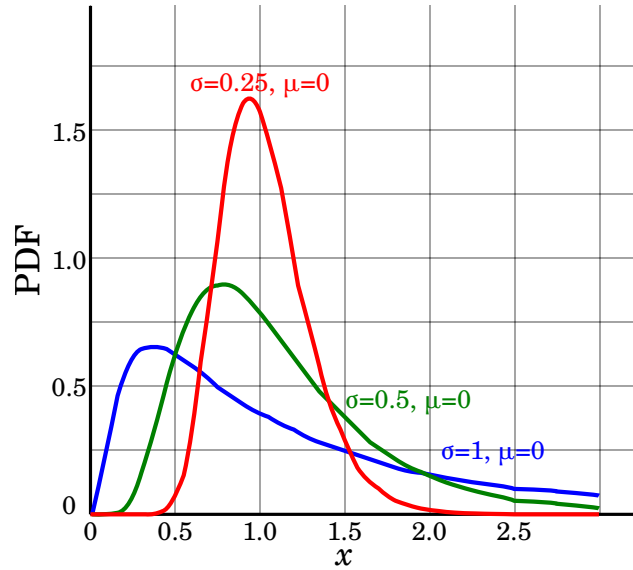
Figure A.4: In figure is reported a graph showing the main characteristics of a log-normal distribution. It is noticeable that σ influences a lot the shape of the curve. Adapted from [64]

A.2.3   Negative Exponential Distribution

Negative exponential distribution is used in reliability analyses for a considerable number of industrial devices and machinery, as it is suitable to model the useful life phase on the bathtub curve. Indeed, for this distribution failure rate is taken as constant ($h(t) = \lambda$), and so reliability function becomes:

$$R(t) = \exp(-\lambda t) \tag{A.47}$$

Consequently, cumulative probability function is:

$$F(t) = 1 - \exp(-\lambda t) \tag{A.48}$$

A random variable T follows a negative exponential distribution with parameter $\lambda > 0$ if its probability density function is the following (see Fig. A.5):

$$f(t) = \lambda \exp(-\lambda t) \tag{A.49}$$

The property of $h(t)$ being constant is called *"lack of memory"* and, theoretically, it is not applicable to components subjected to degradation phenomena, as progressive damaging affects failure rate, which tends to grow. Nevertheless, exponential distribution is taken as the basis to describe reliability of systems in time.

A peculiarity of this failure distribution is that, being $h(t) = \lambda$ constant, the mean time to failure of a random variable T described by it, is simply its expected value:

$$MTTF = E(T) = \frac{1}{\lambda} \tag{A.50}$$

Then, in correspondence of $t = 1/\lambda$, the cumulative probability function is:

$$F(MTTF) = F(1/\lambda) = 0.632 \tag{A.51}$$

This means that the mean value of the distribution corresponds to the percentile 63.2%.
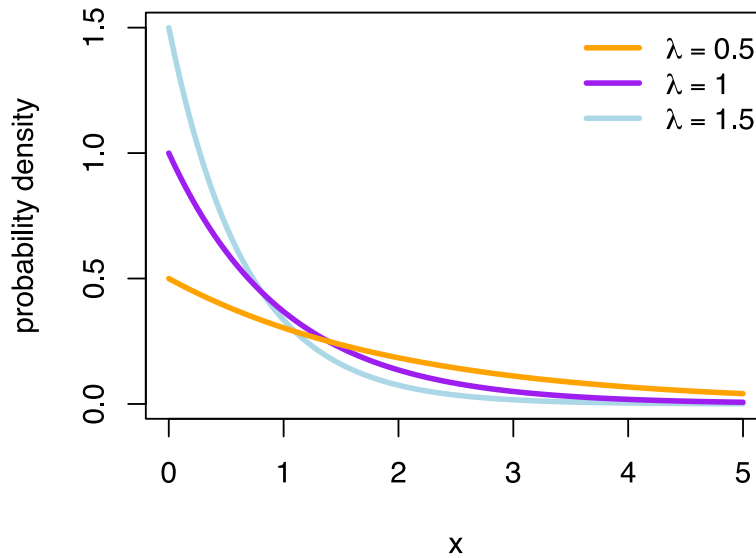
Figure A.5: In figure is reported a graph showing the main characteristics of a negative exponential distribution. It is noticeable how λ influences the behavior of the function. Adapted from [65]

A.2.4   Weibull Distribution

The Weibull distribution is widely used in engineering for the flexibility that its parameters offer in the construction of different models. In particular, a random variable T is distributed as a Weibull with parameters $\alpha > 0$ and $\beta > 0$ if its probability density function is:

$$f(t) = \frac{\beta}{\alpha^\beta} t^{\beta-1} \exp\left[-\left(\frac{t}{\alpha}\right)^\beta\right] \tag{A.52}$$

with $t \geq 0$, α = scale parameter and β = shape parameter.

The cumulative probability function is:

$$F(t) = 1 - \exp\left[-\left(\frac{t}{\alpha}\right)^\beta\right] \tag{A.53}$$

The percentile of the Weibull is:
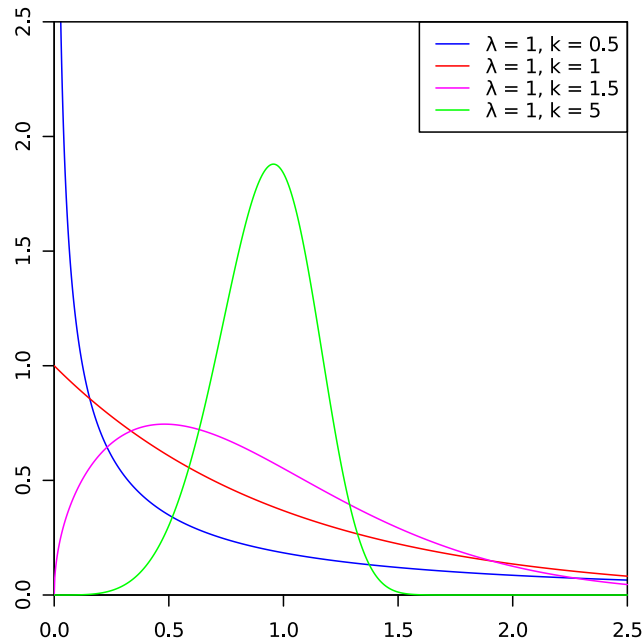
$$t_p = \alpha[-\ln(1-p)]^{\frac{1}{\beta}} \tag{A.54}$$

while reliability is:

$$R(t) = \exp\left[-\left(\frac{t}{\alpha}\right)^\beta\right] \tag{A.55}$$

From eq. (A.53) it is noticeable that $F(\alpha) = 63.2\%$. Weibull distribution significantly changes its shape with different values of β (see Fig. A.6):

- for $\beta = 1$ it is a negative exponential distribution;

132

Figure A.6: In figure is reported a graph showing the main characteristics of a Weibull distribution. In this plot λ stands for the scale factor α, while k for the shape factor β. It is noticeable that k influences a lot the shape of the curve. Adapted from [66]

- for $\beta = 2$ it is similar to a log-normal distribution;

- for $3.5 < \beta < 4$ it is similar to a normal distribution.

Furthermore, for $\beta < 1$ $h(t)$ is decreasing, for $\beta = 1$ $h(t)$ is constant and for $\beta > 1$ $h(t)$ is increasing. For this reason Weibull distribution is used a lot to describe components life, as it is able to model all the three phases of a bathtub curve. It is used for several types of failure modes, in particular in semiconductor field to analyze mechanical fatigue failures and oxide breakdown.

Bibliography

[1]   Alberto Corigliano, Raffaele Ardito, Claudia Comi, Attilio Frangi, Aldo Ghisi, and Stefano Mariani. *Mechanics of Microsystems.* 1st ed. Wiley & Sons, 2018. ISBN: 9781119053804 (cited on p. 1).

[2]   Attilio Frangi, Andrea Guerrieri, Nicolo Boni, Roberto Carminati, Marco Soldo, and Gianluca Mendicino. "Mode Coupling and Parametric Resonance in Electrostatically Actuated Micromirrors". In: *IEEE* 65 (2018), pp. 5962–5969 (cited on pp. 5, 10).

[3]   K.R. Oldham. *MEMS for Biomedical Applications.* Elsevier. Chap. 10 (cited on pp. 6, 7).

[4]   S. Gu-Stoppel, D. Kaden J. Janes, H. J. Quenzer, U. Hofmann, and W. Benecke. "Piezoelectric resonant micromirror with high frequency and large deflection applying mechanical leverage amplification". In: *Proc. SPIE* 8612 (2013) (cited on pp. 8, 21, 22).

[5]   Hakan Urey, David Wine, and Thor Osborn. "Optical performance requirements for MEMS-scanner based microdisplays". In: *Proc. SPIE* 4178 (2000), pp. 176–185 (cited on pp. 10, 14, 15, 16, 18).

[6]   Jeffrey F. Rhoads, Congzhong Guo, and Gary K. Fedder. *Resonant MEMS–Fundamentals, Implementation and Application.* 1st ed. Wiley-VCH Verlag GmbH & Co. KGaA, 2015. Chap. 4. ISBN: 9783527335459 (cited on p. 10).

[7]   Eugene I. Butikov. "Parametric Resonance". In: *Computing in Science and Engineering* 1 (1999), pp. 76–83 (cited on p. 10).

[8]   *Silicon Single Crystal.* 2019. URL: https://www.americanelements.com/silicon-single-crystal-7440-21-3 (visited on 06/24/2019) (cited on p. 11).

[9]   K.E. Petersen. "Silicon as a mechanical material". In: *IEEE* 70 (1982), pp. 420–457 (cited on p. 11).

[10]   *Gaussian Beams.* 2019. URL: https://www.rp-photonics.com/gaussian_beams.html (visited on 06/17/2019) (cited on p. 13).

[11]   *Modulation Transfer Function.* 2019. URL: https://www.edmundoptics.com/resources/application-notes/optics/introduction-to-modulation-transfer-function/ (visited on 06/17/2019) (cited on p. 13).

[12]   David W. Wine, Mark P. Helsel, Lorne Jenkins, Hakan Urey, and Thor D. Osborn. "Performance of a Biaxial MEMS-Based Scanner for Microdisplay Applications". In: *Proc. SPIE* 4178 (2000), pp. 186–196 (cited on p. 14).

[13]   *Damping Ratio.* 2019. URL: https://en.wikipedia.org/wiki/Damping_ratio (visited on 06/27/2019) (cited on p. 17).

[14]   Patterson P.R., Hah D.and Fujino M., Piyawattanametha W., and Wu M.C. "Scanning micromirrors: An overview". In: *Proceedings of SPIE* 5604 (2004), pp. 195–207 (cited on pp. 19, 20).

[15]   Li Fan and Ming C. Wu. "Two-Dimensional Optical Scanner with Large Angular Rotation Realized by Self-Assembled Micro-Elevator". In: *Proc. IEEE LEOS Summer Topical Meeting on Optical MEMS* (1998) (cited on p. 19).

[16]   Attilio Frangi, Andrea Guerrieri, Roberto Carminati, and Gianluca Mendicino. "Parametric Resonance in Electrostatically Actuated Micromirrors". In: *IEEE* 64 (2017), pp. 1544–1551 (cited on p. 20).

[17]   Hee-Moon Jeong et al. "Slow Scanning Electromagnetic MEMS Scanner for Laser Display". In: *SPIE* 6887 (2008) (cited on p. 21).

[18]   *What is innovation?* 2019. URL: https://www.ideatovalue.com/inno/nickskillicorn/2016/03/innovation-15-experts-share-innovation-definition/ (visited on 08/23/2019) (cited on p. 41).

[19]   Alessandro Birolini. *Quality and Reliability of Technical Systems.* 2nd ed. Springer, 1997. ISBN: 3540633103 (cited on pp. 42, 44, 69, 123, 125, 126).

[20]   Allyson L. Hartzell, Mark G. da Silva, and Herbert R. Shea. *MEMS Reliability.* 1st ed. Springer, 2011. ISBN: 9781441960177 (cited on pp. 44, 123).

[21]   Stefano Beretta. *Affidabilita' delle costruzioni meccaniche.* 1st ed. Springer, 2018. ISBN: 9788847010789 (cited on pp. 44, 89, 92, 123).

[22]   *JEDEC.* 2019. URL: https://www.jedec.org/ (visited on 08/04/2019) (cited on pp. 47, 48, 49).

[23]   *Six-sigma.* 2019. URL: http://www.skillpower.co.nz/wp-content/uploads/2015/12/mmmmmmmmmm.png (visited on 06/10/2019) (cited on p. 52).

[24]   *Vibration and Shock Testing.* Standard. U.S. Department of Defence, Dec. 1996 (cited on pp. 58, 60, 71).

[25]   *Vibration and Shock Testing.* Standard. U.S. Department of Defence, July 1989 (cited on pp. 59, 60).

[26]   *Elman.* 2019. URL: http://www.elman-systems.com/english/profilo.asp (visited on 07/23/2019) (cited on p. 60).

[27]   J. Moulin, M. Woytasik, J.-P. Grandchamp, E. Dufour-Gergam, and A. Bosseboeuf. "High current densities in copper microcoils: influence of substrate on failure mode". In: *Microsystem Technologies* 13 () (cited on p. 62).

[28]   Shoji Kamiya. "Shear stress with hydrogen, not oxygen, matters to the fatigue lifetime of silicon". In: *Transducers - Int. Conf. Solid-State Sensors - Actuators Microsyst - TRANSDUCERS* (Aug. 2015) (cited on pp. 67, 105).

[29]   Shoji Kamiya. "Shear stress enhanced fatigue damage accumulation in single crystalline silicon under cyclic mechanical loading". In: *Sens Actuators A Phys* 244 (June 2016) (cited on pp. 67, 105).

[30] J.A. Connaly and S.B. Brown. "Slow Crack Growth in Single-Crystal Silicon". In: *Science* 256 (June 1992) (cited on pp. 67, 105).

[31] J.A. Connaly. "Micromechanical fatigue testing". In: *Experimental Mechanics* 33 (June 1993) (cited on pp. 67, 105).

[32] P. Shrotriya, S. Allameh, S. Brown, Z. Suo, and W.O. Soboyejo. "Fatigue damage evolution in silicon films for micromechanical applications". In: *Experimental Mechanics* 43 (Sept. 2003) (cited on pp. 67, 105).

[33] Van Spengen and W. Merlijin. "MEMS reliability from a failure mechanisms perspective". In: *Microelectronics Reliability* 43 (July 2003) (cited on pp. 67, 105).

[34] O.N. Pierron. "Fatigue rates of monocrystalline silicon thin films in harsh environments: Influence of stress amplitude, relative humidity, and temperature". In: *Applied Physics Letters* 94 (2009) (cited on pp. 67, 105).

[35] O.N. Pierron. "Highly localized surface oxide thickening on polycrystalline silicon thin films during cyclic loading in humid environments". In: *Acta Materialia* 57 (2009) (cited on pp. 67, 105, 107).

[36] Terry A. Michalske and Stephen W. Freiman. "A Molecular Interpretation of Stress Corrosion in Silica". In: *Nature* 295 (Feb. 1982), pp. 511–512 (cited on pp. 67, 105, 107).

[37] S. M. Wiederhorn. "A Chemical Interpretation of Static Fatigue". In: *Journal of the American Ceramic Society* 55 (Feb. 1972), pp. 81–85 (cited on pp. 67, 105, 107).

[38] S. M. Wiederhorn and L. H. Bolz. "Stress Corrosion and Static Fatigue of Glass". In: *Journal of the American Ceramic Society* 53 (Oct. 1970), pp. 543–548 (cited on pp. 67, 105, 107).

[39] *Low Temperature Storage Life*. Standard. JEDEC, Nov. 2004 (cited on p. 69).

[40] *Accelerated Moisture Resistance - Unbiased HAST*. Standard. JEDEC, July 2015 (cited on p. 69).

[41] *Temperature Cycling*. Standard. JEDEC, July 2000 (cited on p. 70).

[42] *Electrostatic Discharge (ESD) Sensitivity Testing Human Body Model (HBM)*. Standard. JEDEC, Dec. 2007 (cited on p. 71).

[43] Lee Shao-Kuan, Hsu Hsiu-Ching, and Tuan Wei-Hsing. "Oxidation behavior of copper at a temperature below 300 ℃ and the methodology for passivation". In: *Materials Research* 19 (2016), pp. 51–56 (cited on p. 80).

[44] Matts Björck and Ragna Elger. "Oxidation kinetics of copper at reduced oxygen partial pressures". In: (2013) (cited on p. 80).

[45] Zhu Yongfu, Mimura Kouji, Lim Jae-Won, Isshiki Minoru, and Qing Jiang. "Brief review of oxidation kinetics of copper at 350 ℃ to 1050 ℃". In: *Metall Mat Trans A Phys Metall Mat Sci* 37 (2006), pp. 1231–1237 (cited on p. 80).

[46] Hadi Ebrahimifar and Morteza Zandrahimi. "Study of parabolic rate constant for coated AISI 430 steel with Mn3O4 and MnFe2O4 spinels". In: *Indian Journal of Engineering and Materials Sciences* 18 (2011), pp. 314–320 (cited on p. 80).

[47] William Landford and Peijun Ding. "Oxidation resistant high conductivity copper layers for microelectronic applications and process of making same". In: *United States Patent* (1999) (cited on p. 80).

[48] *Deal-Grove oxidation model.* 2019. URL: http://www.iue.tuwien.ac.at/phd/hollauer/node16.html (visited on 08/28/2019) (cited on p. 80).

[49] D. H. Alsem. "Mechanisms for fatigue of micron-scale silicon structural films". In: *Advanced Engineering Materials* 9 () (cited on pp. 105, 106).

[50] G. Langfelder. "A polysilicon test structure for fatigue and fracture testing in micro electro mechanical devices". In: *Proceedings of IEEE Sensors* (2008), pp. 94–97 (cited on p. 105).

[51] G. Langfelder. "Real-time monitoring of the fatigue damage accumulation in polysilicon microstructures at different applied stresses". In: *Proceedings of IEEE Sensors* (2009), pp. 888–893 (cited on p. 105).

[52] G. Langfelder. "A new on-chip test structure for real time fatigue analysis in polysilicon MEMS". In: *Microelectronics Reliability* 49 (2009), pp. 120–126 (cited on p. 105).

[53] A. Ghisi. "A microsystem for the fracture characterization of polysilicon at the micro-scale". In: *Eur J Mech A Solids* 30 (2011), pp. 127–136 (cited on p. 105).

[54] C.L. Muhlstein. "High-cycle fatigue of single-crystal silicon thin films". In: *Journal of Microelectromechanical Systems* 10 (Dec. 2001) (cited on pp. 67, 105, 106, 120).

[55] C.L. Muhlstein, E.A. Stach, and R.O. Ritchie. "Mechanism of fatigue in micron-scale films of polycrystalline silicon for microelectromechanical systems". In: *Applied Physics Letters* 80 (Mar. 2002), pp. 1532–1534 (cited on pp. 67, 105, 106, 109, 120).

[56] C.L. Muhlstein, E.A. Stach, and R.O. Ritchie. "A reaction-layer mechanism for the delayed failure of micron-scale polycrystalline silicon structural films subjected to high-cycle fatigue loading". In: *Acta Materialia* (Aug. 2002) (cited on pp. 67, 105, 106, 120).

[57] H. Kahn, R. Ballarini, A.H. Heuer, and J. Ballante. "Fatigue failure in polysilicon not due to simple stress corrosion cracking". In: *Science* 298 (Nov. 2002) (cited on pp. 67, 105, 106).

[58] H. Kahn, R. Ballarini, and A.H. Heuer. "Dynamic fatigue of silicon". In: *Curr. Opin. Solid State Mater. Sci.* 8 (Jan. 2004) (cited on pp. 67, 105, 106).

[59] M. Ciccotti. "Stress-Corrosion Mechanisms in Silicate Glasses". In: *J. Phys. D: Appl. Phys.* (2009) (cited on pp. 107, 108, 109).

[60] B. Kobrin, J. Chinn, and R. W. Ashurst. "Durable Anti-Stiction Coatings by Molecular Vapor Deposition (MVD)". In: *Nanotechnol. Conf. Trade Show Nanotech Techn. Proc.* (2005), pp. 347–350 (cited on p. 116).

[61] Y. X. Zhuang. "Vapor-phase self-assembled monolayers for anti-stiction applications in MEMS". In: *J Microelectromech Syst* 16 (2007), pp. 1451–1460 (cited on pp. 116, 117).

[62] W. R. Ashurst. "Vapor-Phase Deposited Chlorosilane-Based Self-Assembled Monolayers on Various Substrates for Thermal Stability Analysis". In: *Ind. Eng. Chem. Res.* 56 (2017), pp. 5239–5252 (cited on p. 116).

[63] *Normal distribution.* 2019. URL: https://en.wikipedia.org/wiki/Normal_distribution (visited on 07/21/2019) (cited on p. 129).

[64] *Lognormal distribution.* 2019. URL: https://en.wikipedia.org/wiki/Lognormal_distribution (visited on 07/21/2019) (cited on p. 131).

[65] *Exponential distribution.* 2019. URL: https://en.wikipedia.org/wiki/Exponential_distribution (visited on 07/21/2019) (cited on p. 132).

[66] *Weibull distribution.* 2019. URL: https://en.wikipedia.org/wiki/Weibull_distribution (visited on 07/21/2019) (cited on p. 133).